
Copyright Undertaking

EFFECTS OF POROUS WALLS ON SUPERSONIC/HYPERSONIC BOUNDARY-LAYER INSTABILITY

TIAN XUDONG

PhD

The Hong Kong Polytechnic University

2020

The Hong Kong Polytechnic University

Department of Mechanical Engineering

EFFECTS OF POROUS WALLS ON SUPERSONIC/HYPERSONIC BOUNDARY-LAYER INSTABILITY

TIAN XUDONG

A thesis submitted in partial fulfillment of the
requirements for the degree of Doctor of Philosophy

February 2020

CERTIFICATE OF ORIGINALITY

I hereby declare that this thesis is my own work and that, to the best of my knowledge and belief, it reproduces no material previously published or written, nor material that has been accepted for the award of any other degree or diploma, except where due acknowledgment has been made in the text.

_____________________________(Signed)

_________TIAN Xudong_______(Name of student)

Abstract

The effects of porous walls on supersonic/hypersonic boundary-layer instability are investigated using theoretical and numerical approaches. The linear stability theory (LST) is utilized to examine the effects of admittance magnitude and phase on the first and second modes. Numerical simulations are performed to validate the theoretical predictions. Phase analysis is employed to study the mechanisms of the growth of the first and second modes. A design strategy of the ultrasonic absorptive coating (UAC) is also proposed to stabilize the first and second modes.

The analyses based on the adiabatic or quasi-adiabatic wall show the stabilization and destabilization of the first and second modes depend on the wall admittance phase and are facilitated by the increase in the wall admittance magnitude. Moreover, the effects of porous walls on the first and second modes are independent of the wave-propagation angle.

Both for the first and second modes, the fluctuating internal energy is dominated by the advection of perturbed thermal energy by mean flow in the vicinity of the critical layer and by the dilatation fluctuation near the wall. The growth rate of the second mode is determined by the contribution of the heat transport by the wall-normal velocity fluctuation to the fluctuation in the vicinity of the critical layer. While the growth rate of the first mode is associated with the energy exchange between the dilatation fluctuation and the internal energy fluctuation near the wall. Porous walls alter the phase of the wall-normal fluctuating velocity, which recasts the phase of the energy transport by the wall-normal velocity fluctuation.

The design strategy of UAC focusing on the admittance magnitude and phase can provide quantitative requirements on the stabilization of the first and second modes. The designed UAC remarkably damps the second mode and meanwhile avoids aggravating the first mode in a supersonic flat-plate boundary layer.

Acknowledgments

It is with the author's most profound gratitude and highest respect that he would like to express to his chief supervisor, Prof. WEN Chihyung, for his guidance and support throughout the author's graduate studies. His rigorous attitude and strict requirements for academic research lead the author on the right track of research. His attitude of being a friend to his students makes him the best advisor any graduate student can have.

The author is sincerely grateful to Prof. ZHAO Rui for his warm-hearted assistance and invaluable suggestions. The author would also like to thank his collaborators, LONG Tiehan and Dr. HAO Jiaao, for many enlightening discussions. The author is also obliged to Prof. LI Xinliang for providing CFD code.

The author would like to express a special acknowledgment to all the members of Prof. WEN's research team, who create a perfect environment for intellectual development and personal life.

Finally, the author thanks his family and his girlfriend, CHEN Jing, for their hearty encouragement and constant support.

Table of Contents

List of Figures

List of Tables

Chapter 1 Introduction

Boundary layer transition in the supersonic and hypersonic regimes is critical for the design of high-speed flight vehicles. In contrast to the laminar flow, heat transfer and skin friction drag are remarkably higher in the turbulent flow [1-3]. Therefore, it can decrease the weight of thermal protect systems (TPSs) and the payload penalty by maintaining laminar flow over vehicle surfaces. These benefits motivate the studies on the prediction and control of the laminar-turbulent transition in supersonic and hypersonic boundary layers.

The paths of laminar-turbulent transition are closely associated with the forcing environmental disturbances [4]. In low disturbance environments, instability waves experience a linear growth governed by eigenmodes at the early stage of development. If the initial disturbances are high enough, the eigenmode growth will be bypassed and breakdown emerges straightforwardly [5]. In flight environments, free-stream disturbances are regularly small [6], therefore, only small perturbations are concerned in this study.

For the supersonic and hypersonic boundary layer on a flat plate or an axisymmetric body at zero angle attack, the linear growth stage is dominated by the first or second mode [7-9]. Generally, the first mode is dominant at the low Mach number, and the ruling by the second mode commences when the Mach number increases [9]. For an insulated wall, the second mode becomes dominant when $Ma > 4$, and this number is smaller for a cooled wall [10].

The first mode in the supersonic and hypersonic boundary layer is deemed as an extension of the Tollmien-Schlichting (T-S) mode, and the most unstable first-mode waves are three-dimensional (3D) waves [7]. The second mode is also called as “Mack mode” since Mack firstly found this higher mode using compressible linear stability theory (LST) [3]. The second mode waves belong to acoustic waves and propagate between the wall and the relative sonic line with a phase speed close to the velocity at the boundary layer edge [9, 11, 12]. The wavelength of the second mode approximates twice the boundary layer thickness, and the frequencies are commonly over 100kHz [13-15].

Practically, the prediction of the boundary layer transition is arduous due to the uncertainty of the environmental fluctuations [16]. Fortunately, the control of the boundary layer transition is not restricted by the transition locus. In current work, we focus on the transition control by stabilizing the first and second modes and also endeavor to understand the mechanisms of the first- and second-mode instabilities.

1.1 A Review of Previous Work and Motivation

Since theoretical works conducted by Mack [3, 7] and experimental studies[13-15, 17-19] show that the second mode dominates the hypersonic boundary layer instabilities, the control of hypersonic boundary-layer transition mainly focuses on stabilizing the second mode using active or passive techniques, such as suction, pressure gradient, wavy wall, localized heating or cooling, ultrasonic absorptive coating (UAC), etc. [16, 20-22]. The second-mode disturbances can be induced by external perturbations, therefore, the commonly used wall polishing which can diminish the internal disturbances cannot eliminate the second-mode disturbances.

Malik [20] theoretically investigated the effect of wall suction and pressure gradient on the second-mode instabilities, and the results show that both wall suction and pressure gradient can decrease the maximum growth rate of the second mode. However, wall suction as an active control technique is challenging to implement in hypersonic flights because of the severe flow conditions [23]. The pressure gradient which can be achieved by wall shaping (convex surface) may generate crossflow instabilities or Görtler vortices.

Wall cooling can stabilize the first mode but destabilize the second mode [10]. Therefore, the delay of the mixed-mode transition using wall cooling depends on the dominant mode. Malik's calculations [20] based on a boundary layer flow over a 5^{o} half-angle sharp cone with boundary layer edge temperature of $111K$ show that the predicted transition Reynolds number (based on $N = 10$) increases from $Re_{tr} = 10 \times 10^6$ of an adiabatic wall to $Re_{tr} = 15 \times 10^6$ of a cold wall at $M_\infty = 5$, but decreases in cold wall cases in contrast to the adiabatic wall case at $M_\infty = 6$ and 7. This suggests the wall cooling may be valid for the moderate supersonic boundary layer in which the first mode is dominant.

Fedorov et al. [22] studied the effect of the localized wall heating or cooling on a 7^{o} half-angle sharp cone at zero angle of attack at Mach 6. The heating/cooling source is located near the leading edge. Both the experimental and numerical results indicate that the localized wall cooling can decrease disturbance magnitudes and delay transition while the heating has the opposite effect. Zhao et al. [21] numerically investigated the importance of the position of the localized wall heating/cooling on the instability propagation in a flat-plate boundary layer at Mach 6. In their simulations, small disturbances are generated by a zero-net mass-flux blowing-suction actuator with a fixed frequency of 138.74kHz. The results show the relative location between the local heating/cooling and synchronization point of slow and fast acoustic mode is significant for hypersonic boundary layer instabilities. The localized heating/cooling changes the local growth rate of unstable waves, which affects the downstream perturbation magnitude. It is recommended to mount the cooling Upstream or the heating downstream of the synchronization point to delay the hypersonic boundary layer transition.

Motivated by the stabilization caused by large Mach numbers in free shear layers and wakes [24, 25], Fedorov et al. [23] studied the effect of wavy walls, which generate small separation bubbles, on the second mode. The experiments carried out in the Institute of Theoretical and Applied Mechanics Tranzit-M shock tunnel at a free-stream Mach number of 6 show that the disturbances associated with the second mode are damped by a wavy wall while the disturbances in a low-frequency band are slightly amplified at relatively large Reynolds numbers of $Re_{1\infty} = 12.67 \times 10^6 \mathrm{m}^{-1}$ and $Re_{1\infty} = 15.41 \times 10^6 \mathrm{m}^{-1}$. Their numerical simulations also confirmed the decrease in the maximum amplitude of the second-mode fluctuations due to the wavy wall.

Since the frequency of the second mode is very high (on the order of 100kHz), Malmuth et al. [11] speculated that the stabilization of the second mode might be implemented by absorbing high-frequency disturbances via the porous surface of thermal protection systems (TPSs). They analyzed the inviscid instabilities of a hypersonic boundary layer at $M = 6$ and $T_w/T_{ad} \approx 0.2$ using the WKB method and found that a small reflective coefficient which corresponds to a strong absorption can significantly inhibit the second mode instability.

Fedorov et al. [26] utilized viscous stability theory to analyze the stabilization effect of the porous layer composed of uniformly distributed cylindrical blind micro-holes. The admittance of the porous layer was formulated using the theory of sound wave propagation in cylindrical conduits [27-29]. In their analyses, the stabilization effect of the porous layer is consistent with the results of Malmuth et al. [11], and the performance of the porous layer is closely associated with the porosity, porous layer thickness, and pore radius.

Rasheed et al. [30] conducted experiments on a 5.06^o half-angle slender cone covered by a porous wall on one half and a smooth wall on another half in the T5 Hypervelocity Shock Tunnel at $Ma_\infty \approx 5$. Experimental results demonstrate the porous wall successfully delays the boundary layer transition, which confirms the theoretical prediction [26]. Later, stabilization effects of porous walls composed of random microstructure (felt metal) and regular microstructure on the second mode instabilities were confirmed by the experiments carried out in the ITAM T-326 hypersonic blowdown wind tunnel [31, 32]. The ultrasonic absorptive carbon-carbon material with small average pore sizes and low porosities also shows the potential to delay the hypersonic boundary layer transition [33]. Nevertheless, it was found that the first mode is destabilized using felt metals [32].

Some numerical simulations were conducted as well to study the stabilization effects of porous walls on hypersonic boundary layer instabilities [34-38]. In the simulations performed by Sandham and Lüdeke [35], individual pores were meshed and resolved rather than modeled. The stabilization effect was found to be closely associated with the porosity and pore depth, while the pore shape did not play a significant role. Moreover, they found that the growth rate obtained from numerical simulations was smaller than the prediction from LST by 10~30%.

Brès et al. [34, 37] numerically investigated the stabilizing effect of porous coatings consisting of a uniform array of slots with different aspect ratios (width/depth) and porosities on hypersonic boundary layer instabilities at $Ma_{\infty} = 6$. The results show porous coatings with deep pores operate in an attenuative regime in which acoustic waves are attenuated due to fluid viscosity. Porous coatings with relatively shallow pores work in the cancellation or reinforcement regimes depending on the reflection of acoustic waves in the pores. Their linear simulations agree well with the prediction of LST, excluding one case dominated by resonant interactions. The mode linked to the acoustic resonance was found more unstable than the second mode and should be circumvented in the UAC design.

For the design of UAC, Brès et al. [39] emphasized two parameters: cavity depth and porosity. They derived a formula to determine the cavity depth, which corresponds to minimum reflection for the frequency of the most unstable second mode waves. According to their parametric study, high porosity is recommended. Essentially, their guidelines for the UAC design is to minimize the reflection coefficient for acoustic waves. However, these guidelines are deficient in the quantitative requirements on the reflection coefficient.

Stephen and Michael [40] investigated the effect of porous walls on the first mode of a hypersonic boundary layer. In their theoretical linear stability analyses, porous coatings, including regular microstructures and random microstructures employed in the experiments of Ref. [31, 32, 41], were found to destabilize the first mode. Wang and Zhong [42] found the destabilization of the first mode is associated with the admittance phase of porous coatings. Carpenter and Porter [43] found that the first mode can be stabilized in the incompressible boundary layer on a flat plate when the admittance phase approaches $\pi/2$.

Essentially, the reflection coefficient of porous walls for incident waves is a function of admittance magnitude and phase. Quantitative requirements for the design UAC may be resolved based on the admittance magnitude and phase. Moreover, the analyses based on the admittance magnitude and phase can give insight into the mechanisms of the impact of porous walls on the wall disturbance as the relation of the velocity and pressure fluctuations is provided by the admittance straightforwardly.

Unnikrishnan and Gaitonde [44, 45] utilized momentum potential theory to analyze the interactions of the fluid-thermodynamic components. They found that the source term generated by the thermal component is significant for the amplification of acoustic instabilities. Besides, the Rijke tube indicates that the phase of heat transfer is the key to excite acoustic waves. Therefore, it is motivated to perform phase analyses of the disturbance energy equation to study the mechanisms of the amplification of the first and second modes.

1.2 The Scope of Current Work

This thesis consists of six chapters, including this brief introduction. The methodology, including theoretical and numerical methods, is presented in Chapter 2. In Chapter 3, theoretical studies on the effects of porous walls on the first and second modes are described, and the mechanisms of the amplification of the first and second modes with and without porous walls are also discussed based on the phase analysis on the disturbance energy equation. In Chapter 4, the theoretical predictions are validated using direct numerical simulations (DNS), and the mechanisms of the amplification of the second mode with and without porous walls are investigated again based on DNS results which provide quantitative comparisons. Chapter 5 describes a strategy to design ultrasonic absorptive coating (UAC) to stabilize a supersonic boundary layer, in which the first and second mode coexist. Chapter 6 is the conclusion of current work.

Chapter 2 Methodology

This chapter describes the theoretical and numerical approaches utilized in this thesis. In the theoretical studies, linear stability theory is employed, and mean flow quantities are obtained using a self-similar solution. While in the numerical investigations, direct numerical simulations (DNS) are performed to validate the theoretical prediction and enhance the understanding of the mechanism of the effect of porous walls on hypersonic boundary-layer instability.

2.1 Linear Stability Theory

The instability problem in a compress viscous hypersonic or supersonic boundary layer can be resolved using the linear stability theory (LST) [7, 8, 46-49] or the parabolized stability equation (PSE) [50-57]. Fedorov [9], in his review paper, pointed out the shortcoming of the PSE method is that it could not get through the branch point of the fast and slow mode if the branch point falls in the real axis. In the current work, linear stability theory is chosen to analyze the hypersonic or supersonic boundary layer instabilities.

2.1.1 Governing Equations for Small Disturbances

The Navies-Stocks equations for a compressible viscous flow are

$$\frac{\partial \rho}{\partial t}+\frac{\partial}{\partial x_i}(\rho v_i)=0 \tag{2.1}$$

$$\rho\left(\frac{\partial v_i}{\partial t}+v_j\frac{\partial v_i}{\partial x_j}\right)=-\frac{\partial p}{\partial x_i}+\frac{\partial}{\partial x_i}\left(\lambda\frac{\partial v_k}{\partial x_k}\right)+\frac{\partial}{\partial x_j}\left[\mu\left(\frac{\partial v_i}{\partial x_j}+\frac{\partial v_j}{\partial x_i}\right)\right] \tag{2.2}$$

$$
\begin{aligned}
c_p\left(\frac{\partial T}{\partial t}+v_i\frac{\partial T}{\partial x_i}\right) &= \frac{\partial}{\partial x_i}\left(k\frac{\partial T}{\partial x_i}\right)+\frac{\partial p}{\partial t}+v_i\frac{\partial p}{\partial x_i} \\
&+\lambda\left(\frac{\partial v_i}{\partial x_i}\right)^2+\frac{\mu}{2}\left(\frac{\partial v_i}{\partial x_j}+\frac{\partial v_j}{\partial x_i}\right)^2
\end{aligned} \tag{2.3}
$$

where v_i is the velocity component in i direction, x_i the i axis, ρ the density, p the pressure, T the temperature, μ the first coefficient of viscosity, λ the second coefficient of viscosity, k the thermal conductivity, and c_p the specific heat. In this work, Stokes' hypothesis is adopted, i.e., $\lambda=-\frac{2}{3}\mu$. The index summation rule is also applied in the above equations.

The equation of state for ideal gases is given by

$$
p=\rho RT \tag{2.4}
$$

where R is the gas constant. In the following chapter, the Reynolds number is also denoted by R. Indeed, it is easy to distinguish between the gas constant and the Reynolds number.

This study focuses on the flat-plate boundary layer and hence Cartesian coordinates x, y, z are utilized, and the coordinate x and z represent the streamwise and spanwise directions, respectively, and y is normal to the wall. The velocities u, v, w are the components in x, y, z directions, respectively. The transient quantities are decomposed into mean-flow quantities and small fluctuations, as shown below:

$$
\begin{aligned}
u&=\bar{U}+u', & v&=\bar{V}+v', & w&=\bar{W}+w' \\
p&=\bar{P}+p', & T&=\bar{T}+T', & \rho&=\bar{\rho}+\rho' \\
\mu&=\bar{\mu}+\mu', & \lambda&=\bar{\lambda}+\lambda', & k&=\bar{k}+k'
\end{aligned} \tag{2.5}
$$

where bars denote the mean-flow quantities and primes denote disturbances.

Substituting Equation (2.5) into Equation (2.1) - (2.4) and then subtracting the governing equations of the mean flow, we yield the governing equation for small perturbations:

$$\begin{aligned} C_t \frac{\partial \phi}{\partial t} + C_x \frac{\partial \phi}{\partial x} + C_y \frac{\partial \phi}{\partial y} + C_z \frac{\partial \phi}{\partial z} + C_0 \phi = {} & C_{xx} \frac{\partial^2 \phi}{\partial x^2} + C_{xy} \frac{\partial^2 \phi}{\partial x \partial y} \\ & + C_{yy} \frac{\partial^2 \phi}{\partial y^2} + C_{xz} \frac{\partial^2 \phi}{\partial x \partial z} + C_{yz} \frac{\partial^2 \phi}{\partial y \partial z} + C_{zz} \frac{\partial^2 \phi}{\partial z^2} + F_n \end{aligned} \tag{2.6}$$

where ϕ denotes the perturbation vector and $\phi = [u', v', p', T', w']^T$ (the superscript T denotes the operator of the transpose), the matrix C_i (i stands for the subscripts in Equation (2.6) for simplicity) contains 5×5 elements and are evaluated by the mean-flow quantities, F_n denotes the nonlinear term. In this study, the nonlinear term is neglected, therefore $F_n = 0$.

We assume the disturbance vector ϕ can be expressed as

$$\phi(x, y, z, t) = \psi(y) e^{i(\alpha x + \beta z - \omega t)} \tag{2.7}$$

where α and β stand for the streamwise and spanwise wavenumbers, respectively, ω denotes the frequency, ψ is the eigenfunction vector given by

$$\psi = \left[\hat{u}, \hat{v}, \hat{p}, \hat{T}, \hat{w}\right]^T \tag{2.8}$$

where hats represent the eigenfunction. Substituting Equation (2.7) into Equation (2.6), we yield

$$\tilde{C}_0 \psi + \tilde{C}_x \frac{\partial \psi}{\partial x} + \tilde{C}_y \frac{\partial \psi}{\partial y} = C_{xx} \frac{\partial^2 \psi}{\partial x^2} + C_{xy} \frac{\partial^2 \psi}{\partial x \partial y} + C_{yy} \frac{\partial^2 \psi}{\partial y^2} \tag{2.9}$$

where the matrix $\tilde{C}_0$, $\tilde{C}_x$ and $\tilde{C}_y$ are given by

$$\tilde{C}_0 = -i\omega C_t + C_0 + i\alpha C_x + i\beta C_z + \alpha^2 C_{xx} + \alpha\beta C_{xz} + \beta^2 C_{zz}$$

$$\tilde{C}_x = C_x - 2i\alpha C_{xx} - i\beta C_{xz}$$

$$\tilde{C}_y = C_y - i\alpha C_{xy} - i\beta C_{yz}$$

We assume the local boundary layer is quasi-parallel, which means the derivative in the streamwise direction is negligible, then Equation (2.9) reduces to

$$\tilde{C}_0 + \tilde{C}_y \frac{\partial \psi}{\partial y} - C_{yy} \frac{\partial^2 \psi}{\partial y^2} = 0 \tag{2.10}$$

The explicit form of Equation (2.10) is given in Appendix A, in which the bars representing mean quantities are dropped for simplicity. The boundary conditions for Equation (2.10) are

$$\begin{array}{ll} \hat{u} = \hat{w} = \hat{T} = 0, \hat{v} = A\hat{p}, & y = 0 \\ \hat{u} = \hat{v} = \hat{w} = \hat{T} = 0, & y \to \infty \end{array} \tag{2.11}$$

where A represents the admittance of porous walls. For the smooth solid wall, A is equal to zero. Then Equation (2.10) and (2.11) constitute the dispersion relation for small disturbances propagating in boundary layers. For a temporal problem, the wavenumbers α and β are given and ω is unknown, while for a spatial problem, ω and wave propagation angle $\arctan(\beta/\alpha_r)$ (or β) are given and α is unknown. The unknown parameter is a complex number and can be solved using local or global methods [46, 58-61]. In this study, we consider the spatial problem. The growth rate of an eigenmode is $-\alpha_i$. If $\alpha_i < 0$, the mode is unstable.

2.1.2 Self-similar Solution of Boundary Layer Flow

For the flat-plate boundary layer, mean-flow variables can be obtained via a self-similar solution or by computational fluid dynamics (CFD). Here we describe the self-similar solution.

The governing equations for a flat-plate boundary layer can be derived using the

Mangler-Levy-Lees transformation,

$$\begin{aligned} d\xi &= \rho_e \mu_e U_e r^{2j} dx \\ d\eta &= \frac{U_e r^j}{\sqrt{2\xi}} \rho dy \end{aligned} \tag{2.12}$$

where subscript e denotes the boundary layer edge, r body radius, $j = 0$ for a two-dimensional boundary layer, and $j = 1$ for an axisymmetric body. The governing equations in the $\xi - \eta$ coordinates can be written as [62]:

$$(cf'')' + ff'' = 0 \tag{2.13}$$

$$(a_1 g' + a_2 f' f'')' + fg' = 0 \tag{2.14}$$

where

$$\begin{gathered} f'(\eta) = \frac{u}{U_e}, \quad g(\eta) = \frac{H}{H_e}, \quad c = \frac{\rho\mu}{\rho_e \mu_e}, \\ a_1 = \frac{c}{Pr}, \quad a_2 = c\left(1 - \frac{1}{Pr}\right) \frac{(\gamma - 1)M_e^2}{1 + \frac{1}{2}(\gamma - 1)M_e^2}, \\ \frac{\rho_e}{\rho} = \left(1 + \frac{1}{2}(\gamma - 1)M_e^2\right) g - \frac{1}{2}(\gamma - 1)M_e^2 f'^2 \end{gathered}$$

and H, Pr, γ, and M denote the total enthalpy, Prandtl number, specific heat ratio, and Mach number, respectively. The boundary conditions for Equations (2.13) and (2.14) are

$$\eta = 0\text{:} \quad f = f' = 0, \quad g = g_w \text{ (or } g' = 0 \text{ for adiabatic wall)} \tag{2.15}$$

$$\eta \to \infty\text{:} \quad f' = 1, \quad g = 1 \tag{2.16}$$

The Equations (2.13) and (2.14) with the boundary conditions (2.15) and (2.16) can be numerically solved using Newton's iteration and Runge-Kutta methods.

2.2 Numerical Method

The governing equations for the numerical simulation are the two-dimensional Navier-Stokes equations. In Cartesian coordinates, the governing equations written in a conservative form are given by

$$\frac{\partial U}{\partial t}+\frac{\partial(F-F_\nu)}{\partial x}+\frac{\partial(G-G_\nu)}{\partial y}=0 \tag{2.17}$$

where U is the vectors of flow variables, F and F_ν the vectors of inviscid and viscous flux in the streamwise direction, respectively, G and G_ν the vectors of inviscid and viscous flux in the wall-normal direction, respectively. The components of the above vectors are given by

$$\begin{gathered}
U=\begin{pmatrix}\rho\\ \rho u\\ \rho v\\ e\end{pmatrix},\quad F=\begin{pmatrix}\rho u\\ \rho u^2+p\\ \rho uv\\ (e+p)u\end{pmatrix},\quad F_\nu=\begin{pmatrix}0\\ \tau_{xx}\\ \tau_{xy}\\ u\tau_{xx}+v\tau_{xy}-q_x\end{pmatrix}\\
G=\begin{pmatrix}\rho v\\ \rho uv\\ \rho v^2+p\\ (e+p)v\end{pmatrix},\quad G_v=\begin{pmatrix}0\\ \tau_{xy}\\ \tau_{yy}\\ u\tau_{xy}+v\tau_{yy}-q_y\end{pmatrix}
\end{gathered} \tag{2.18}$$

where

$$\begin{gathered}
e=\rho\left(C_vT+\frac{1}{2}u^2+\frac{1}{2}v^2\right)\\
\tau_{xx}=2\mu\frac{\partial u}{\partial x}-\frac{2}{3}\mu\left(\frac{\partial u}{\partial x}+\frac{\partial v}{\partial y}\right),\tau_{xy}=\tau_{yx}=\mu\left(\frac{\partial u}{\partial y}+\frac{\partial v}{\partial x}\right),\\
\tau_{yy}=2\mu\frac{\partial v}{\partial y}-\frac{2}{3}\mu\left(\frac{\partial u}{\partial x}+\frac{\partial v}{\partial y}\right),\ q_x=-k\frac{\partial T}{\partial x},\ q_y=-k\frac{\partial T}{\partial y}
\end{gathered}$$

where C_v is the specific heat capacity at constant volume and k denotes the heat conductivity coefficient. The Stokes' hypothesis is employed in the numerical simulations, too. The dynamic viscosity coefficient is calculated using Sutherlands law

$$\mu=\mu_{ref}\left(\frac{T}{T_{ref}}\right)^{\frac{3}{2}}\frac{T_{ref}+S}{T+S} \tag{2.19}$$

where $\mu_{ref}=1.716\times10^{-5}\mathrm{kg(ms)^{-1}}$, $T_{ref}=273.15\mathrm{K}$ and $S=110.4\mathrm{K}$. The heat conductivity coefficient k is obtained via a constant Prandtl number. The governing equations are closed by the equation of state of an ideal gas (i.e., Equation (2.4))

Equations (2.17) are numerically solved using high-order finite-difference schemes. The fifth-order upwind scheme is utilized to discretize the inviscid convective flux terms, and the fourth-order central difference scheme is applied to the discretization of the viscous flux terms. The temporal integration is implemented using an explicit third-order Runge-Kutta method. This approach has been successfully utilized to compute the stability problem of a hypersonic boundary layer over a blunt cone [63, 64].

In the unsteady simulations, disturbances are induced by a blowing-suction actuator, which is given by

$$q_m'(x,t) = \frac{\rho_w v_w}{\rho_\infty U_\infty} = \varepsilon \sin\left(2\pi \frac{x - x_1}{x_2 - x_1}\right) \sin(\omega t)\ , \ \ x_1 \le x \le x_2 \tag{2.20}$$

where ε is the disturbance magnitude and ω is the disturbance circular frequency. When a porous wall is employed, the porous wall boundary condition is given by [36]

$$v_w(x,t) = p_w'(x,t)\mathrm{Real}(A) - \frac{1}{\omega}\frac{\partial p_w'(x,t)}{\partial t}\mathrm{Imag}(A) \tag{2.21}$$

where $p_w'(x,t)$ is the pressure perturbation and $p_w'(x,t) = p_w(x,t) - p_w(x,0)$, $\mathrm{Real}(A)$ and $\mathrm{Imag}(A)$ represent the real part and imaginary part of the admittance A of the porous wall, respectively. In the right-hand side of Equation (2.21), the negative sign of the second term is due to the assumption that the time dependence of normal incident waves is in the form of $\exp(-i\omega t)$.

To compare DNS and LST results, the growth rate and phase speed of fluctuations can be determined by

$$-\alpha_i = \frac{1}{|p_w'|}\frac{d|p_w'|}{dt} \tag{2.22}$$

$$c = \omega \frac{dx}{d\varphi} \tag{2.23}$$

where $|p_w'|$ is the wall pressure perturbation magnitude and φ the phase angle, which are obtained using Fast Fourier Transform (FFT). It should be noted that the imaginary part of the complex vector obtained from FFT needs to change its sign to compare with LST results as the time dependence in FFT is in the form of $\exp(i\omega t)$, which is contrary to the form of $\exp(-i\omega t)$ used in LST calculations.

Chapter 3 Theoretical Studies on the Effects of Porous Wall on Hypersonic Boundary Layer Instabilities

This chapter describes the effect of porous walls on the stability of a hypersonic boundary layer flow. Previous works on the stabilization of hypersonic boundary layers mainly focus on the stabilization of the second mode. In this study, both the first and second modes are considered. For the first mode, oblique waves are the most unstable. Therefore, three-dimensional instabilities are also taken into account in this chapter.

A flat-plate boundary layer is employed in this chapter and the flow parameters utilized in computations are: Mach number $M_e = 6$, Reynolds number $R = 2000$, Prandtl number $Pr = 0.72,$ and specific gas ratio $\gamma = 1.4$. The dynamic viscosity μ is calculated using a power law $\frac{\mu}{\mu_e} = \left(\frac{T}{T_e}\right)^n$ with $n = 0.7$. The wall is assumed to be insulated. In this chapter, all the quantities are non-dimensional. Velocity, density, temperature, and other variables are nondimensionalized by their corresponding values of the mean flow at the boundary layer edge, pressure by $\rho_e^* {U_e^*}^2$, all the lengths by $l^* = \sqrt{\mu_e^* x^* / (\rho_e^* U_e^*)}$, and time by l^*/U_e^*. The velocity and pressure profiles of the basic flow are obtained from a self-similar solution, and the calculated non-dimensional boundary layer thickness is equal to 16.

In this study, the terminology of discrete modes proposed by Fedorov and Tumin [65] is also adopted. The discrete modes consist of fast and slow modes, which originate from the acoustic modes near the leading edge with different propagation speeds. Generally, the slow mode is unstable for adiabatic walls while the fast mode is unstable if the wall is very cold [65]. Without specific notation, the unstable modes in this chapter belong to the slow mode.

3.1 Effect of Admittance on the first and second modes

Previous theoretical studies on the second-mode stabilization and the design of UAC particularly emphasize the significance of the reflection coefficient which represents the absorptive capacity of a UAC. As aforementioned, this parameter is a function of disturbance frequency, admittance, or impedance. In this section, a given admittance $A = |A| \exp(i\theta)$ is imposed to substitute for a realistic structure of a porous wall. The admittance magnitude $|A|$ essentially depends on the porous wall conditions and the frequency of incident waves. For instance, the non-dimensional admittance magnitude of a configuration analogous to that presented in Ref [32] can be as large as 9. The admittance phase treated in this section is in the range of $[0.5\pi, 1.5\pi]$ which includes all the admittance phases of the UACs reported in Ref. [31, 34, 37, 66].

3.1.1 Admittance Phase

We first consider the effects of the admittance phase on the first and second modes. Here we set $|A| = 4$. The contour of the growth rate as a function of the admittance phase and the non-dimensional angular frequency is illustrated in Figure 3.1. Moreover, five typical admittance phases $\theta = 0.5\pi,\ 0.75\pi,\ \pi,\ 1.25\pi$, and 1.5π are chosen to distinctly compare their performance on the first and second modes, as depicted in Figure 3.2.

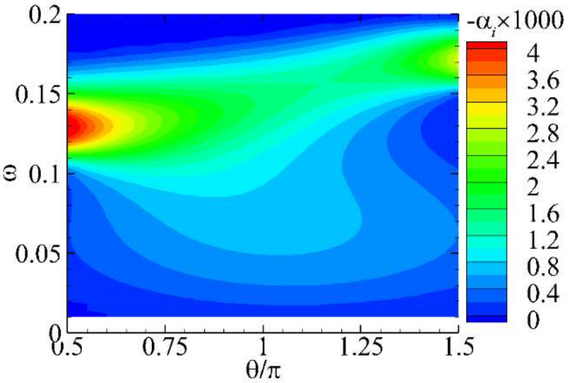

Figure 3.1 Contour of growth rate under the admittance with its phase in the range of $[0.5\pi, 1.5\pi]$ and its magnitude of $|A| = 4$.

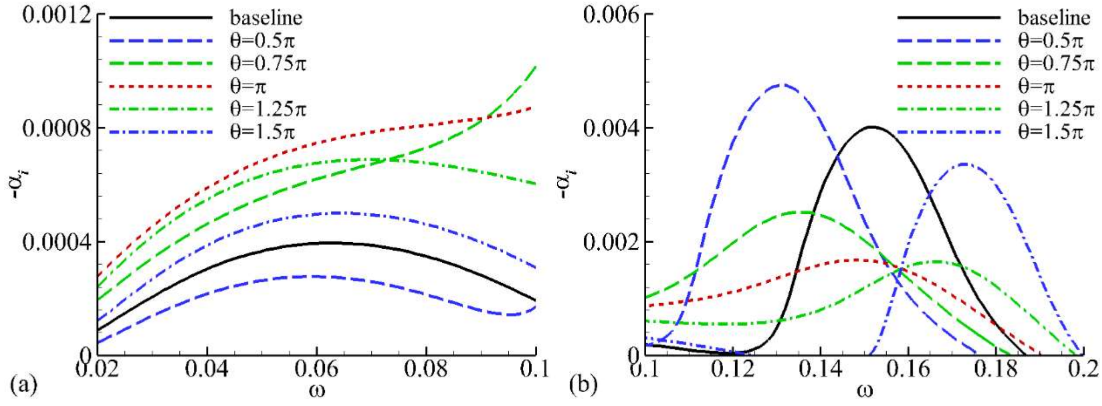

Figure 3.2 Growth rate of (a) the first mode and (b) the second mode under different admittance phases. The admittance magnitude is $|A| = 4$. Baseline denotes the smooth-solid-wall case, which is the same for the following figures.

Figure 3.1 shows the admittance phase is significant for the growth rate of the first and second modes as well as the non-dimensional angular frequency of the second mode. Concerning the first mode, the maximum growth rate of the first mode decreases at $\theta = 0.5\pi$, which is consistent with the finding by Carpenter and Porter [43], while when the admittance phase is close to π, the first mode is destabilized and according to Figure 3.2(a) its maximum growth rate is practically doubled compared with the baseline. By contrast, the second mode is damped remarkably as the admittance phase is a little larger than π, but is destabilized when $\theta = 0.5\pi$ and $\theta = 1.5\pi$.

Unlike the first mode, Figure 3.1 and Figure 3.2(b) clearly show that the spectra of the second mode shift remarkably when the admittance phase tends to 0.5π or 1.5π. For the case that the admittance phase approaches 0.5π, the frequency of the peak growth rate shifts to a lower frequency band compared with the baseline. While for the case that the admittance phase tends to 1.5π, the frequency of the peak growth rate shifts in an inverse direction.

Figure 3.2(b) illustrates the peak growth rate of the second mode at $\theta = 1.5\pi$ is lower than that of the baseline case, however, disturbances in this scenario may still be significantly amplified. As the non-dimensional angular frequency is a function of frequency f^* and position x^*, namely $\omega = \frac{2\pi f^*}{U_e^*}\sqrt{\frac{x^*}{Re}}$, for a certain perturbation frequency f^*, the second-mode waves are amplified in a long distance due to large ω.

The above conclusions indicate that for the stabilization of the first mode, the admittance phase should be close to 0.5π, while for the stabilization of the second mode, the admittance phase close to π is favorable.

3.1.2 Admittance Magnitude

The effect of admittance magnitude on the amplification of the first and second modes is examined at five typical admittance phases $\theta = 0.5\pi, 0.75\pi, \pi, 1.25\pi,$ and 1.5π. The growth rate varied along with the non-dimensional angular frequency under different admittance phases is depicted in Figure 3.3.

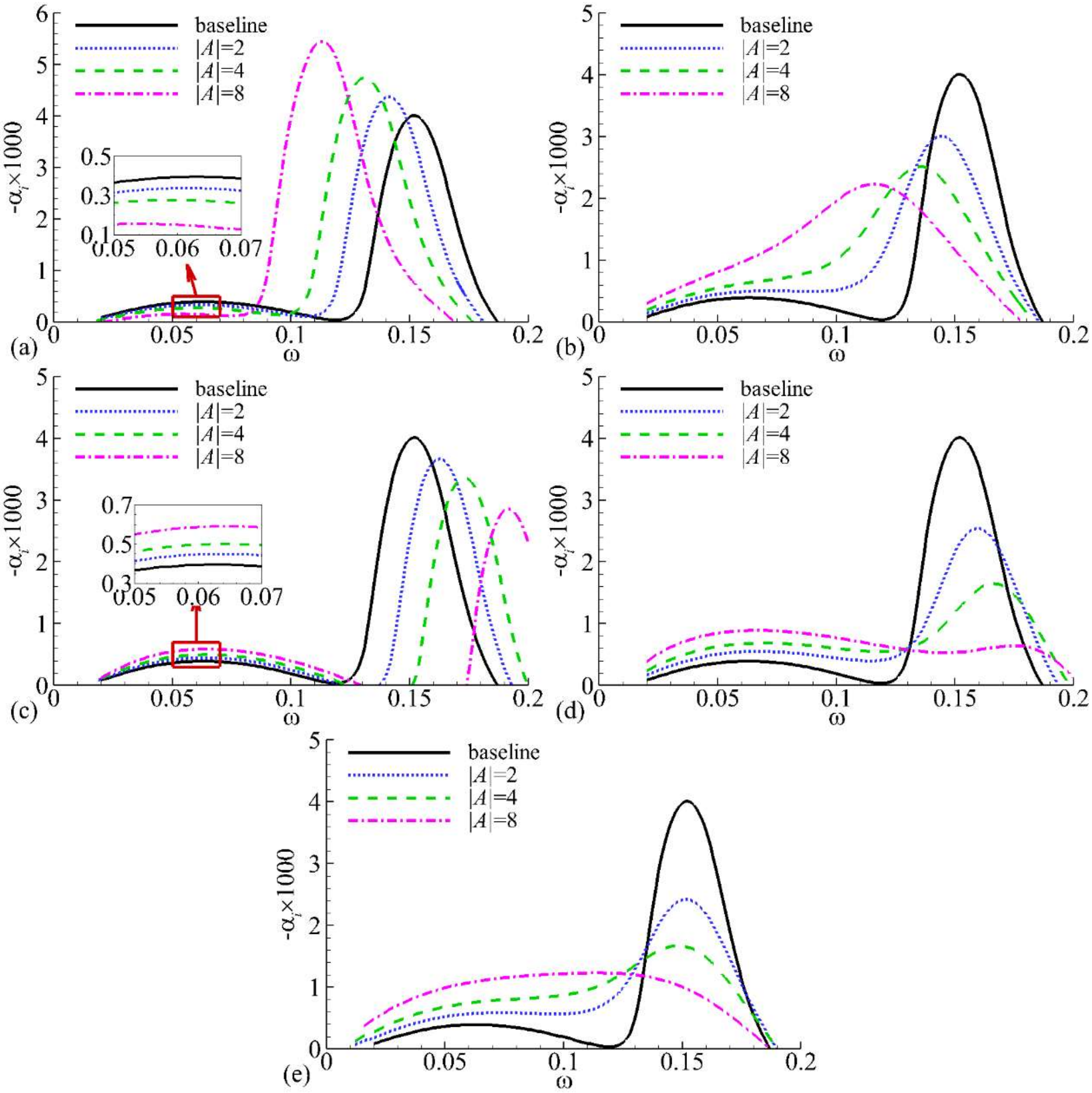

Figure 3.3 Growth rate of the first and second modes at the admittance phases of (a) $\theta = 0.5\pi$, (b) $\theta = 0.75\pi$, (c) $\theta = 1.5\pi$, (d) $\theta = 1.25\pi$ and (e) $\theta = \pi$.

It can be observed from Figure 3.3 that, for each admittance phase, the increase in the admittance magnitude has a monotonic influence on the growth rate of the first and second modes and the frequency shift of the second mode. It is evident that the increase in the admittance magnitude consolidates the stabilization or destabilization effects on the first and second modes caused by porous walls with a fixed admittance phase. Figure 3.3 also demonstrates a large admittance magnitude contributes to the mode merging as the admittance phase is about in the range of $0.75\pi \leq \theta \leq \pi$, as depicted in Figure 3.3 (b) (d) and (e). The merging of the first and second modes results in a wide frequency band for unstable disturbances, which is detrimental to the stabilization of hypersonic boundary layers.

Figure 3.3 reveals that for the design of UAC, the admittance magnitude should be carefully handled in the case that the mixed mode dominates the linear growth of fluctuations. Pervious design guidelines strive to minimize the reflective coefficient, which indeed can be achieved by a large admittance magnitude and an admittance phase approximating π. Apparently, this strategy may result in deterioration of the laminar flow control.

3.2 Three-dimensional Instabilities

It is well acknowledged that the most unstable first-mode wave is the oblique wave while in terms of the second mode, the two-dimensional (2D) wave is the most amplified wave [7]. Here we investigate the effects of porous walls on the three-dimensional (3D) disturbances, including the first and second modes.

Figure 3.4 schematically shows the propagation of an oblique wave. The wave-propagation angle is defined by the wave propagation direction deviating from the streamwise direction, namely $\arctan(\beta/\alpha_r)$. The growth rates of the oblique waves on the solid wall are illustrated in Figure 3.5. It can be seen that the first mode becomes more unstable when the wave-propagation angle increases, while the second mode is inhibited by the increased wave-propagation angle and becomes stable when the wave-propagation angle is up to 45°.

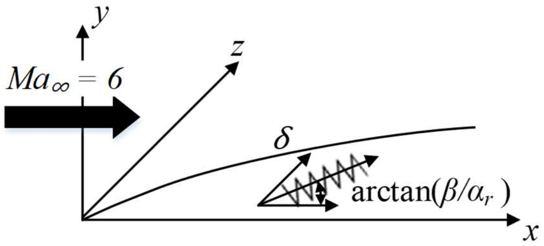

Figure 3.4 Schematic diagram of the propagation of oblique waves.

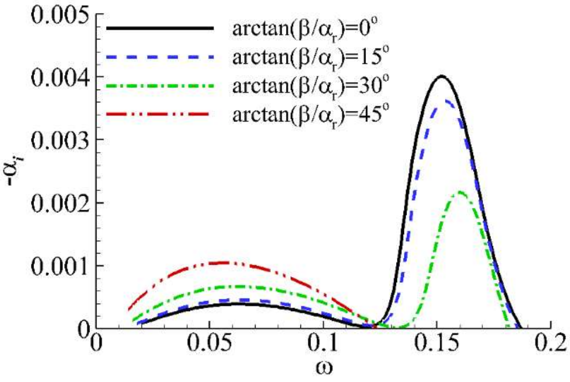

Figure 3.5 Growth rate of the first and second modes on the smooth solid wall under different wave-propagation angles $\arctan(\beta/\alpha_r)$.

3.2.1 Effect of Admittance Phase

The effect of the oblique waves is investigated under different admittance phases. Here four wave-propagation angles $\arctan(\beta/\alpha_r) = 0,\ 15^{\circ},\ 30^{\circ}$ and (d) 45° are employed. The growth rates of the first and second modes at various admittance phases are depicted in Figure 3.6.

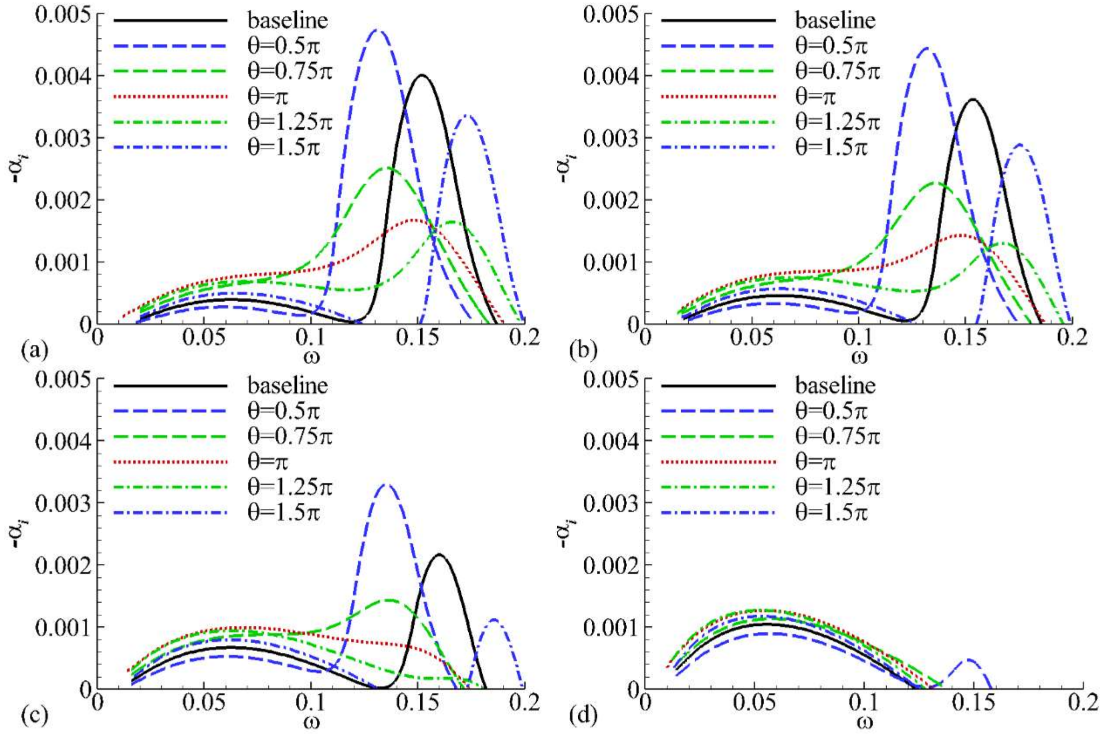

Figure 3.6 Growth rate of the oblique first- and second-mode waves at the admittance magnitude of $|A| = 4$ and admittance phase in the range of $[0.5\pi,\ 1.5\pi]$. The wave-propagation angles are: (a) $\arctan(\beta/\alpha_r) = 0$, (b) $\arctan(\beta/\alpha_r) = 15^{\mathrm{o}}$, (c) $\arctan(\beta/\alpha_r) = 30^{\mathrm{o}}$ and (d) $\arctan(\beta/\alpha_r) = 45^{\mathrm{o}}$. Baseline denotes the smooth-solid-wall case.

Compared with the 2D instabilities illustrated in Figure 3.6(a), Figure 3.6 (b) (c) and (d) show the admittance phase causes analogous effects on the 3D fluctuations. Moreover, in terms of the growth rate, the elevation of the first and the decline of the second mode along with the increase of the wave-propagation angle also emerge with porous walls employed, indicating the regularity of the effects of the wave-propagation angle on the first and second modes is not changed by porous walls. Figure 3.6(d) also shows that in the case of $\arctan(\beta/\alpha_r) = 45^{\mathrm{o}}$, the second mode which is stable in the smooth-solid-wall case, is destabilized by the porous wall with the admittance phase of $\theta = 0.5\pi$, which suggests the destabilization effect of porous walls is not modified by the wave-propagation angle. Consequently, it could be concluded that the effects of the wave-propagation angle and the admittance phase of a porous wall are independent of each other.

3.2.2 Effect of Admittance Magnitude

The previous section shows that for 2D instabilities the increase in the admittance magnitude strengthens the impact of porous walls on the first and second mode. For the 3D perturbations, the effects on the first and second modes due to the rise of the admittance magnitude are examined with a wave-propagation angle of $\arctan(\beta/\alpha_r) = 30^{\circ}$ employed. The comparisons between the 2D instabilities and 3D instabilities under two typical admittance phases $\theta = 0.5\pi$ and $\theta = \pi$ are depicted in Figure 3.7.

Figure 3.7(b) and 3.7(d) show, of the 3D instabilities, a large admittance magnitude facilitates the effects of porous walls on the first and second modes, which is analogous to that of the 2D instabilities. By comparing 2D instabilities and 3D instabilities under the same admittance phase, it can be seen that the regularities that the oblique first-mode waves are more unstable and the oblique second-mode waves are more stable are not altered by the increase in the admittance magnitude. Therefore, it could be deduced that the effects of the wave-propagation angle and the admittance magnitude of porous walls are also independent of each other.

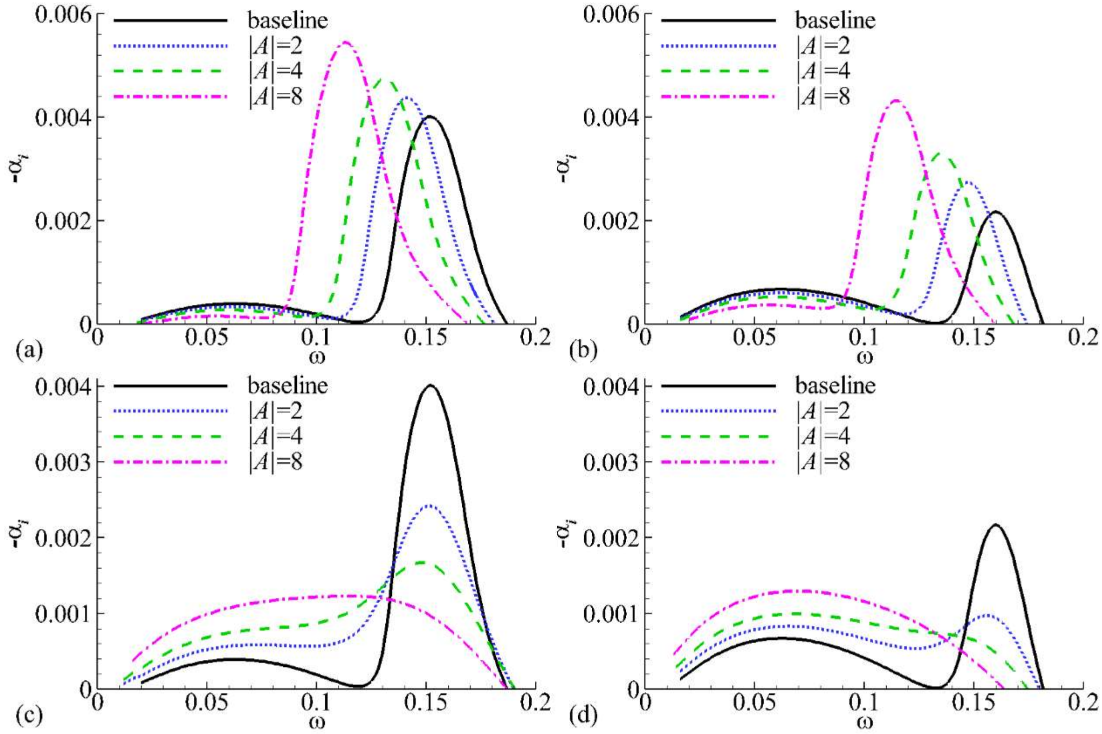

Figure 3.7 Growth rate of 2D waves (left-hand plots) and 3D waves (right-hand plots) at the admittance phase of (a) (b) $\theta = 0.5\pi$, (c) (d) $\theta = \pi$. The wave-propagation angle of the 3D waves is $\arctan\left(\frac{\beta}{\alpha_r}\right) = 30^{\circ}$.

Consequently, the effects of porous walls on the first and second modes are independent of the wave-propagation angle. When oblique waves are taken into account, the stabilization of the oblique first-mode waves requires considerably large admittance magnitude.

3.3 Reversal of Unstable Modes

A porous wall composed by regular or random microstructures for normal incident waves commonly has an admittance phase in the range of $[0.5\pi, 1.5\pi]$. Up to now, the effect of the admittance phase beyond this range has not been investigated before. Here we consider the admittance phase beyond this range to examine its effects on the eigenmode of hypersonic boundary layers. For simplicity, we continue to use “porous wall” to denominate such a semi-transparent wall.

Figure 3.8 illustrates the effects of porous walls with an admittance phase of $\theta = 0$ on the fast and slow modes. It can be seen from Figure 3.8 (a) that in the track of the growth rate, the fast and slow modes are flipped over when the admittance magnitude exceeds a threshold. Figure 3.8(b) shows that the phase-speed branches of the fast and slow modes are also interchanged across the synchronization point. Moreover, the peak growth rate of the unsteady mode keeps growing along with the increase of the admittance magnitude.

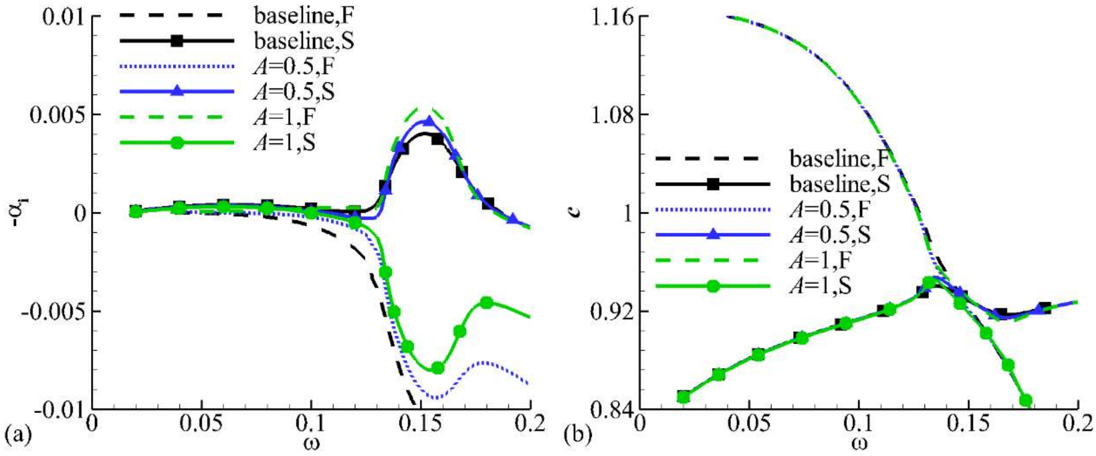

Figure 3.8 (a) Growth rate and (b) phase speed of the fast (F) and slow (S) modes under different admittances with the admittance of $\theta = 0$.

The reversal of unstable modes due to porous walls with a phase of $\theta = 0$ also emerges in the range of $\theta \in (-0.5\pi,\ 0.5\pi)$, where the real part of admittance is positive, as shown in Figure 3.9. It indicates that the real part of admittance is significant for the eigenmode branch. When it is negative or of a little positive value, the fast mode is stable, and the slow mode is unstable. If it is positive and exceeds a threshold, a contrary scenario is manifested.

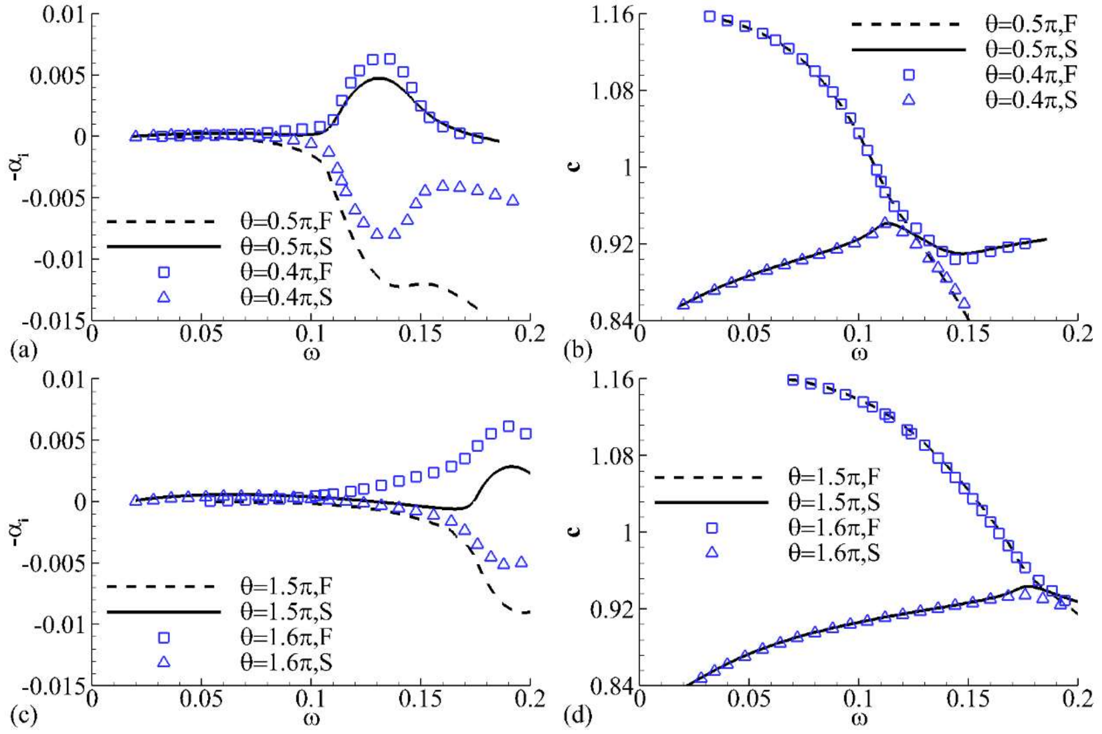

Figure 3.9 Growth rate (left-hand plot) and phase speed (right-hand plot) of the fast and slow modes under different admittance phases with admittance magnitude of $|A| = 4$.

3.4 Simplified Linear Stability Equations

The eigenvector of an eigenmode within supersonic/hypersonic boundary layers can provide the shape information of a disturbance component. Substituting the eigenvector and eigenvalue obtained from LST calculations to the linear stability equation (2.10), we can simplify the linear stability equations.

Here we employ the mode at $\omega = 0.152$ with $\alpha = 0.164 - 0.004i$ and $\beta = 0$, which is the most unstable second mode under the current boundary layer, as an instance to simplify Equation (2.10). The components of the eigenvector are depicted in Figure 3.10. Each term in Equation (2.10) is evaluated, and then the explicit form of Equation (2.10) (see Appendix A) for 2D boundary layer flow ($W = 0$) can be recasted as followings:

$$\frac{1}{T}(i\alpha U - i\omega)\hat{u} = -\frac{dU}{dy}\frac{\hat{v}}{T} - i\alpha\hat{p} + \frac{1}{R}\frac{d}{dy}\left(\mu\frac{d\hat{u}}{dy} + \frac{dU}{dy}\frac{d\mu}{dT}\hat{T}\right) + res. \tag{3.1}$$

$$\frac{1}{T}(i\alpha U - i\omega)\hat{v} = -\frac{d\hat{p}}{dy} + \frac{4}{3R}\frac{d}{dy}\left(\mu\frac{d\hat{v}}{dy}\right) + res. \tag{3.2}$$

$$\frac{1}{T}(i\alpha U - i\omega)\hat{w} = -i\beta\hat{p} + \frac{1}{R}\frac{d}{dy}\left(\mu\frac{d\hat{w}}{dy}\right) + res. \tag{3.3}$$

$$\begin{aligned}\frac{1}{T}(i\alpha U - i\omega)\hat{T} = -\frac{dT}{dy}\frac{\hat{v}}{T} - (\gamma - 1)\left(i\alpha\hat{u} + \frac{d\hat{v}}{dy} + i\beta\hat{w}\right)\\ + \frac{\gamma}{RPr}\frac{d^2(\mu\hat{T})}{dy^2} + res.\end{aligned} \tag{3.4}$$

where $res.$ denotes the residual terms. The first three equations (3.1) – (3.3) are the linearized disturbance momentum equations. Equation (3.4) is a rewrite of the linearized disturbance energy equation (A.4) based on the internal energy rather than enthalpy in order to reveal the internal energy variation straightforwardly.

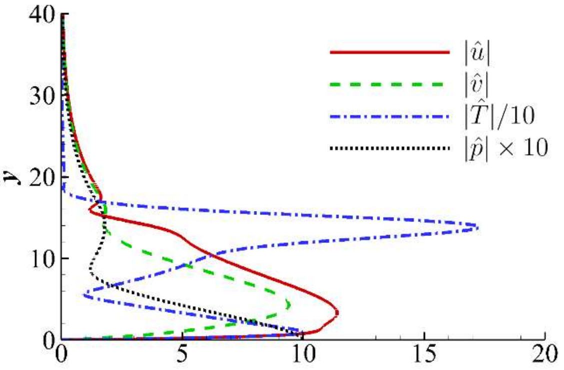

Figure 3.10 Disturbance Components of the most unstable mode of the smooth-solid-wall case with $\omega = 0.152$, $\alpha = 0.164 - 0.004i$, and $\beta = 0$. All the components are normalized by the wall-pressure-disturbance magnitude $|\hat{p}_w|$.

Essentially, the residual terms in Equations (3.1) – (3.4) are negligible for both the first and second modes, including oblique waves. Here we choose two modes from the smooth-solid-wall case at $\omega = 0.063$ and $\omega = 0.152$ with a propagation phase angle of $\arctan\left(\frac{\beta}{\alpha_r}\right) = 30^o$, which respectively represents the 3D first- and second-mode waves, for validation. The corresponding eigenvalues are $\alpha = 0.071 - 0.00067i$ and $\alpha = 0.163 - 0.0017i$, respectively. The magnitudes of the terms in Equations (3.1) – (3.4) are examined for the first and second modes and their profiles along y coordinate are illustrated in Figure 3.11 and Figure 3.12, respectively.

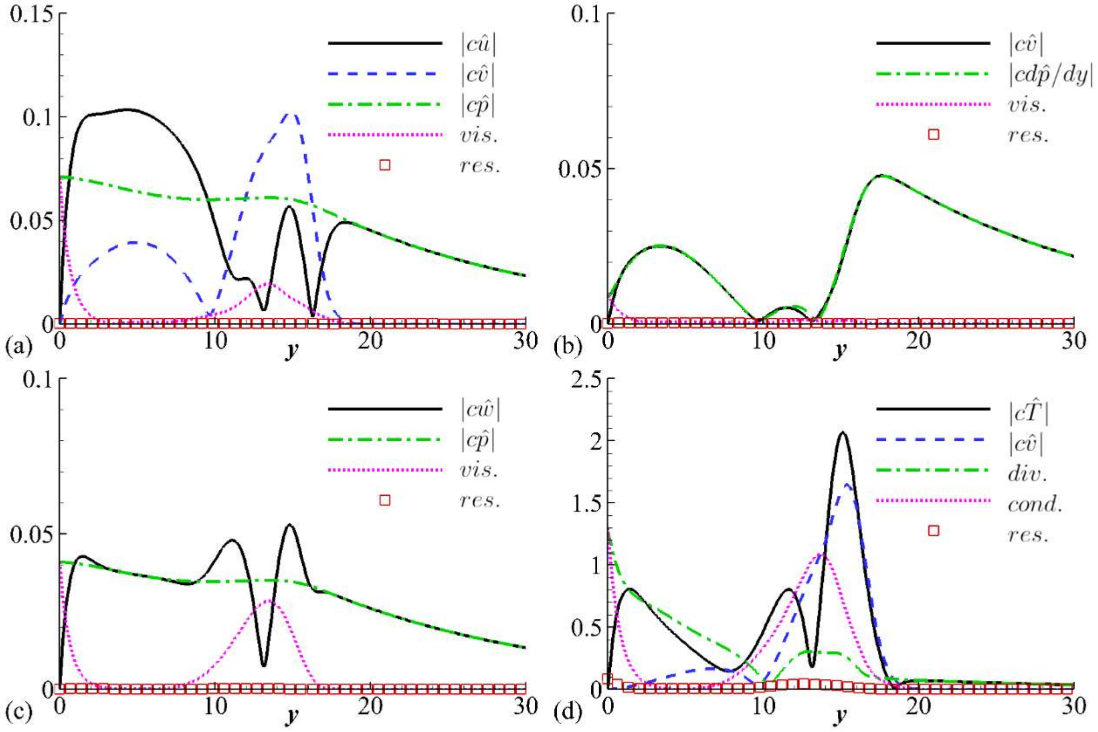

Figure 3.11 Magnitudes of the terms in Equation (3.1)-(3.4) at $\omega = 0.063$ with $\arctan\left(\frac{\beta}{\alpha_i}\right) = 30^o$ and eigenvalue of $\alpha = 0.071 - 0.00067i$: (a) Equation (3.1), (b) Equation (3.2), (c) Equation (3.3), and (d) Equation (3.4). Here c denotes the coefficient of each term, $vis.$ the viscous term in the disturbance momentum equations, $res.$ the sum of the absolutes of the residual terms, $div.$ the term

$-(\gamma-1)\left(i\alpha\hat{u}+\frac{\partial\hat{v}}{\partial y}+i\beta\hat{w}\right)$ and $cond.$ the thermal conduction term $\frac{\gamma}{RPr}\frac{d^2(\mu\hat{T})}{dy^2}$.

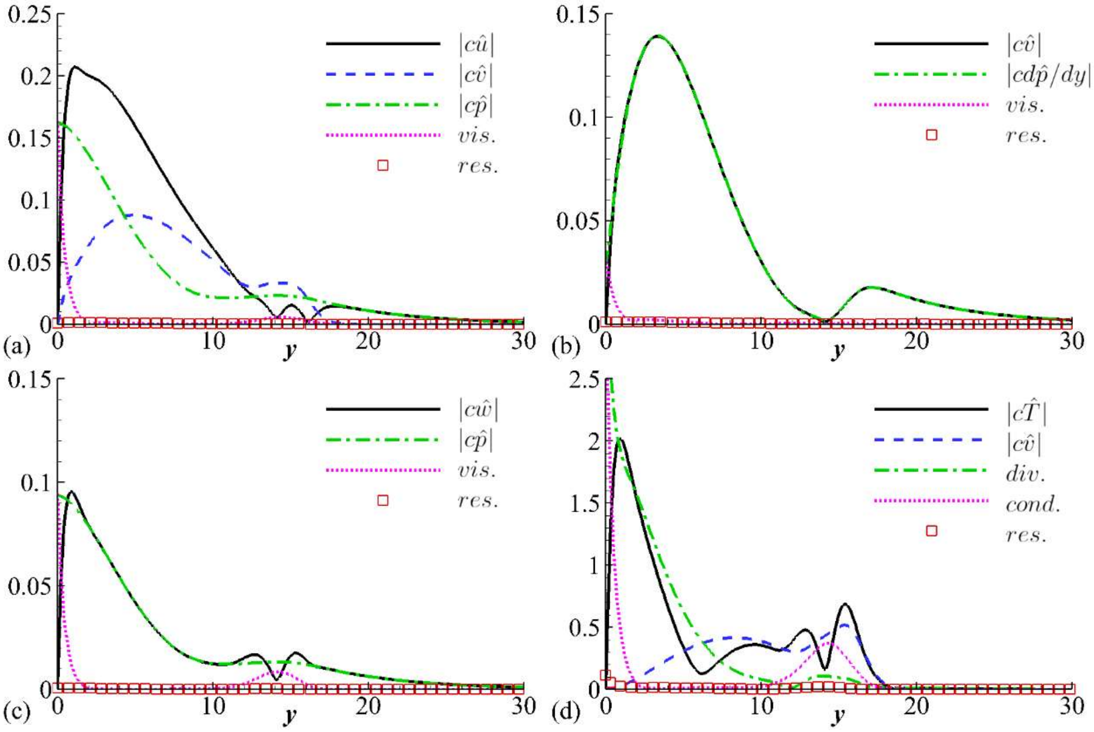

Figure 3.12 Magnitudes of the terms in Equation (3.1)-(3.4) at $\omega = 0.152$ with $\arctan\left(\frac{\beta}{\alpha_i}\right) = 30^o$ and eigenvalue of $\alpha = 0.164 - 0.0017i$,: (a) Equation(3.1), (b) Equation(3.2), (c) Equation(3.3) and (d) Equation(3.4). Here the legends are the same with those in Figure 3.11.

Figure 3.11 and 3.12 show, both for the first and second mode, the magnitudes of the residual terms of Equation (3.1) – (3.4) are fairly small along y coordinate except the magnitude of the residual of Equation (3.4) at the wall. But it is negligible in contrast to the magnitudes of the terms $\frac{\gamma}{RPr}\frac{d^2(\mu\hat{T})}{dy^2}$ and $-(\gamma-1)\left(i\alpha\hat{u}+\frac{\partial\hat{v}}{\partial y}+i\beta\hat{w}\right)$ at the wall, as shown in Figure 3.12 (d). Therefore, Equations (3.1) – (3.4) can be reduced to

$$\frac{1}{T}(i\alpha U - i\omega)\hat{u} = -\frac{dU}{dy}\frac{\hat{v}}{T} - i\alpha\hat{p} + \frac{1}{R}\frac{d}{dy}\left(\mu\frac{d\hat{u}}{dy} + \frac{dU}{dy}\frac{d\mu}{dT}\hat{T}\right) \tag{3.5}$$

$$\frac{1}{T}(i\alpha U - i\omega)\hat{v} = -\frac{d\hat{p}}{dy} + \frac{4}{3R}\frac{d}{dy}\left(\mu\frac{d\hat{v}}{dy}\right) \tag{3.6}$$

$$\frac{1}{T}(i\alpha U - i\omega)\hat{w} = -i\beta\hat{p} + \frac{1}{R}\frac{d}{dy}\left(\mu\frac{d\hat{w}}{dy}\right) \tag{3.7}$$

$$\begin{aligned}\frac{1}{T}(i\alpha U - i\omega)\hat{T} = {} & -\frac{dT}{dy}\frac{\hat{v}}{T} - (\gamma - 1)\left(i\alpha\hat{u} + \frac{d\hat{v}}{dy} + i\beta\hat{w}\right) \\ & + \frac{\gamma}{RPr}\frac{d^2(\mu\hat{T})}{dy^2}\end{aligned} \tag{3.8}$$

The continuity equation in Equation (2.10) is retained and rewritten here, as shown below

$$\gamma Ma_e^2(i\alpha U - i\omega)\hat{p} - (i\alpha U - i\omega)\frac{\hat{T}}{T} + i\alpha\hat{u} + \frac{\partial\hat{v}}{\partial y} + i\beta\hat{w} - \frac{dT}{dy}\frac{\hat{v}}{T} = 0 \tag{3.9}$$

Equations (3.5) - (3.9) are the simplified linear stability equations. In the following sections, the disturbance energy equation (3.8) is utilized to analyze the mechanisms of the amplification of the first and second modes. Therefore, it is necessary to interpret the meaning of each term of Equation (3.8). For convenience, all the energy terms henceforth represent those in disturbance flow fields. On the left side of Equation (3.8), $-i\omega\frac{\hat{T}}{T}$ denotes the time rate of change of internal energy, and $i\alpha U\frac{\hat{T}}{T}$ is heat transport by the mean flow. These two terms are significant for the change of internal energy in a finite control volume and their sum $\frac{1}{T}(i\alpha U - i\omega)\hat{T}$ is the nominal total time rate of change of internal energy. On the right side of Equation (3.8), the first term $-\frac{dT}{dy}\frac{\hat{v}}{T}$ is the heat transport by the wall-normal velocity fluctuation, the second term $-(\gamma - 1)\left(i\alpha\hat{u} + \frac{\partial\hat{v}}{\partial y} + i\beta\hat{w}\right)$ represents the energy change due to dilatation fluctuations, and the last term $\frac{1}{RPr}\frac{d^2}{dy^2}\left(\mu\hat{T}\right)$ denotes the thermal conduction.

It should be noted that $-\frac{dT}{dy}\frac{\hat{v}}{T}$ is a source term that draws energy from the mean-flow field to the disturbance-flow field. In the current boundary layer, $\frac{dT}{dy} \leq 0$ (the equality holds at the wall and the upper boundary layer edge), therefore, for a control volume in the boundary layer, the flow moving upwards brings high-temperature fluid elements into it, while the flow moving downwards brings low-temperature fluid elements into it. In this work, the simplified linear stability equations are not used to solve the eigenproblem, but to analyze the energy exchange in the boundary layer. All the eigenmodes are obtained still by resolving Equations (2.10) and (2.11).

3.5 Instabilities of the First and Second Modes

Unnikrishnan and Gaitonede [44] analyzed the energy interactions among the acoustic, vortical, and thermal components and found that the thermal component plays a great role in the growth of acoustic waves. With respect to the most unstable mode in the current boundary layer, the internal energy fluctuations around the critical layer (the phase speed of disturbances is equal to local mean-flow speed) and near the wall are comparable to the kinetic energy fluctuations sandwiched between the peaks of internal energy fluctuations, as shown in Figure 3.13. Therefore, it can be speculated that the internal energy fluctuations may influence the local instabilities.

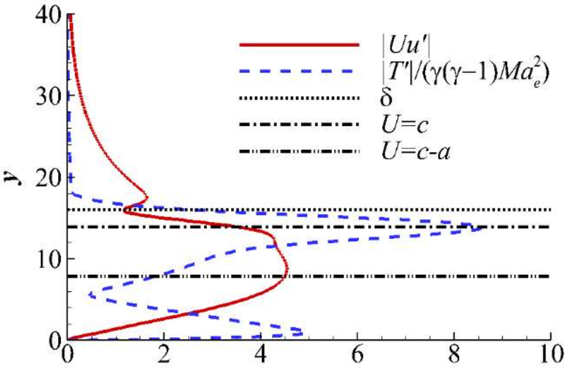

Figure 3.13 Comparison of the kinetic ($|Uu'|$) and internal energy ($|T'|/[\gamma(\gamma -$

$1)Ma_e^2]$) fluctuations of the mode at $\omega = 0.152$ with $\alpha = 0.164 - 0.004i$. Here δ denotes the boundary layer thickness, $U = c$ represents the critical layer and c is the phase speed, and $U = c - a$ is the sonic line and a is the local speed of sound.

It is well known that the Rijke tube can turn heat into sound [67]. According to Rayleigh's criterion, the excitation of acoustic waves by heat addition depends on the phase of the vibration at which heat transfer occurs. The statements are given below:

> "If heat be communicated to, and abstracted from, a mass of air vibrating (for example) in a cylinder bounded by a piston, the effect produced will depend upon the phase of the vibration at which the transfer of heat takes place. If heat be given to the air at the moment of greatest condensation, or be taken from it at the moment of greatest rarefaction, the vibration is encouraged. On the other hand, if heat be given at the moment of greatest rarefaction, or abstracted at the moment of greatest condensation, the vibration is discouraged." [68]

This motivates us to consider the phase relations of the energy terms in Equation (3.8).

3.5.1 Second-Mode Instability

We first investigate the mechanisms of the second mode instabilities in the boundary layer over the smooth solid wall. Here we consider 2D instabilities as 2D waves are more unstable than 3D waves for the second mode. We choose the modes belonging to the second mode family at different frequencies $\omega =$ 0.13, 0.152, and 0.17 for comparison. Their eigenvalues are $\alpha = 0.13884 - 0.00048i$, $0.16406 -$

$0.00401i$, and $0.18543-0.0019i$, respectively. The corresponding eigenvectors are substituted into Equation (3.8). Figure 3.14 demonstrates the magnitude and phase profiles of the left-hand side terms of Equation (3.8) and Figure 3.15 illustrates those of the right-hand side terms of Equation (3.8). Noted that all the disturbance components are normalized by the wall pressure disturbance.

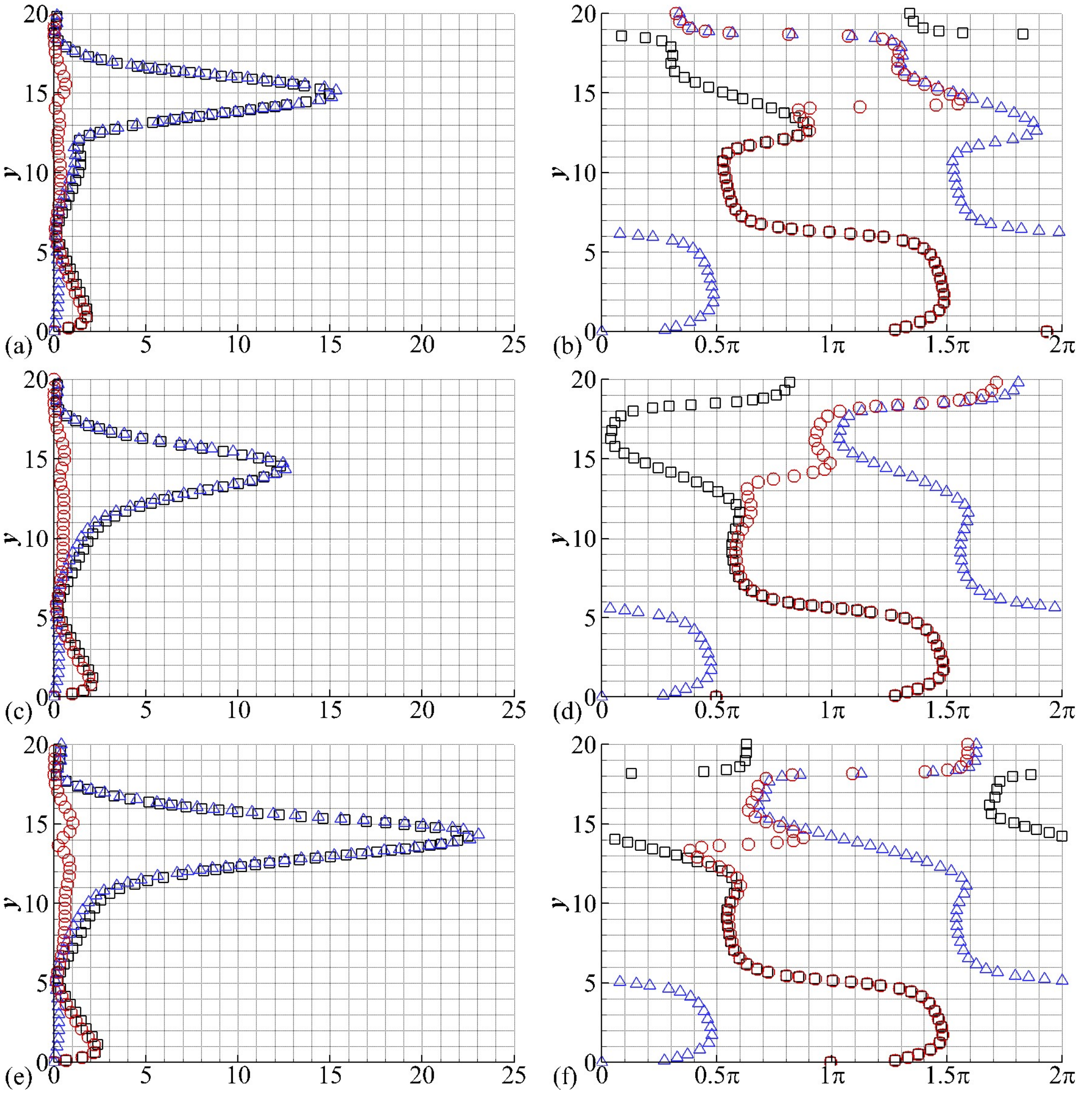

Figure 3.14 Magnitude (left-hand plots) and phase (right-hand plots) of $-i\omega\frac{\hat{T}}{T}$ (□), $i\alpha U\frac{\hat{T}}{T}$ (△) and $(i\alpha U-i\omega)\frac{\hat{T}}{T}$ (○) under different ω: (a)(b) $\omega=0.13$, $\alpha=0.13884-0.00048i$; (c)(d) $\omega=0.152$, $\alpha=0.16406-0.00401i$; (e)(f) $\omega=0.17$,

$\alpha = 0.18543 - 0.0019i$.

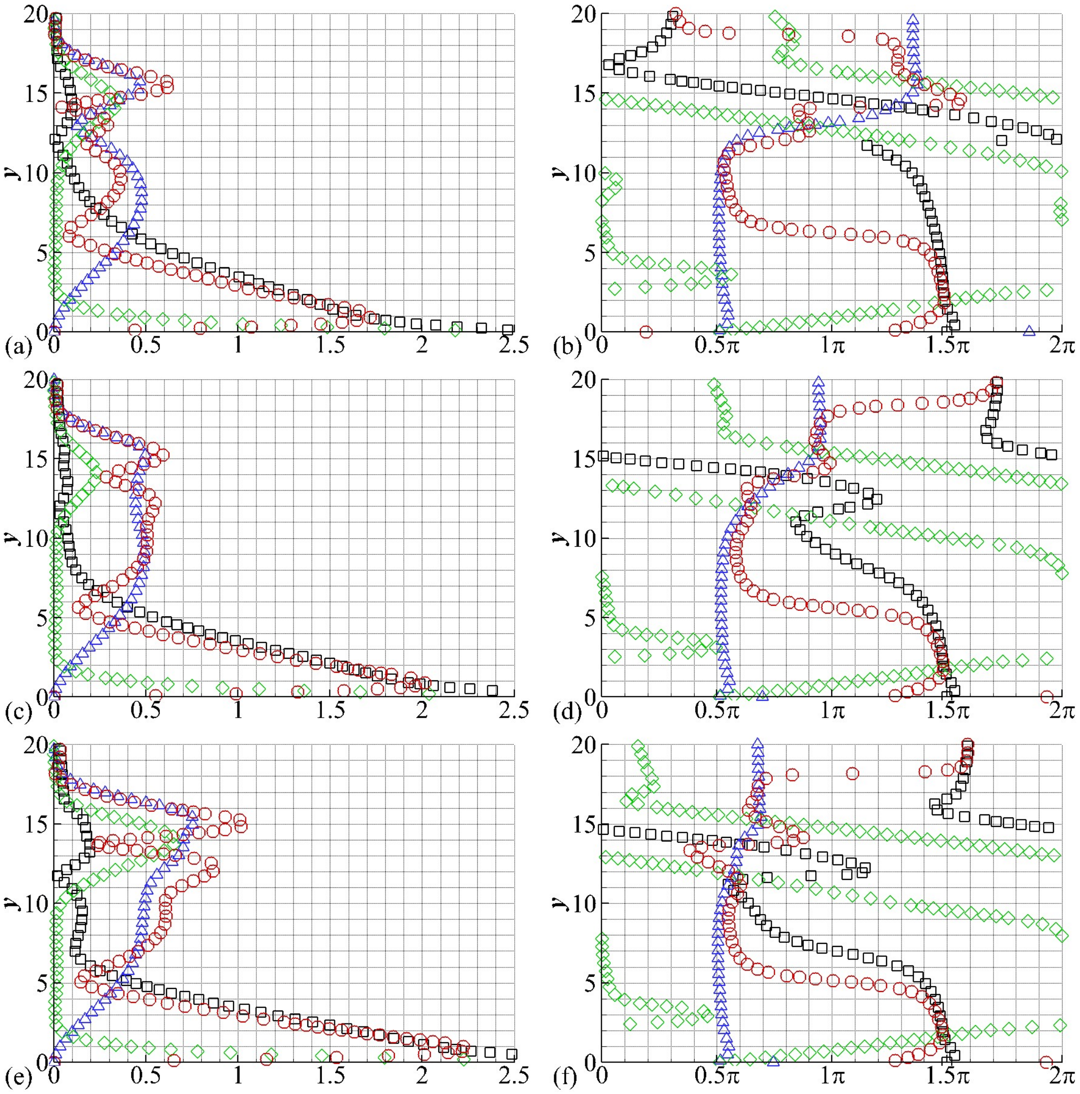

Figure 3.15 Magnitude (left-hand plots) and phase (right-hand plots) profiles of $-(\gamma-1)\left(i\alpha\hat{u}+\frac{\partial\hat{v}}{\partial y}\right)$ (□), $-\frac{dT}{dy}\frac{\hat{v}}{T}$ (△), $\frac{\gamma}{RPr}\frac{d^2}{dy^2}\left(\mu\hat{T}\right)$ (◇) and $\left(i\alpha U-i\omega\right)\frac{\hat{T}}{T}$ (○) under different ω: (a) (b) $\omega = 0.13$, $\alpha = 0.13884 - 0.00048i$; (c) (d) $\omega = 0.152$, $\alpha = 0.16406 - 0.004i$; (e) (f) $\omega = 0.17$, $\alpha = 0.18543 - 0.0019i$.

The magnitudes of $-i\omega\frac{\hat{T}}{T}$ and $i\alpha U\frac{\hat{T}}{T}$ shown in the left plots of Figure 3.14 are considerably large in the vicinity of the critical layer ($y \approx 14$ for the current three cases). As their magnitudes are comparable in this region, the magnitude of their sum $(i\alpha U - i\omega)\frac{\hat{T}}{T}$ is fairly small. It indicates the advection energy transport by the mean flow is dominant for the internal energy variation in the region around the critical layer. Since $(i\alpha U - i\omega)\frac{\hat{T}}{T} = i\alpha_r(U-c)\frac{\hat{T}}{T} - \alpha_i U\frac{\hat{T}}{T}$ and $\alpha_r \gg -\alpha_i$, the sign alteration of $U-c$ accounts for a phase shift of $(i\alpha U - i\omega)\frac{\hat{T}}{T}$ across the critical layer, as shown in the right plots of Figure 3.14.

Below the critical layer, on the left side of Equation (3.8), $(i\alpha U - i\omega)\frac{\hat{T}}{T}$ is in phase with $-i\omega\frac{\hat{T}}{T}$ and has a new phase shift, as depicted in the right plots of Figure 3.14. This phase shift corresponds to a valley in the magnitude profile of $(i\alpha U - i\omega)\frac{\hat{T}}{T}$ shown in the left plots of Figure 3.14. Below this valley, the thermal convection $i\alpha U\frac{\hat{T}}{T}$ is negligible and hence $(i\alpha U - i\omega)\frac{\hat{T}}{T} \sim -i\omega\frac{\hat{T}}{T}$. On the right side of Equation (3.8), below the phase shift of $(i\alpha U - i\omega)\frac{\hat{T}}{T}$, $(i\alpha U - i\omega)\frac{\hat{T}}{T}$ basically has the same magnitude and phase with $-(\gamma-1)\left(i\alpha\hat{u} + \frac{\partial\hat{v}}{\partial y}\right)$, excluding the region that is very close to the wall. Therefore, the dilatation fluctuation accounts for the variation of internal energy near the wall. This conclusion agrees with the experimental findings by Zhu et al. [69] that dilatation fluctuations ruled by the second mode generate intense aerodynamic heating.

Against the wall, $\frac{\gamma}{RPr}\frac{d^2}{dy^2}\left(\mu\hat{T}\right)$ has identical magnitude with $-(\gamma-1)\left(i\alpha\hat{u} + \frac{\partial\hat{v}}{\partial y}\right)$. Indeed, the thermal conduction $\frac{\gamma}{RPr}\frac{d^2}{dy^2}\left(\mu\hat{T}\right)$ is passively induced by the near-wall thermal fluctuations due to the fluctuating thermal expansion and contraction and provides energy to sustain the near-wall dilatation fluctuation.

Figure 3.15(d) shows that in the case $\omega = 0.152$ which has the largest growth rate among these three cases, $-\frac{dT}{dy}\frac{\hat{v}}{T}$ is nearly in phase with $(i\alpha U - i\omega)\frac{\hat{T}}{T}$ throughout the phase shift of $(i\alpha U - i\omega)\frac{\hat{T}}{T}$ crossing the critical layer. Moreover, Figure 3.15(c) shows $-\frac{dT}{dy}\frac{\hat{v}}{T}$ is on the same order of magnitude with $(i\alpha U - i\omega)\frac{\hat{T}}{T}$ on both the two sides of the critical layer. As $-\alpha_i$ cannot be negligible at the critical layer, its value becomes significant for the phase of $(i\alpha U - i\omega)\frac{\hat{T}}{T}$ in the vicinity of the critical layer. The large value of $-\alpha_i$ in this case is associated with a high contribution of the convective heat transfer $-\frac{dT}{dy}\frac{\hat{v}}{T}$ to the internal energy perturbation.

By contrast, in the cases $\omega = 0.13$ and $\omega = 0.17$ which have lower growth rates compared with the case $\omega = 0.152$, the phase of $(i\alpha U - i\omega)\frac{\hat{T}}{T}$ diverges from the phase of $-\frac{dT}{dy}\frac{\hat{v}}{T}$ manifestly across the critical layer, as demonstrated in Figure 3.15(b) and (f). As a result, the heat transport by the wall-normal velocity fluctuation does not synchronize with the total time rate of change of internal energy around the critical layer, which diminishes the contribution of the energy transport by the wall-normal velocity fluctuation to the local internal energy fluctuations.

Therefore, it could be concluded that the contribution of the heat transfer $-\frac{dT}{dy}\frac{\hat{v}}{T}$ to the internal energy fluctuations accounts for the amplification of the second-mode instabilities. Moreover, the relative phase of $-\frac{dT}{dy}\frac{\hat{v}}{T}$ to $(i\alpha U - i\omega)\frac{\hat{T}}{T}$ in the vicinity of the critical layer is associated with the near-wall dilatation fluctuation. When the near-wall dilatation fluctuation is intensified, the wall-normal fluctuating velocity will be accelerated, which affects the energy transport by the wall-normal velocity fluctuation in the vicinity of the critical layer. Meanwhile, the critical-layer fluctuation also influences the near-wall fluctuation by changing the wall-normal fluctuating velocity. Consequently, the near-wall fluctuation mutually interacts with the critical-layer fluctuation, which underpins the growth of second-mode instabilities.

3.5.2 First-Mode Instability

In terms of the first mode, we continue to conduct phase analysis on the simplified disturbance energy equation. Likewise, we focus on 2D instabilities in the smooth-solid-wall case. The 3D instabilities will be analyzed in the following sections. We choose three non-dimensional angular frequencies: ω =0.03, 0.063, and 0.09. and the corresponding eigenvalues are $\alpha = 0.0348 - 0.0002i$, $0.07068 - 0.00039i$, and $0.09913 - 0.00028i$, respectively. These three eigenmodes all belong to the first mode family. The magnitude and phase profiles of the left-hand side terms of Equation (3.8) are depicted in Figure 3.16 and those of the right-hand side terms of Equation (3.8) are depicted in Figure 3.17, respectively.

Analogous to the second mode, the magnitudes of $-i\omega\frac{\hat{T}}{T}$ and $i\alpha U\frac{\hat{T}}{T}$ are remarkably large across the critical layer ($y \approx 13$ for the current three cases), and only $-i\omega\frac{\hat{T}}{T}$ is significant near the wall, as shown in the left-hand plots of Figure 3.16. As $-\alpha_i$ is fairly small in these three cases, $(i\alpha U - i\omega)\frac{\hat{T}}{T}$ is in phase with $i\alpha U\frac{\hat{T}}{T}$ above the critical layer and with $-i\omega\frac{\hat{T}}{T}$ below the critical layer, as shown in the right-hand plots of Figure 3.16. Figure 3.17 (b) (d) and (f) demonstrate that across the critical layer the phase of $-\frac{dT}{dy}\frac{\hat{v}}{T}$ differs from that of $(i\alpha U - i\omega)\frac{\hat{T}}{T}$ evidently, which indicates the heat transport by the wall-normal velocity fluctuation slightly contributes to the internal energy fluctuation in this region.

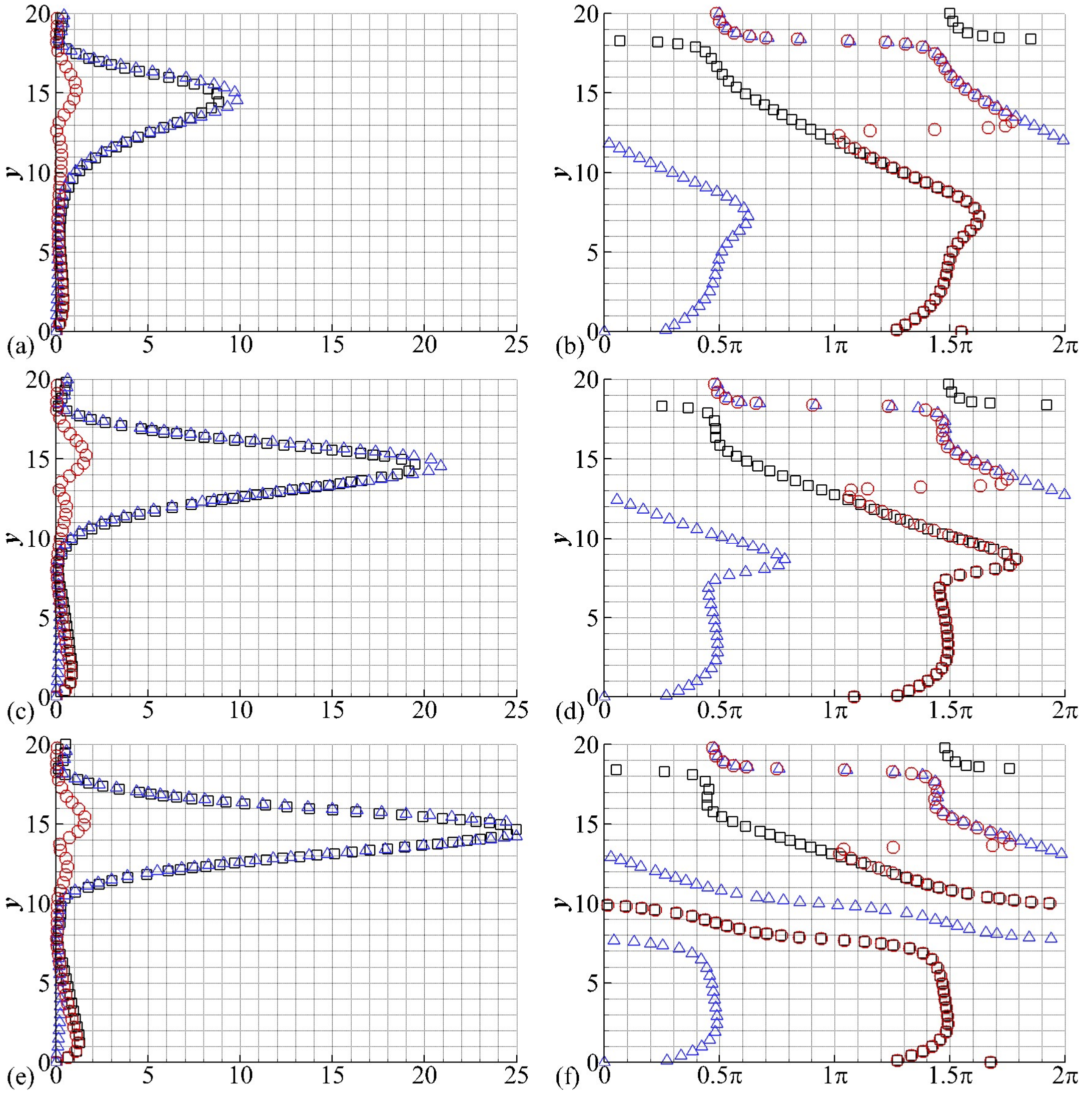

Figure 3.16 Magnitude (left-hand plots) and phase (right-hand plots) profiles of $-i\omega\frac{\hat{T}}{T}$ (□), $i\alpha U\frac{\hat{T}}{T}$ (△) and $(i\alpha U-i\omega)\frac{\hat{T}}{T}$ (○) under different ω: (a) (b) $\omega = 0.03$, $\alpha = 0.0348 - 0.0002i$; (c) (d) $\omega = 0.063$, $\alpha = 0.07068 - 0.00039i$; (e) (f) $\omega = 0.09$, $\alpha = 0.09913 - 0.00028i$.

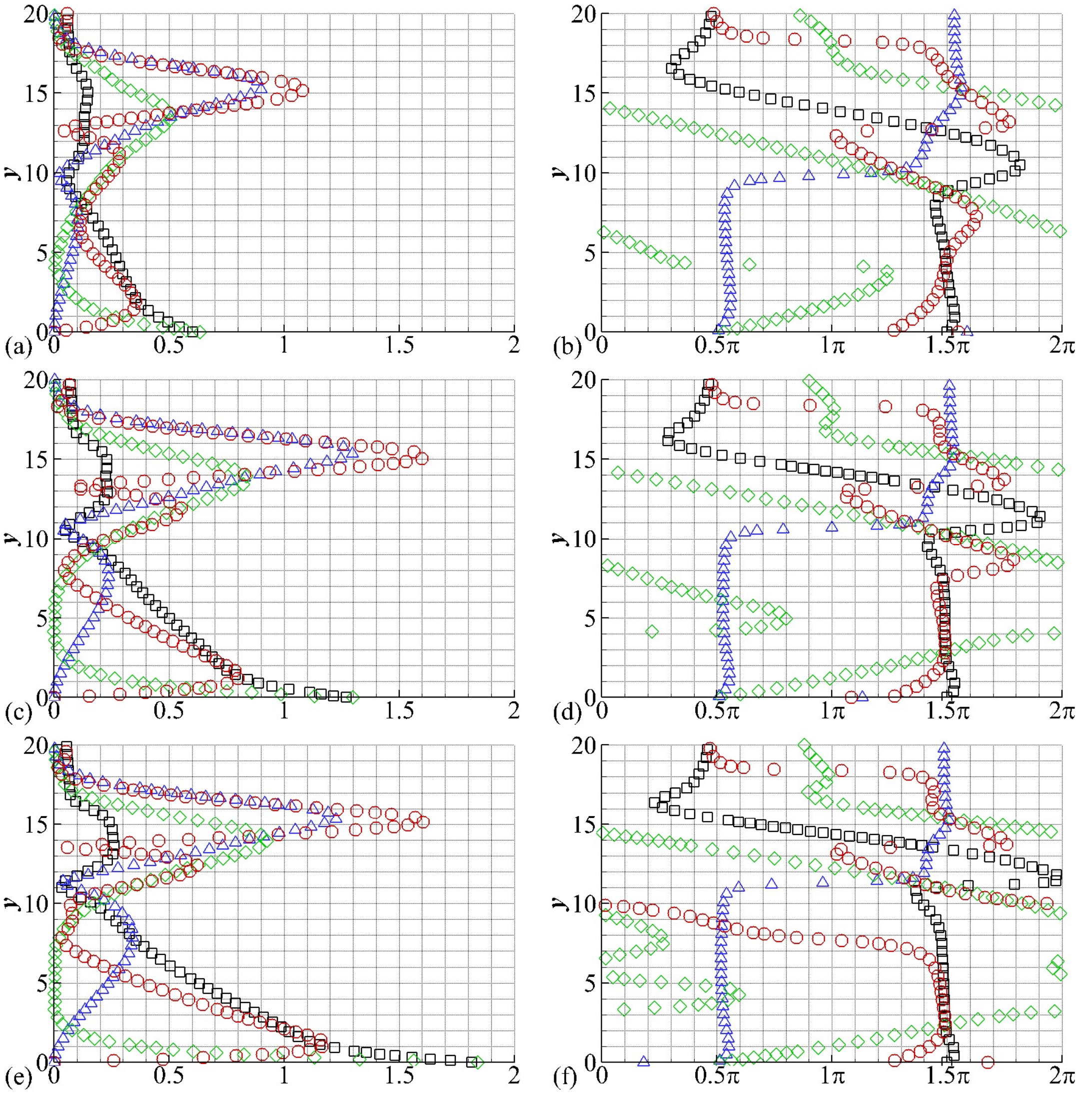

Figure 3.17 Magnitude (left-hand plots) and phase (right-hand plots) profiles of $-(\gamma-1)\left(i\alpha\hat{u}+\frac{\partial\hat{v}}{\partial y}\right)$ (□), $-\frac{dT}{dy}\frac{\hat{v}}{T}$ (△), $\frac{\gamma}{RPr}\frac{d^2}{dy^2}\left(\mu\hat{T}\right)$ (◇) and $(i\alpha U-i\omega)\frac{\hat{T}}{T}$ (○) under different ω: (a) (b) $\omega=0.03,\ \alpha=0.0348-0.0002i$; (c) (d) $\omega=0.063,\ \alpha=0.07068-0.00039i$; (e) (f) $\omega=0.09,\ \alpha=0.09913-0.00028i$.

A little below the critical layer, the phase of $-(\gamma-1)\left(i\alpha\hat{u}+\frac{\partial\hat{v}}{\partial y}\right)$ superposes on that of $(i\alpha U-i\omega)\frac{\hat{T}}{T}$ in a certain range along y coordinate, as shown in the right plots of Figure 3.17. Moreover, the width of the phase superposition is roughly proportional to the growth rate $-\alpha_i$. We conjecture this phase superposition is associated with the amplification of the first mode wave. According to Rayleigh's criterion, the excitation of the acoustic wave emerges as the time rate of change of heat adding synchronizes with that of the condensation. It is perfectly held by the phase overlap of $-(\gamma-1)\left(i\alpha\hat{u}+\frac{\partial\hat{v}}{\partial y}\right)$ and $(i\alpha U-i\omega)\frac{\hat{T}}{T}$ herein. Therefore, the phase overlap of $(\gamma-1)\left(i\alpha\hat{u}+\frac{\partial\hat{v}}{\partial y}\right)$ and $(i\alpha U-i\omega)\frac{\hat{T}}{T}$ in a wide region below the critical layer facilitates the local fluctuations.

Against the wall, the passively induced thermal conduction $\frac{\gamma}{RPr}\frac{d^2}{dy^2}\left(\mu\hat{T}\right)$ sustains the near-wall dilatation fluctuation, which is the same with the second mode instability.

3.6 Mechanisms of the Effects of Porous Walls on Unstable Modes

This section is to investigate the mechanism of the effect of porous walls on the first and second modes by performing phase analysis on the simplified linear stability equations. The mechanisms of the instabilities of the oblique first mode waves are also analyzed.

3.6.1 Stabilization and Destabilization of the Second Mode

According to the foregoing LST analyses, the stabilization effect of porous walls on the second mode is efficient when the admittance phase is close to π, and the destabilization effect of porous wall occurs as the admittance has a positive real part. Here the admittance of $A=-4$ and $A=4$ are utilized to investigate the mechanisms of the stabilization and destabilization of the second mode. The non-dimensional angular frequency $\omega=0.152$ is chosen. And the eigenvalues are $\alpha=$

$0.16406 - 0.004i$, $\alpha = 0.1646 - 0.00165i$, and $\alpha = 0.16251 - 0.01278i$ for the smooth solid wall $A = 0$, porous wall with $A = -4$, and porous wall with $A = 4$, respectively. The profiles of the magnitude and phase angle of the terms $-(\gamma - 1)\left(i\alpha\hat{u} + \frac{\partial\hat{v}}{\partial y}\right)$, $-\frac{dT}{dy}\frac{\hat{v}}{T}$, and $(i\alpha U - i\omega)\frac{\hat{T}}{T}$ in the porous-wall cases and the smooth-solid-wall case are demonstrated in Figure 3.18.

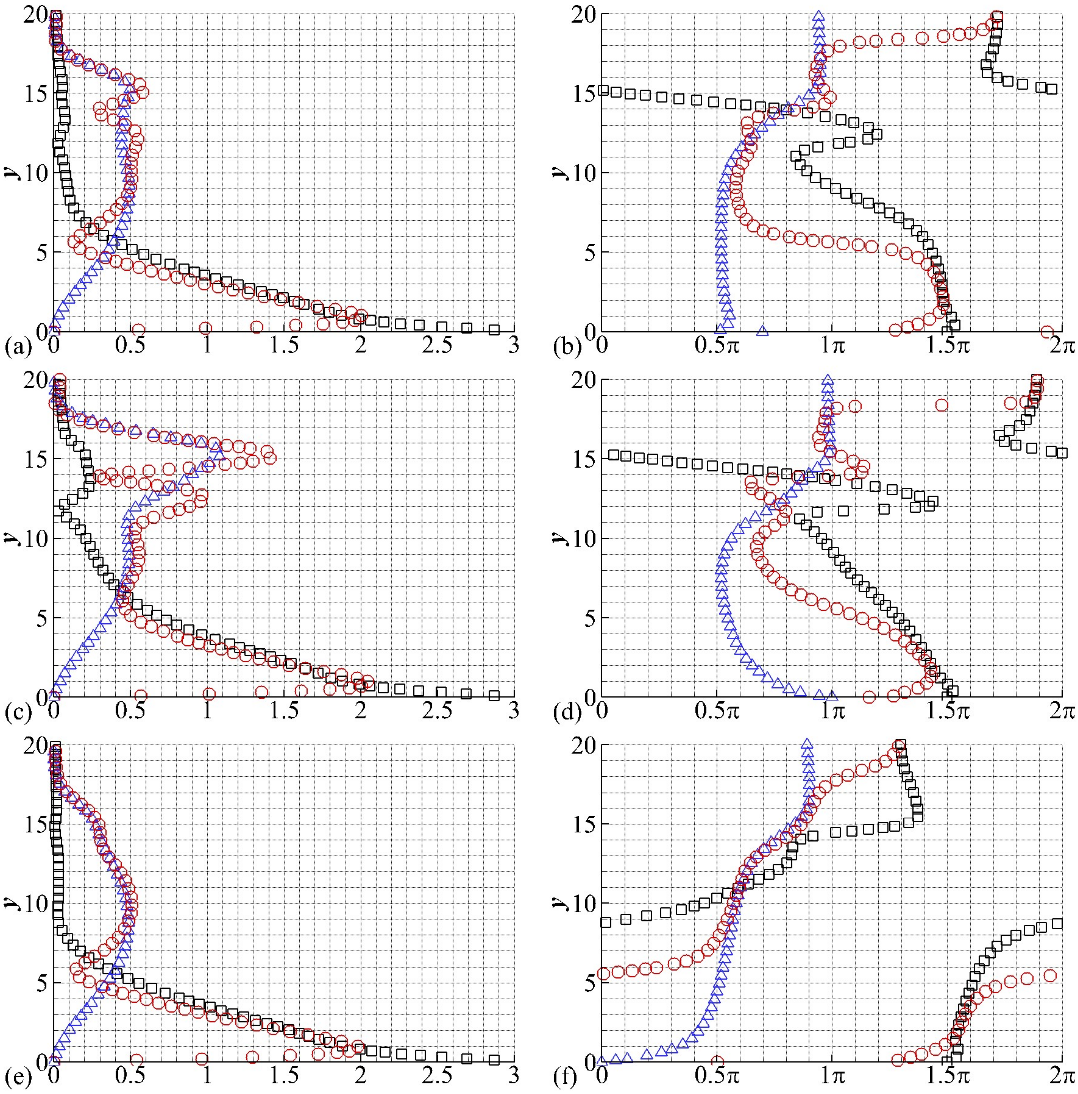

Figure 3.18 Magnitude (left-hand plots) and phase (right-hand plots) of $-(\gamma - 1)\left(i\alpha\hat{u} + \frac{\partial\hat{v}}{\partial y}\right)$(□), $-\frac{dT}{dy}\frac{\hat{v}}{T}$ (△), and $(i\alpha U - i\omega)\frac{\hat{T}}{T}$ (○) under different walls at $\omega = 0.152$: (a) (b) smooth solid wall, $\alpha = 0.16406 - 0.004i$; (c) (d) porous wall with $A =$

-4, $\alpha = 0.1646 - 0.00165i$; (e) (f) porous wall with $A = 4$, $\alpha = 0.16251 - 0.01278i$.

Firstly, we focus on the phase overlap between $-\frac{dT}{dy}\frac{\hat{v}}{T}$ and $(i\alpha U - i\omega)\frac{\hat{T}}{T}$ around the critical layer ($y \approx 14$). In the stabilized case ($A = -4$), the phase of $(i\alpha U - i\omega)\frac{\hat{T}}{T}$ crossing the critical layer shifts swiftly and it differs from the phase of $-\frac{dT}{dy}\frac{\hat{v}}{T}$ evidently. By contrast, in the destabilized case ($A = 4$), the phase of $(i\alpha U - i\omega)\frac{\hat{T}}{T}$ shifts moderately across the critical layer and is completely superposed on by the phase of $-\frac{dT}{dy}\frac{\hat{v}}{T}$. Recalling the growth rates of these three cases, we again find the critical-layer phase overlap of $-\frac{dT}{dy}\frac{\hat{v}}{T}$ and $(i\alpha U - i\omega)\frac{\hat{T}}{T}$ is positively correlated with the growth rate $-\alpha_i$, which confirms the amplification of the second mode depends upon the contribution of the thermal convection $-\frac{dT}{dy}\frac{\hat{v}}{T}$ to the local internal energy fluctuations.

Below the critical layer, the phase relation between $-\frac{dT}{dy}\frac{\hat{v}}{T}$ and $-(\gamma - 1)\left(i\alpha\hat{u} + \frac{\partial\hat{v}}{\partial y}\right)$ is significantly affected by the porous walls. In the baseline case, the phase of $-\frac{dT}{dy}\frac{\hat{v}}{T}$ is counter to that of $-(\gamma - 1)\left(i\alpha\hat{u} + \frac{\partial\hat{v}}{\partial y}\right)$ near the wall, as shown in Figure 3.18 (b), which means the upward flow and downward flow in the wall-normal direction correspond to the thermal expansion and contraction, respectively. For the disturbance defined by Equation (2.7) ($\phi = \psi(y)e^{i(\alpha x + \beta z - \omega t)}$), the change of phase with time increasing is from right to left (i.e., from 2π to 0) in the right plots of Figure 3.18. In the stabilized case, the phase of $-\frac{dT}{dy}\frac{\hat{v}}{T}$ shifts to the right at the wall, which indicates $\hat{v}$ is delayed by the porous wall. And this delay of $\hat{v}$ at the wall also causes a delay in the near-wall $\hat{v}$ due to the flow continuity. Thus $-\frac{dT}{dy}\frac{\hat{v}}{T}$ is no longer in phase with $(\gamma-1)\left(i\alpha\hat{u}+\frac{\partial\hat{v}}{\partial y}\right)$ near the wall, which attenuates the dilatation fluctuation. While in the destabilized case, the phase of $-\frac{dT}{dy}\frac{\hat{v}}{T}$ shifts to the left at the wall, which means the phase of $\hat{v}$ moves forward. It also affects the phase of $\hat{v}$ in the near-wall region. We can see from Figure 3.18 (f) that the $-\frac{dT}{dy}\frac{\hat{v}}{T}$ is completely in phase with $(\gamma-1)\left(i\alpha\hat{u}+\frac{\partial\hat{v}}{\partial y}\right)$ near the wall, then the interplay between the wall-normal energy transport and the dilatation fluctuation will reinforce each other.

As the disturbances around the critical layer interact with the near-wall perturbations mutually, the distortion in the near-wall perturbations results in the variation in the phase discrepancy between $-\frac{dT}{dy}\frac{\hat{v}}{T}$ and $(i\alpha U-i\omega)$ in the vicinity of the critical layer in the porous-wall cases.

3.6.2 Frequency Shift of the Second Mode

The LST results show the frequency band of the second mode instability shifts when the employed porous wall has an admittance phase close to 0.5π or 1.5π. Here we utilize the porous walls with the admittances of $A=4\exp(0.5\pi i)$ and $A=4\exp(1.5\pi i)$ to investigate the mechanisms of the frequency shift of the second mode. The non-dimensional angular frequency $\omega=0.152$ is chosen again. The eigenvalues for the smooth solid wall, the porous wall with $A=4\exp(0.5\pi i)$ and porous wall with $A=4\exp(1.5\pi i)$ are $\alpha=0.16406-0.00401i$, $\alpha=0.16689-0.002i$, and $\alpha=0.1621-0.00008i$, respectively. The profiles of the magnitude and phase of the terms $-(\gamma-1)\left(i\alpha\hat{u}+\frac{\partial\hat{v}}{\partial y}\right)$, $-\frac{dT}{dy}\frac{\hat{v}}{T}$ and $(i\alpha U-i\omega)\frac{\hat{T}}{T}$ for different walls are depicted in Figure 3.19.

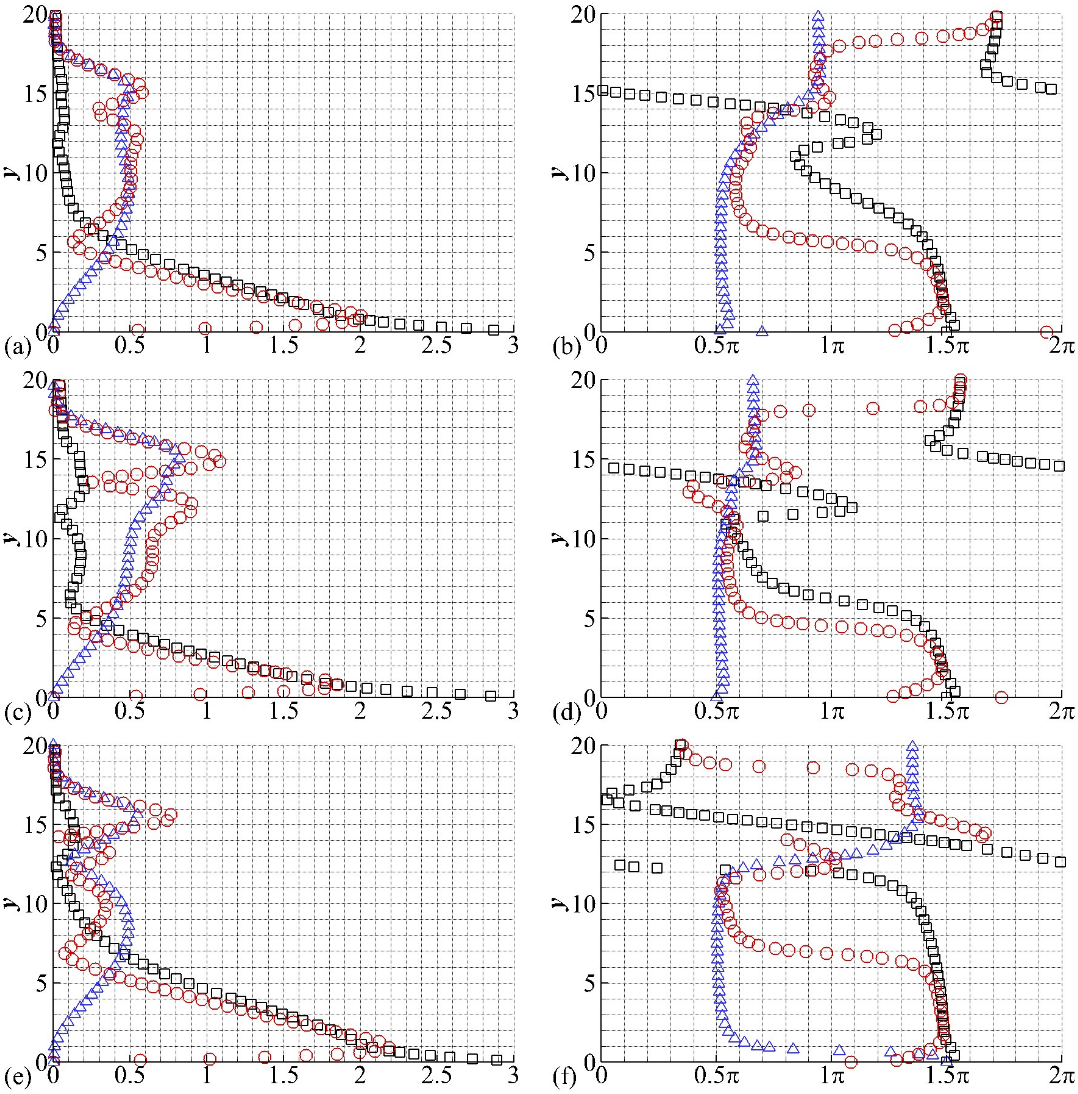

Figure 3.19 Magnitude (left-hand plots) and phase (right-hand plots) of $-(\gamma-1)\left(i\alpha\hat{u}+\frac{\partial\hat{v}}{\partial y}\right)$(□), $-\frac{dT}{dy}\frac{\hat{v}}{T}$ (△), and $(i\alpha U-i\omega)\frac{\hat{T}}{T}$ (○) of the smooth-solid-wall case and porous-wall cases at $\omega=0.152$: (a)(b) smooth solid wall, $\alpha=0.16406-0.00401i$, (c)(d) $A=4\exp(0.5\pi i)$, $\alpha=0.16689-0.002i$, (e)(f) $A=4\exp(1.5\pi i)$, $\alpha=0.1621-0.00008i$.

From the right plots of Figure 3.19, we can see that around the critical layer ($y\approx$

14), that the high phase overlap of $-\frac{dT}{dy}\frac{\hat{v}}{T}$ and $(i\alpha U - i\omega)\frac{\hat{T}}{T}$ corresponds to a large growth rate still holds herein. It can also be seen when the admittance phase $\theta = 0.5\pi$, the phase profiles of the terms $-(\gamma-1)\left(i\alpha\hat{u} + \frac{\partial\hat{v}}{\partial y}\right)$, $-\frac{dT}{dy}\frac{\hat{v}}{T}$ and $(i\alpha U - i\omega)\frac{\hat{T}}{T}$ approach those of the smooth-solid-wall case at large ω shown in Figure 3.15 (f). On the other hand, when $\theta = 1.5\pi$, the phase profiles of these three terms are similar to that of the smooth-solid-wall case at small ω shown in Figure 3.15(b). If we perform the analogy to a wide frequency spectrum, then the frequency shift is manifested.

The right-hand plots in Figure 3.19 show that the phase shift of $-\frac{dT}{dy}\frac{\hat{v}}{T}$ crossing the critical layer in the porous wall cases is plainly distinct from the baseline. Apparently, this phase shift accounts for the critical-layer phase discrepancy between $-\frac{dT}{dy}\frac{\hat{v}}{T}$ and $(i\alpha U - i\omega)\frac{\hat{T}}{T}$. Moveover, the phase shift of $-\frac{dT}{dy}\frac{\hat{v}}{T}$ crossing the critical layer is closely associated with the variation in the near-wall perturbations induced by porous walls.

Figure 3.20 compares the magnitude and phase profiles of the wall-normal fluctuating velocity $\hat{v}$ among these three cases. Pertaining to the porous wall with the admittance of $A = 4\,exp(0.5\pi i)$, the phase of $\hat{v}$ at the wall is identical to that near the wall and meanwhile the magnitude of $\hat{v}$ is non-zero at the wall, hence the porous wall facilitates the magnitude of $\hat{v}$ near the wall. Apparently, this outcome is also valid in a wide frequency band. Then the near-wall dilatation fluctuation which is associated with the wall-normal energy transport by $\hat{v}$ at small ω will be similar to that of the baseline case at large ω. Concomitantly, the spectral distribution of the growth rate is changed. While for the case $A = 4\,exp(1.5\pi i)$, the disturbance velocity

$\hat{v}$ at the wall with non-zero magnitude has a phase contrary to that against the wall, which leads to a decrease in the magnitude of $\hat{v}$ near the wall. Then a converse scenario emerges in a wide frequency band compared with the former case.

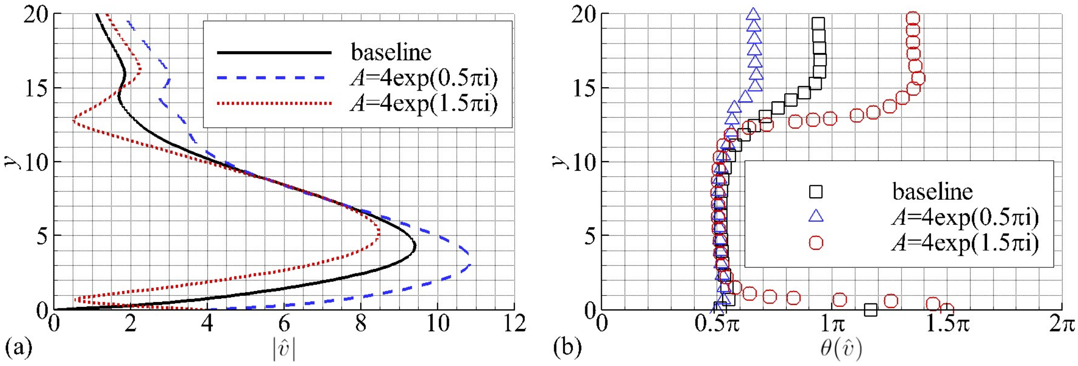

Figure 3.20 Magnitude (left-hand plots) and phase (right-hand plots) profiles of disturbance velocity $\hat{v}$ at $\omega = 0.152$ under different walls.

3.6.3 Stabilization and Destabilization of the First Mode

The stabilization and destabilization of the fist mode emerge when porous walls have admittance phases tending to 0.5π and π, respectively, according to the preceding calculations using LST. Here the porous walls with the admittance of $A = 4\exp(0.5\pi i)$ and $A = 4\exp(\pi i)$ are utilized to investigate the mechanisms of the stabilization and destabilization of the 2D first mode instabilities, respectively. The non-dimensional frequency $\omega = 0.063$ is chosen. The eigenvalues for the smooth solid wall, porous walls with the admittance of $= 4\exp(0.5\pi i)$ and admittance of $A = 4\exp(\pi i)$ are $\alpha = 0.07068 - 0.00039i$, $\alpha = 0.07025 - 0.00027i$ and $\alpha = 0.07062 - 0.00076i$, respectively. The magnitudes and phases of $(i\alpha U - i\omega)\frac{\hat{T}}{T}$,

$-\frac{dT}{dy}\frac{\hat{v}}{T}$ and $-(\gamma-1)\left(i\alpha\hat{u}+\frac{\partial\hat{v}}{\partial y}\right)$ of these three cases are illustrated in Figure 3.21.

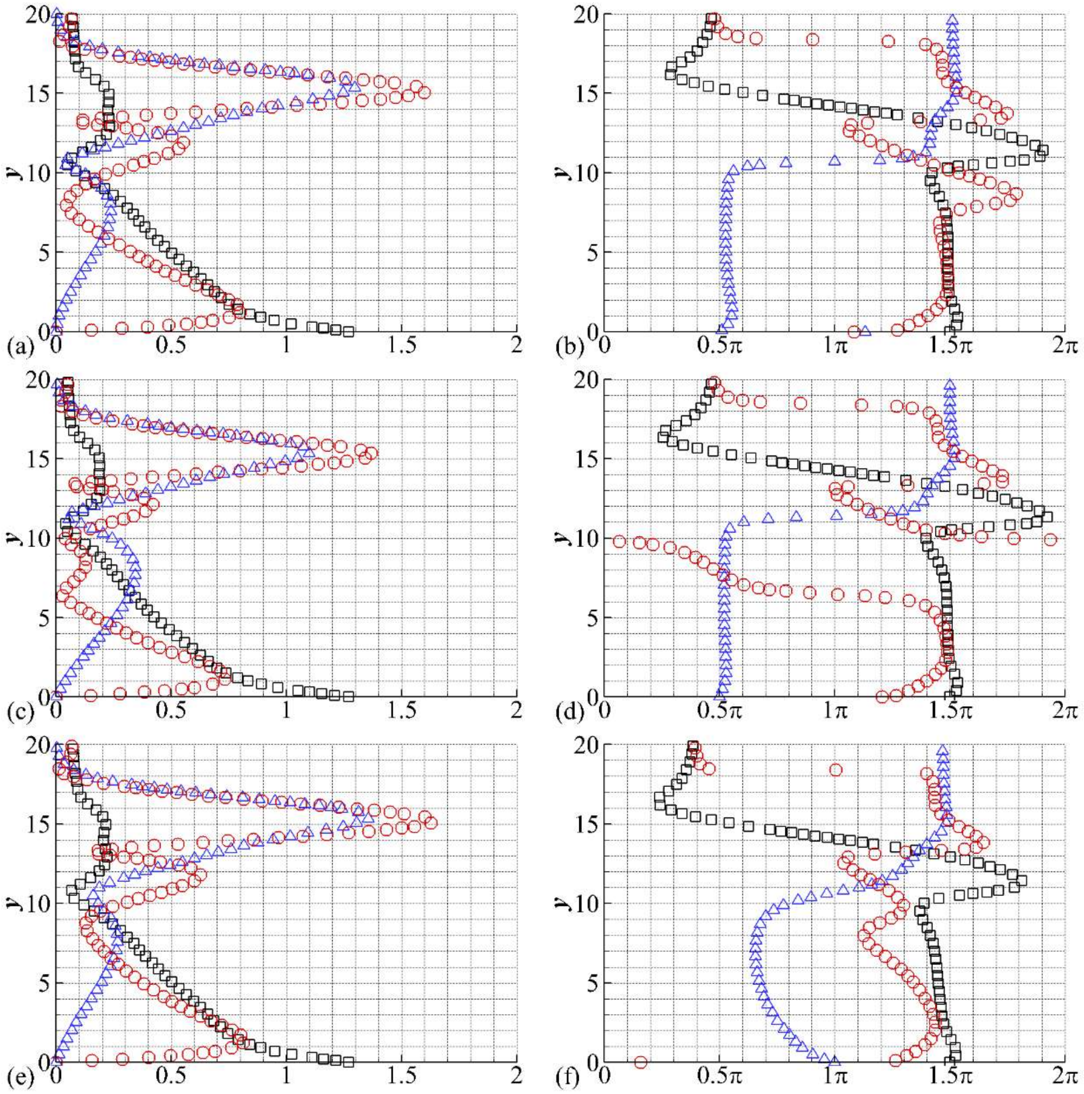

Figure 3.21 Magnitude (left-hand plots) and phase (right-hand plots) profiles of $-(\gamma-1)\left(i\alpha\hat{u}+\frac{\partial\hat{v}}{\partial y}\right)$(□), $-\frac{dT}{dy}\frac{\hat{v}}{T}$ (△), and $(i\alpha U-i\omega)\frac{\hat{T}}{T}$ (○) in the smooth-solid-wall case and porous-wall cases at $\omega=0.063$: (a) (b) the smooth solid wall, $\alpha=0.07068-0.00039i$(c) (d) the porous wall with $A=4\exp(0.5\pi i)$, $\alpha=0.07025-0.00027i$, (e) (f) the porous wall with $A=4\exp(\pi i)$, $\alpha=0.07062-0.00076i$.

With respect to the case $A=4\exp(0.5\pi i)$, the phase discrepancy between

$-\frac{dT}{dy}\frac{\hat{v}}{T}$ and $(i\alpha U - i\omega)\frac{\hat{T}}{T}$ around the critical layer ($y \approx 13$) is analogous to that of the smooth-solid-wall case due to the small growth rate. While below the critical layer, the phase superposition of $-(\gamma - 1)\left(i\alpha\hat{u} + \frac{\partial\hat{v}}{\partial y}\right)$ and $(i\alpha U - i\omega)\frac{\hat{T}}{T}$ shrinks in y coordinate compared with the smooth-solid-wall case, as shown in Figure 3.21(b) and (d). Identical to Figure 3.17 (b), (d), and (f), the diminution of this phase superposition corresponds to a decrease in the growth rate. Therefore, it could be concluded that the amplification of the first mode in the current boundary layer depends upon the mutual interaction between the local dilatation fluctuations and internal energy fluctuations.

When the porous wall with the admittance of $A = 4\exp(\pi i)$ is employed, the phase of $-\frac{dT}{dy}\frac{\hat{v}}{T}$ is recast near the wall, as shown in Figure 3.21 (f). It is also demonstrated that the phase discrepancy between $-\frac{dT}{dy}\frac{\hat{v}}{T}$ and $(i\alpha U - i\omega)\frac{\hat{T}}{T}$ in the vicinity of the critical layer is diminished in contrast to the baseline. In other words, the contribution of thermal convection $-\frac{dT}{dy}\frac{\hat{v}}{T}$ to internal energy fluctuations is promoted. Therefore, the increase of the growth rate emerging in the case of the admittance phase close to π is associated with the energy transport by the wall-normal velocity fluctuation around the critical layer.

3.6.4 Oblique First-Mode Wave

The LST results show that the oblique first-mode wave is more unstable than the 2D first-mode wave, which is not converted by porous walls. Here the non-dimensional angular frequency $\omega = 0.063$ is adopted again to compare the oblique-wave case with the 2D-wave case in the interplay of $-(\gamma-1)\left(i\alpha\hat{u}+\frac{\partial\hat{v}}{\partial y}+i\beta\hat{w}\right)$, $-\frac{dT}{dy}\frac{\hat{v}}{T}$, and $(i\alpha U-i\omega)\frac{\hat{T}}{T}$ to investigate the mechanisms of the growth of the oblique first-mode instability. The propagation angle of the oblique wave $\arctan\left(\frac{\beta}{\alpha_r}\right)=45^{\circ}$ is chosen herein. The eigenvalues of the oblique wave and 2D wave are $\alpha = 0.07123-0.00103i$ and $\alpha=0.07068-0.00039i$, respectively. The magnitude and phase profiles of $-(\gamma-1)\left(i\alpha\hat{u}+\frac{\partial\hat{v}}{\partial y}+i\beta\hat{w}\right)$, $-\frac{dT}{dy}\frac{\hat{v}}{T}$ and $(i\alpha U-i\omega)\frac{\hat{T}}{T}$ of the two cases are illustrated in Figure 3.22.

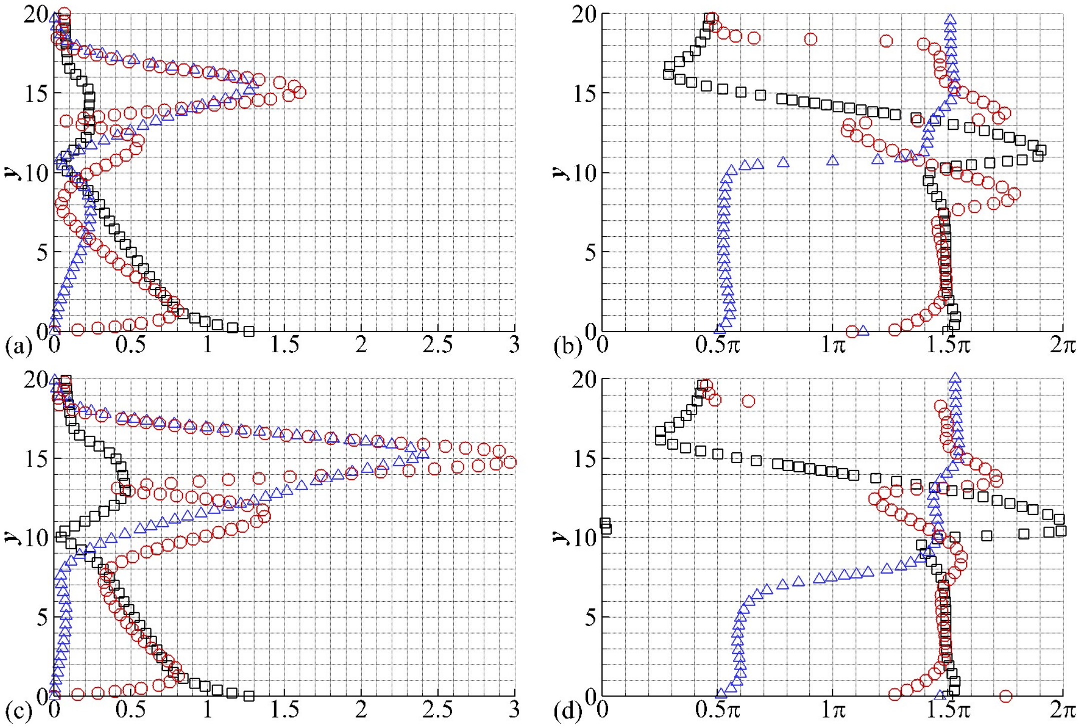

Figure 3.22 Magnitude (left-hand plots) and phase (right-hand plots) profiles of $-(\gamma-1)\left(i\alpha\hat{u}+\frac{\partial\hat{v}}{\partial y}+i\beta\hat{w}\right)$(□), $-\frac{dT}{dy}\frac{\hat{v}}{T}$ (△), and $(i\alpha U-i\omega)\frac{\hat{T}}{T}$ (○) in the 2D-wave and oblique-wave cases at $\omega=0.063$: (a) (b) 2D wave, $\alpha=0.07068-0.00039i$ (c) (d) oblique wave with propagation angle of $\arctan\left(\frac{\beta}{\alpha_r}\right)=45^{\circ}$, $\alpha=0.07123-0.00103i$.

It is evident that around the critical layer the peak magnitude of $-\frac{dT}{dy}\frac{\hat{v}}{T}$ in the oblique-wave case is much larger than that in the 2D-wave case, as shown in Figure 3.22(a) and (c). By comparing Figure 3.22(b) and (d), it can be observed that in the vicinity of the critical layer, the phase discrepancy between $-\frac{dT}{dy}\frac{\hat{v}}{T}$ and $(i\alpha U - i\omega)\frac{\hat{T}}{T}$ of the oblique-wave case is relatively smaller than that of the 2D-wave case, meaning more contribution to the local internal energy fluctuations is provided by the thermal convection $-\frac{dT}{dy}\frac{\hat{v}}{T}$. On the other hand, the phase superposition of $(i\alpha U - i\omega)\frac{\hat{T}}{T}$ and $-(\gamma-1)\left(i\alpha\hat{u} + \frac{\partial\hat{v}}{\partial y} + i\beta\hat{w}\right)$ below the critical layer is wider in the oblique-wave case than the 2D-wave case, as shown in Figure 3.22(b) and (d). It reveals the mutual interactions between the internal energy fluctuation and dilatation fluctuation are promoted in the oblique-wave case.

Consequently, the large growth rate in the oblique-wave case may be associated with the phase discrepancy between $-\frac{dT}{dy}\frac{\hat{v}}{T}$ and $(i\alpha U - i\omega)\frac{\hat{T}}{T}$ in the vicinity of the critical layer and phase overlap between $(i\alpha U - i\omega)\frac{\hat{T}}{T}$ and $-(\gamma-1)\left(i\alpha\hat{u} + \frac{\partial\hat{v}}{\partial y} + i\beta\hat{w}\right)$ near the wall.

3.7 Summary

The effects of porous walls on the first and second modes depend on the admittance phase of porous walls and these effects are facilitated by the increase in the admittance magnitude. The first mode instability is stabilized when the admittance phase tends to 0.5π and destabilized when the admittance phase is close to π. On the contrary, the second mode is damped as the admittance phase approaches to π. If the admittance phase tends to 0.5π or 1.5π, the second mode is destabilized with a shift to the low- or high-frequency band, respectively. In terms of the oblique waves, the effects of porous walls are independent of the wave propagation angle.

The mechanisms of the amplification of the second mode are associated with the relative phases of the energy transport by the wall-normal velocity fluctuation and the total time rate of the fluctuating internal energy around the critical layer. A high phase overlap corresponds to a large growth rate. Porous walls generate an impact on the wall-normal fluctuating velocity at the wall, which results in a recasting in the phase of the wall-normal fluctuating velocity. The frequency shift is associated with the change in the magnitude of the wall-normal fluctuating velocity near the wall.

The amplification of the first mode may be associated with the manual interaction between the internal energy fluctuation and the dilatation fluctuation near the wall. In the porous-wall case with the admittance phase close to π and the oblique wave case, the amplification of the first mode is also affected by the diminishment in the phase discrepancy between the energy transport by the wall-normal velocity fluctuation and the total time rate of the fluctuating internal energy in the vicinity of the critical layer.

Chapter 4 Numerical Studies on the Effects of Porous Walls on Hypersonic Boundary Layers Instabilities

In this chapter, direct numerical simulations (DNS) are performed to validate the effects of porous walls on the hypersonic boundary-layer instability obtained from LST. Based on the DNS computations, the mechanisms of the stabilization, destabilization, and the frequency shift of the second mode are further studied. The numerical simulations are performed on a 2D boundary-layer flow over a flat plate and disturbances are artificially generated by a blowing-suction actuator. The porous walls employed in this chapter are characterized using their admittance, which is equivalent to real structures [38].

4.1 Validation of Numerical Method

In the DNS computations, the flow conditions are: free stream Mach number $M_\infty = 6$, unit Reynolds number $Re_1^* = 10.5 \times 10^6 \mathrm{m}^{-1}$, free stream temperature $T_\infty^* = 43.18\mathrm{K}$, special heat ratio $\gamma = 1.4$, and Prandtl number $Pr = 0.72$. Here asterisks denote dimensional quantities. The viscosity is calculated using Sutherland's law and the reference temperature is $273.15\mathrm{K}$. The wall is isothermal with a temperature of $T_w^* = 293\mathrm{K}$. These parameters are obtained from the experiments conducted by Bountin et al. [23].

The length of the flat plate is 0.2m. The computations are carried out in a grid with 1607×200 nodes, and there are more than 60 nodes within the boundary layer at $x^* = 0.1\mathrm{m}$, where x^* denotes the distance from the leading edge in the streamwise direction.

4.1.1 Steady Flow

The velocity and temperature profiles obtained from the DNS method at $x^* = 0.2\mathrm{m}$ are depicted in Figure 4.1 with the corresponding profiles obtained from a self-similar solution provided for comparison. It can be seen that the DNS results agree well with the theoretical results.

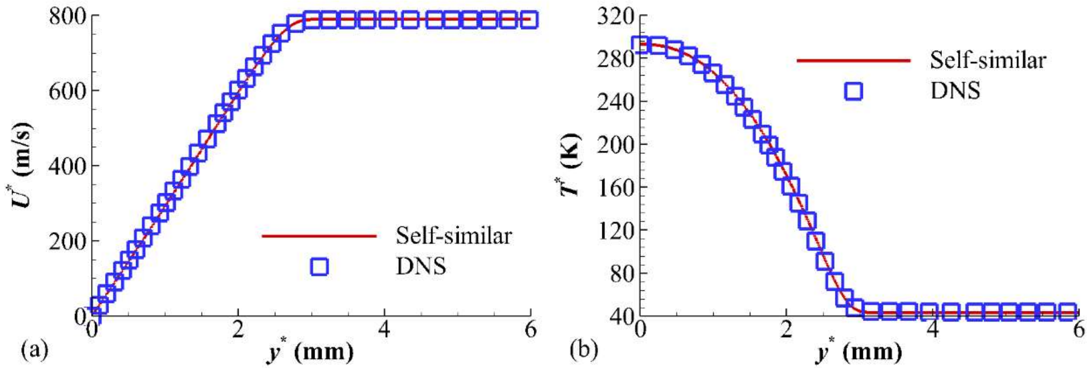

Figure 4.1 Profiles of (a) velocity and (b) temperature at $x^* = 0.2\mathrm{m}$.

4.1.2 Unsteady Flow

In the unsteady flow computations, disturbances are induced by a blowing-suction actuator defined by Equation (2.20) with the parameters of $x_1^* = 0.01\mathrm{m}$, $x_2^* = 0.015\mathrm{m}$, $\varepsilon = 0.001$. The disturbance frequency is $f^* = 138.74\mathrm{kHz}$. In the following analyses, the non-dimensional velocity, density, temperature, and other variables are scaled by their corresponding free-stream values, pressure by $\rho_\infty U_\infty^2$ and all lengths by the boundary layer scale $l^* = \sqrt{x^*/Re_1}$.

The amplitude distribution of the wall pressure fluctuations is shown in Figure 4.2. It has a good agreement with the calculations conducted by Zhao et al. [21] and Hao and Wen [70]. The growth rate and phase speed based are also resolved using Equations (2.22) and (2.23) based on the wall pressure perturbations. Figure 4.3 shows that the growth rate and phase speed obtained from DNS results conform to the slow mode in the region roughly from $x^* = 0.08\mathrm{m}$ to $x^* = 0.15\mathrm{m}$, despite a little discrepancy emerges in the phase speed, which will be interpreted in the next section. Furthermore, the profiles of the perturbation components in this region also follow the predictions of LST. For instance, Figure 4.4 shows the profiles of disturbance components obtained from DNS results at $x^* = 0.11\mathrm{m}$ have high consistency between the DNS results and LST results. Therefore, the evolution of the fluctuations in this region is dominated by the slow mode. Hereafter, we call this region a linear growth region.

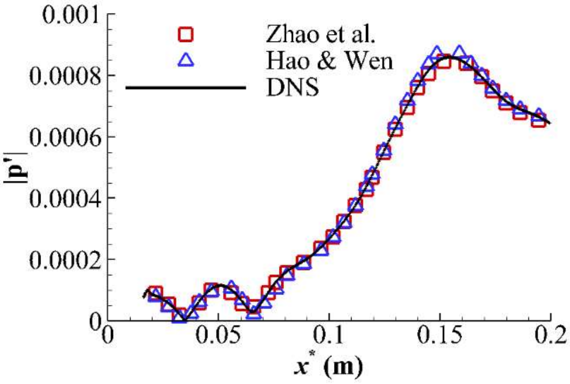

Figure 4.2 Comparison of the amplitude of the wall pressure fluctuation calculated from DNS results with the calculations conducted by Zhao et al. [21] and Hao & Wen [70].

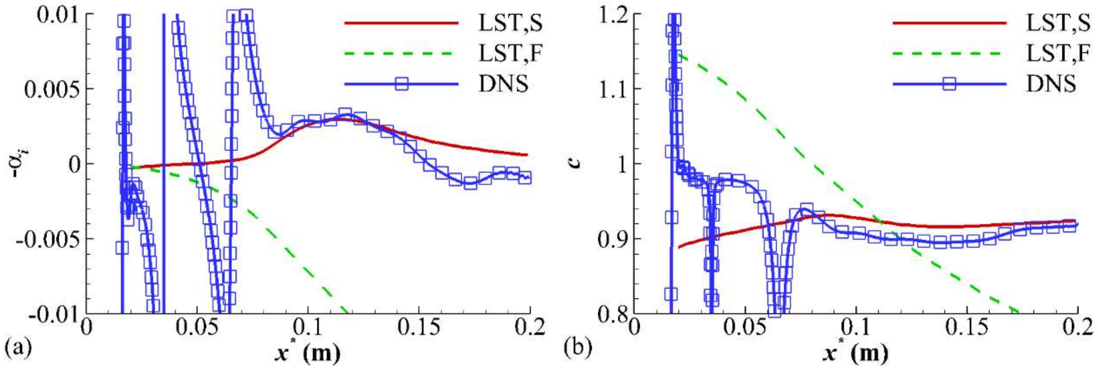

Figure 4.3 Comparison of (a) growth rate and (b) phase speed of perturbations obtained from DNS and LST. S and F denote the slow and fast modes, respectively.

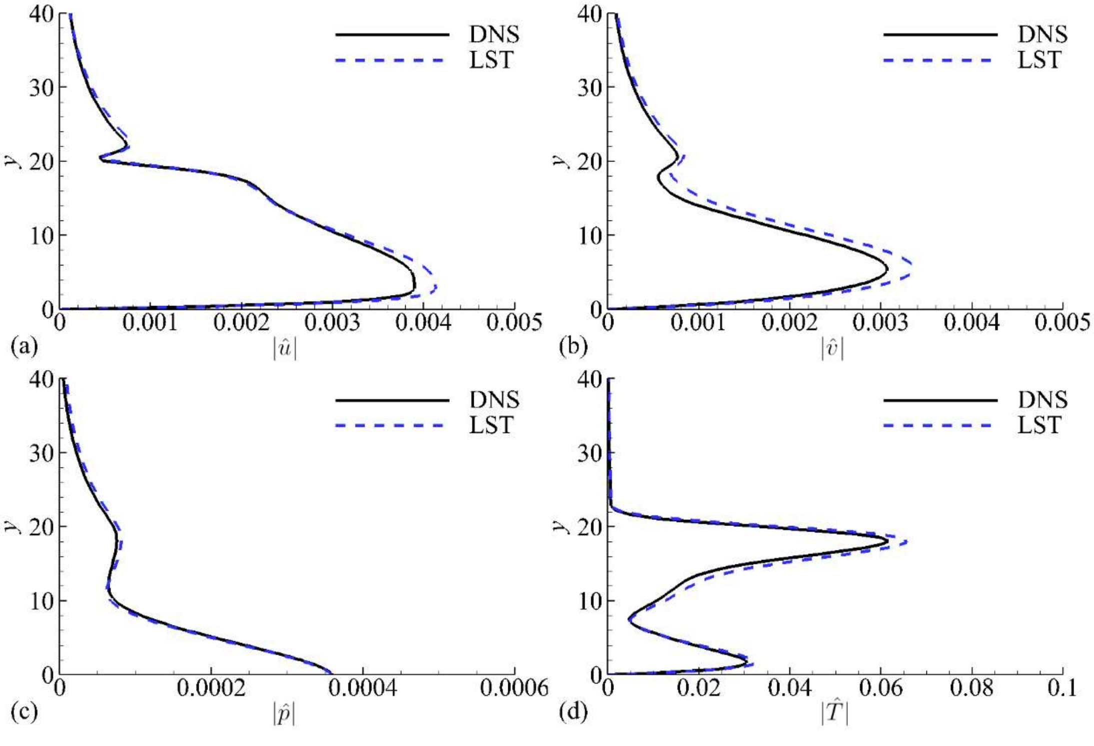

Figure 4.4 Comparison of the profiles of perturbation components at $x^* = 0.11\mathrm{m}$. The LST results are scaled by the magnitude of the wall pressure perturbation from DNS.

In the current boundary-layer flow, the first mode (i.e., the unstable, slow mode near the leading edge) has a considerably small growth rate, which marginally amplifies instability waves. Meanwhile, the fast mode swiftly damps the upstream perturbations. The contrary effects of the fast and slow modes on the local disturbances result in oscillations in the growth rate and phase speed at small x^*, as shown in Figure 4.3 (a) and (b). Therefore, we cannot perform the studies of the effects of porous walls on the first mode on the current boundary-layer flow. It may be appropriate to numerically study the first mode instabilities on a 3D boundary layer flow because oblique first-mode waves are more unstable than the 2D first-mode waves. In the current simulations, 3D instabilities are not involved.

4.2 Evolution of the Second-Mode Instabilities

Proceeding on the above unsteady flow, we analyze the evolution of the second mode instabilities within the boundary layer over a smooth solid wall, and this investigation is the baseline for the following analyses on the stabilization, destabilization, and frequency shift of the second mode with porous walls applied.

The contours illustrated in Figure 4.5 show that the fluctuations concentrate in two regions: one is around the critical layer ($U = c$) and the other is below the sonic line ($U = c - a$). In the former region, the temperature and density fluctuations are considerably strong. Moreover, the density fluctuations illustrated in Figure 4.5 (e) have a “rope-like” appearance, which is consistent with the schlieren images from experimental studies [33, 71-73]. In the latter region, the velocities and pressure fluctuations are remarkable, while the perturbations in density are considerably weak, as shown in Figure 4.5 (a) (b) and (c).

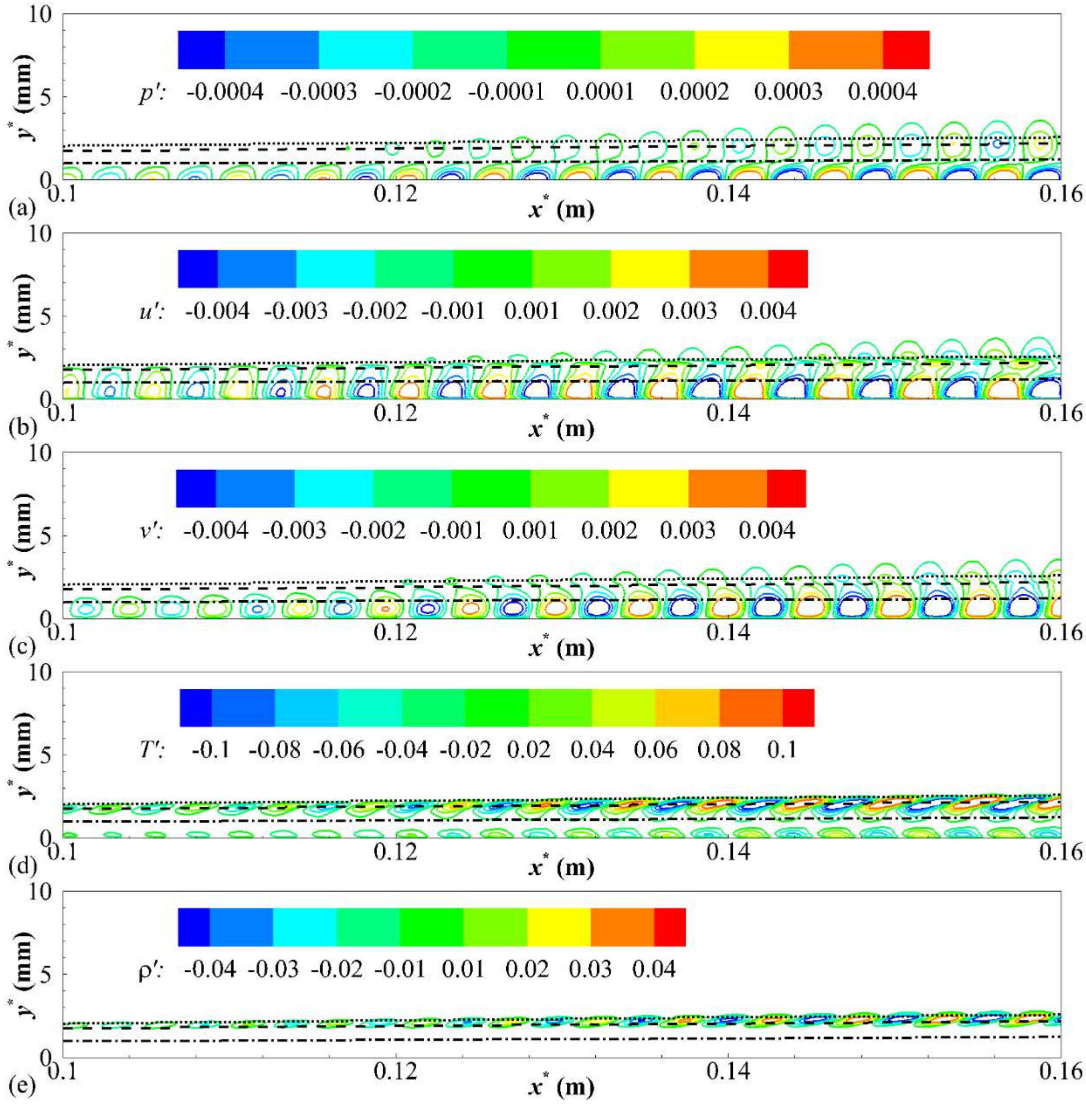

Figure 4.5 Contours of the instantaneous disturbance components in the smooth-solid-wall case. Boundary layer edge ($U = 0.99U_e$) (······), critical layer ($U = c$) (- - -) and sonic line ($U = c - a$) (—·—·).

In Chapter 3, phase analysis was employed on the simplified disturbance energy equation. Here the same execution is implemented to analyze the energy exchange in the evolution of the second mode waves. Unlike the waveform defined by Equation (2.7), here the disturbance vector is in the form of $q'(x, y, t) = \hat{q}(x, y)e^{-i\omega t}$, which takes the nonparallel effect into account. As only the 2D waves are concerned in this chapter, the simplified linear stability equations provided in Chapter 3 can be rewritten as:

$$\frac{1}{T}\left(-i\omega\hat{u}+U\frac{\partial\hat{u}}{\partial x}\right)=-\frac{dU}{dy}\frac{\hat{v}}{T}-\frac{\partial\hat{p}}{\partial x}+\frac{1}{R}\frac{d}{dy}\left(\mu\frac{\partial\hat{u}}{\partial y}+\frac{dU}{dy}\frac{d\mu}{dT}\hat{T}\right) \quad (4.1)$$

$$\frac{1}{T}\left(-i\omega\hat{v}+U\frac{\partial\hat{v}}{\partial x}\right)=-\frac{\partial\hat{p}}{\partial y}+\frac{4}{3R}\frac{\partial}{\partial y}\left(\mu\frac{\partial\hat{v}}{\partial y}\right) \quad (4.2)$$

$$\frac{1}{T}\left(-i\omega\hat{T}+U\frac{\partial\hat{T}}{\partial x}\right)=-\frac{dT}{dy}\frac{\hat{v}}{T}-(\gamma-1)\left(\frac{\partial\hat{u}}{\partial x}+\frac{\partial\hat{v}}{\partial y}\right)+\frac{\gamma}{RPr}\frac{\partial^2}{\partial y^2}(\mu\hat{T}) \quad (4.3)$$

Here we apply the perturbation quantities obtained from DNS computations into the disturbance energy equation (4.3) to investigate the interactions among $\frac{1}{T}\left(-i\omega\hat{T}+U\frac{\partial\hat{T}}{\partial x}\right), -\frac{dT}{dy}\frac{\hat{v}}{T}$ and $-(\gamma-1)\left(\frac{\partial\hat{u}}{\partial x}+\frac{\partial\hat{v}}{\partial y}\right)$ during the wave propagation. The magnitudes of $\frac{1}{T}\left(-i\omega\hat{T}+U\frac{\partial\hat{T}}{\partial x}\right)$, $-\frac{dT}{dy}\frac{\hat{v}}{T}$ and $-(\gamma-1)\left(\frac{\partial\hat{u}}{\partial x}+\frac{\partial\hat{v}}{\partial y}\right)$ in the linear growth region are illustrated in Figure 4.6 and the phase angles of the corresponding terms are provided in Figure 4.7. The non-dimensional boundary layer thickness is about 21, and the critical layer and sonic line obtained from LST are at $y\approx 17$ and $y\approx 10$, respectively. In the linear growth region, the phase speed of the second-mode waves obtained from LST varies mildly, as illustrated in Figure 4.3 (b), which leads to basically constant locations of the critical layer and the sonic line in the dimensionless view.

Figure 4.6 shows that $\frac{1}{T}\left(-i\omega\hat{T}+U\frac{\partial\hat{T}}{\partial x}\right)$ is nearly stagnant at $y\approx 17$ and $y\approx 7$, where a phase shift emerges as shown in Figure 4.7, in the evolution of instability waves. We know the former stagnant point corresponds to the critical layer at which the time rate of change of internal energy $-i\omega\frac{\hat{T}}{T}$ is accounted for by the mean flow advection of perturbed thermal energy $\frac{U}{T}\frac{\partial\hat{T}}{\partial x}$. The latter stagnant point is due to the counteraction between the wall-normal energy transport $-\frac{dT}{dy}\frac{\hat{v}}{T}$ and energy change caused by dilatation fluctuations $-(\gamma-1)\left(\frac{\partial\hat{u}}{\partial x}+\frac{\partial\hat{v}}{\partial y}\right)$. In the vicinity of the critical layer, the term $-\frac{dT}{dy}\frac{\hat{v}}{T}$ is comparable to $\frac{1}{T}\left(-i\omega\hat{T}+U\frac{\partial\hat{T}}{\partial x}\right)$ in magnitude. While below the near-wall stagnant point, the magnitude of $-(\gamma-1)\left(\frac{\partial\hat{u}}{\partial x}+\frac{\partial\hat{v}}{\partial y}\right)$ grows greatly compared with the term $-\frac{dT}{dy}\frac{\hat{v}}{T}$.

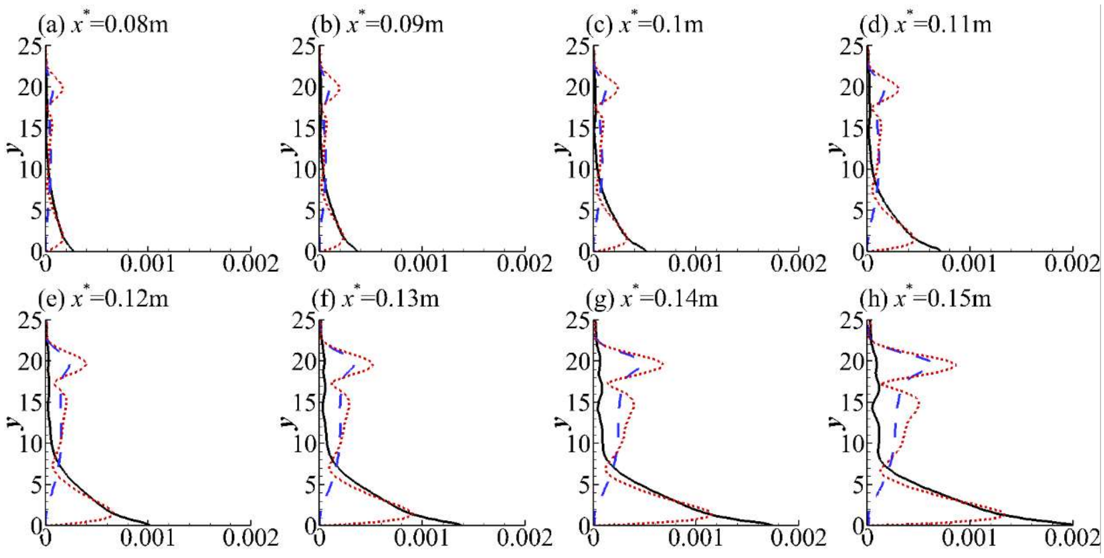

Figure 4.6 Profiles of the magnitudes of $\frac{1}{T}\left(-i\omega\hat{T}+U\frac{\partial\hat{T}}{\partial x}\right)$ (……), $-\frac{dT}{dy}\frac{\hat{v}}{T}$ (- - -), and $-(\gamma-1)\left(\frac{\partial\hat{u}}{\partial x}+\frac{\partial\hat{v}}{\partial y}\right)$ (——) at different locations.

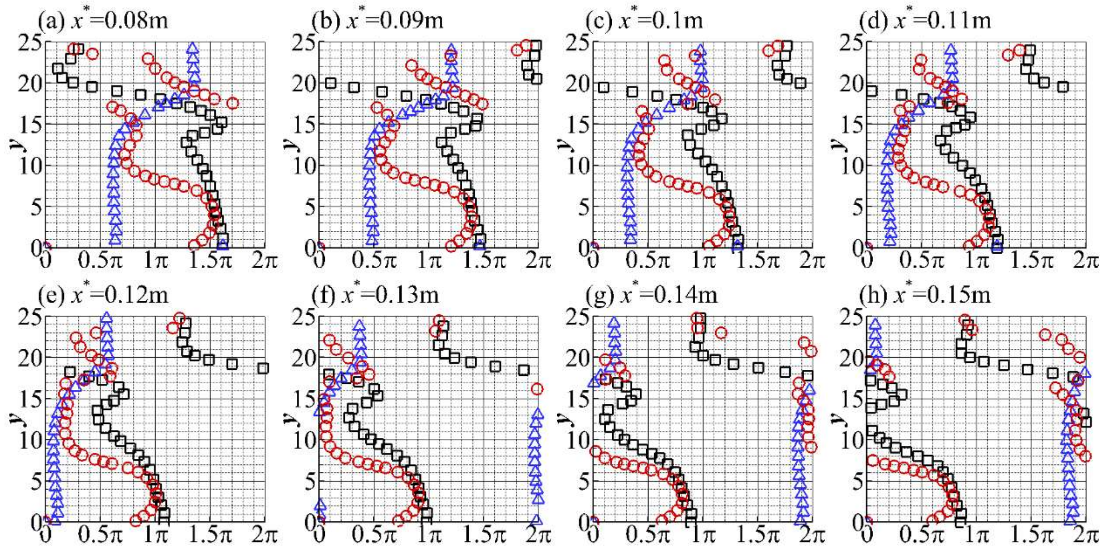

Figure 4.7 Profiles of the phase angles of $\frac{1}{T}\left(-i\omega\hat{T}+U\frac{\partial\hat{T}}{\partial x}\right)$(○), $-\frac{dT}{dy}\frac{\hat{v}}{T}$ (△) and

$-(\gamma-1)\left(\frac{\partial\hat{u}}{\partial x}+\frac{\partial\hat{v}}{\partial y}\right)$ (□) at different locations.

Figure 4.7 demonstrates that in the vicinity of the critical layer the phases of $\frac{1}{T}\left(-i\omega\hat{T}+U\frac{\partial\hat{T}}{\partial x}\right)$ and $-\frac{dT}{dy}\frac{\hat{v}}{T}$ gradually overlap with each other along with the increase of x^* and then diverge as x^* continuously increases. Combined with Figure 4.3(a), it is clear that the high phase overlap is in accord with the large growth rate, which is identical to the conclusion obtained in Chapter 3.

The phase overlap of $\frac{1}{T}\left(-i\omega\hat{T}+U\frac{\partial\hat{T}}{\partial x}\right)$ and $-\frac{dT}{dy}\frac{\hat{v}}{T}$ is associated with their phase variations across the critical layer. Figure 4.8 illustrates the distributions of the maximum phase differences of $\frac{1}{T}\left(-i\omega\hat{T}+U\frac{\partial\hat{T}}{\partial x}\right)$ and $-\frac{dT}{dy}\frac{\hat{v}}{T}$ across the critical layer, respectively denoted by $\Delta\theta_{max}\left(\frac{1}{T}\left(-i\omega\hat{T}+U\frac{\partial\hat{T}}{\partial x}\right)\right)$ and $\Delta\theta_{max}\left(-\frac{dT}{dy}\frac{\hat{v}}{T}\right)$, in comparison with the distribution of the growth rate. It can be seen that $\Delta\theta_{max}\left(\frac{1}{T}\left(-i\omega\hat{T}+U\frac{\partial\hat{T}}{\partial x}\right)\right)$ decreases swiftly at small x^* and then maintains at about 0.5π, while $\Delta\theta_{max}\left(-\frac{dT}{dy}\frac{\hat{v}}{T}\right)$ shrinks continuously as x^* increases. When the maximum phase variations of $\frac{1}{T}\left(-i\omega\hat{T}+U\frac{\partial\hat{T}}{\partial x}\right)$ and $-\frac{dT}{dy}\frac{\hat{v}}{T}$ are nearly identical, the growth rate reaches its peaks.

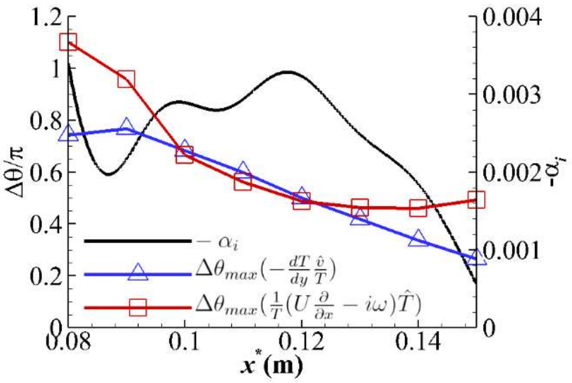

Figure 4.8 Distributions of maximum phase variation (left y axis) of $-\frac{dT}{dy}\frac{\hat{v}}{T}$ and $\frac{1}{T}\left(-i\omega\hat{T}+U\frac{\partial\hat{T}}{\partial x}\right)$ crossing the critical layer and growth rate (right y axis).

The distribution of $\Delta\theta_{max}\left(-\frac{dT}{dy}\frac{\hat{v}}{T}\right)$ indicates the wave propagation speed is different on the two sides of the critical layer. Recalling Figure 4.3 (b), the phase speed of wall-pressure perturbations is about 0.9 in the linear growth region. According to the development of the phase of $-\frac{dT}{dy}\frac{\hat{v}}{T}$ at the boundary edge depicted in Figure 4.7, the phase speed of the disturbance propagation around the critical layer is about 0.92, which is equal to the prediction of LST shown in Figure 4.3 (b). Therefore, the propagation speed near the wall is slower than that in the region away from the wall, which results in a diminishing of $\Delta\theta_{max}\left(-\frac{dT}{dy}\frac{\hat{v}}{T}\right)$.

The evolution of $\Delta\theta_{max}\left(\frac{1}{T}\left(-i\omega\hat{T}+U\frac{\partial\hat{T}}{\partial x}\right)\right)$ is inevitably affected by the phase variation of $-\frac{dT}{dy}\frac{\hat{v}}{T}$. Meanwhile, the thermal conduction $\frac{\gamma}{RPr}\frac{\partial^2}{\partial y^2}\left(\mu\hat{T}\right)$ also plays a role in the evolution of $\Delta\theta_{max}\left(\frac{1}{T}\left(-i\omega\hat{T}+U\frac{\partial\hat{T}}{\partial x}\right)\right)$. At the beginning of the evolution of internal energy perturbations, the effects of $-\frac{dT}{dy}\frac{\hat{v}}{T}$ and $\frac{\gamma}{RPr}\frac{\partial^2}{\partial y^2}\left(\mu\hat{T}\right)$ are negligible and the phase shift of $\frac{1}{T}\left(-i\omega\hat{T}+U\frac{\partial\hat{T}}{\partial x}\right)$ is mainly due to the mean-flow convection. Then the thermal convection $-\frac{dT}{dy}\frac{\hat{v}}{T}$ becomes important during wave development. The contour of the temperature fluctuations illustrated in Figure 4.5 (d) shows the intensity of the temperature fluctuations at the critical layer increases continually as x^* increases, which results in a constant increase in the magnitude of $\frac{\gamma}{RPr}\frac{\partial^2}{\partial y^2}\left(\mu\hat{T}\right)$. Ultimately, the increased $\frac{\gamma}{RPr}\frac{\partial^2}{\partial y^2}\left(\mu\hat{T}\right)$ sustains the equilibrium of the phase shift of $\frac{1}{T}\left(-i\omega\hat{T}+U\frac{\partial\hat{T}}{\partial x}\right)$ crossing the critical layer.

4.3 Stabilization on the Second Mode

Theoretical analyses based on LST indicate that porous walls with an admittance phase approaching π have an efficient stabilization effect on the second mode instabilities. Here a porous wall listed in Table 4.1 is employed to validate the stabilization effect. The parameters of the disturbances are also provided in Table 4.1.

Table 4.1 Parameters of the actuator and porous wall

Disturbances		Porous wall		
Frequency (f^*)	Amplitude (ε)	Admittance magnitude ($\|A\|$)	Admittance phase (θ)	Location
138.74kHz	0.001	2	π	0.08m~0.16m

Figure 4.9 illustrates the growth rate and phase speed, obtained both from DNS and LST, of perturbations in the porous-wall case. Notably, in the LST computations, the porous wall is originated from near the leading-edge region in order to differentiate the fast and slow modes. It can be seen that both the growth rate and phase speed from DNS align with those of the slow mode in the region where the growth rate of the slow mode approaches its peak. Figure 4.10(a) compares the pressure disturbance amplitude between the porous-wall case and the smooth-solid-wall case (baseline). It is evident that the disturbance pressure magnitude in the porous-wall case rises more slowly than that in the baseline case due to the smaller growth rate depicted in Figure 4.10(b).

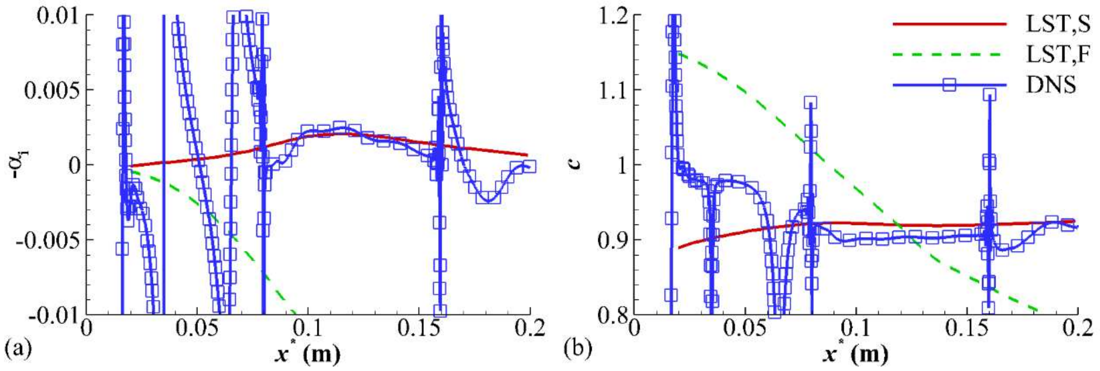

Figure 4.9 (a) growth rate and (b) phase speed of perturbations in the porous-wall case with the admittance of $A = 2\exp(\pi i)$. In the LST computations, the porous wall is originated from near the leading-edge region.

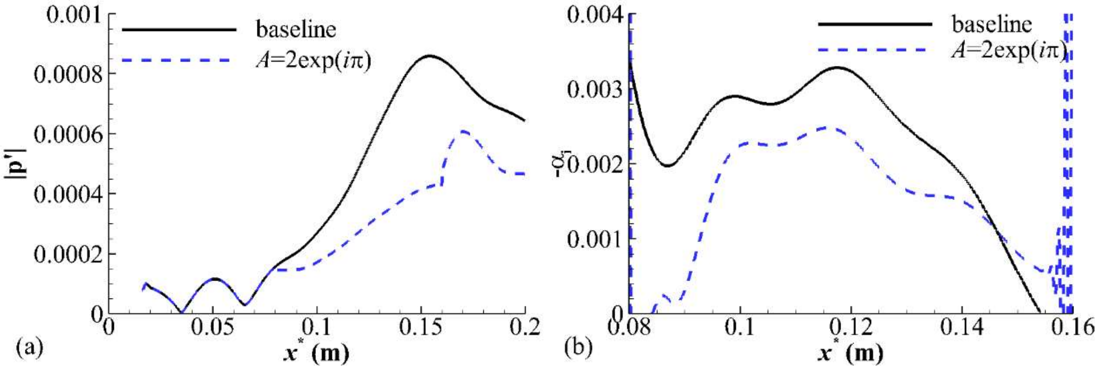

Figure 4.10 Comparison in the distributions of (a) wall-pressure-fluctuation amplitude and (b) growth rate between the porous-wall case and smooth-solid-wall case (baseline).

Figure 4.11 compares the contours of the disturbance components between the porous-wall case and baseline case in the region where the growth rate is high. It is distinct that fluctuations are damped when the porous wall is applied, particularly the near-wall fluctuations. Moreover, the spatial structure of disturbances in the porous-wall case is basically reserved compared with the baseline case.

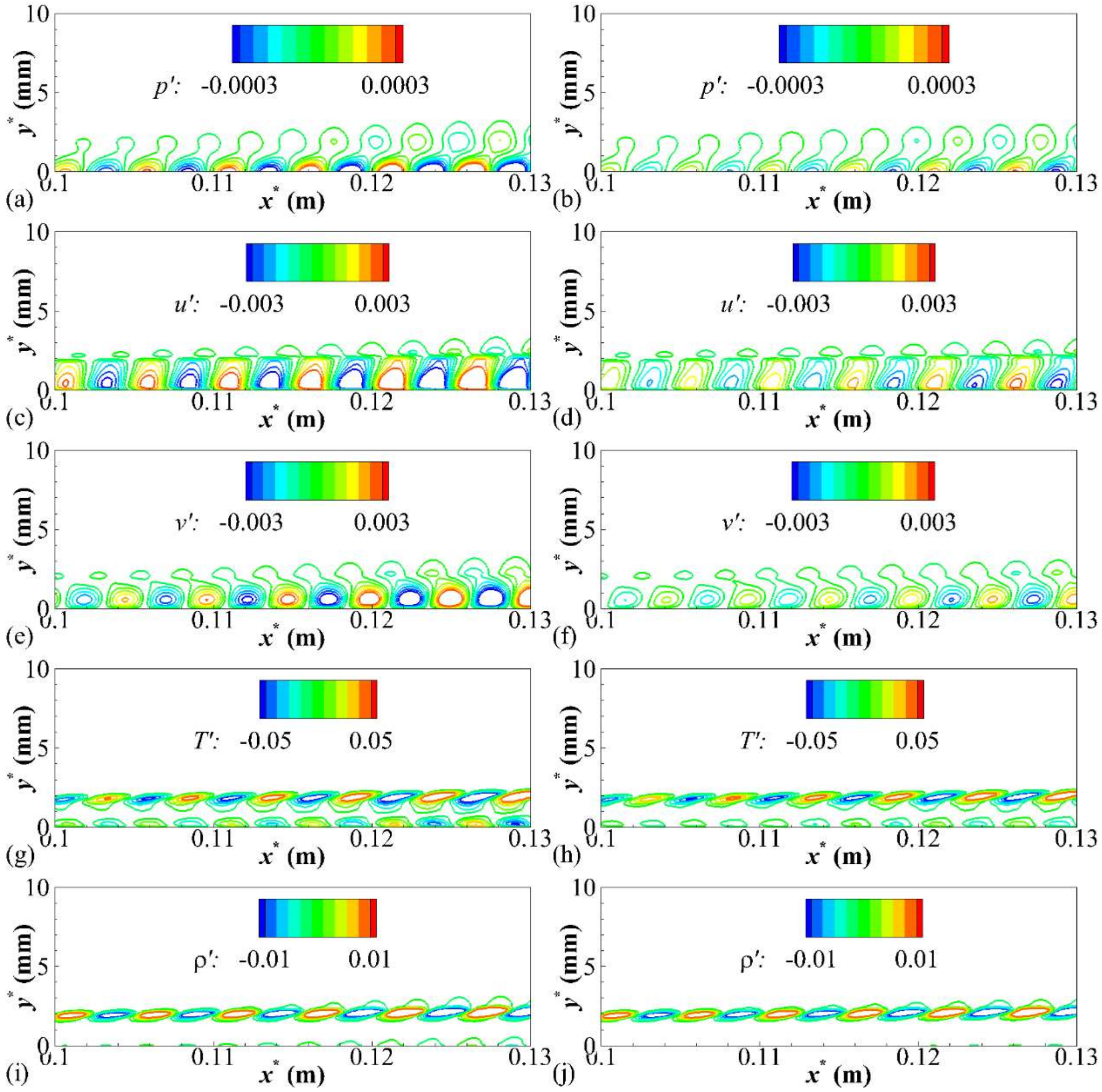

Figure 4.11 Comparison of instantaneous disturbance components between the smooth solid wall (left-hand plots) and the porous wall (right-hand plots) with the admittance of $A = 2\exp(\pi i)$ at the same timestamp.

In Chapter 3, it is found that the stabilization of the second mode is accompanied by the disruption of the in-phase relation between the total time rate of change of fluctuating internal energy and the energy transport by the wall-normal velocity fluctuation. Here we continue to investigate the mechanisms of stabilization on the second mode caused by porous walls based on the DNS computations. Likewise, the terms $\frac{1}{T}\left(-i\omega\hat{T}+U\frac{\partial\hat{T}}{\partial x}\right)$, $-\frac{dT}{dy}\frac{\hat{v}}{T}$ and $-(\gamma-1)\left(\frac{\partial\hat{u}}{\partial x}+\frac{\partial\hat{v}}{\partial y}\right)$ are examined in their magnitude and phase. Figure 4.12 compares the profiles of magnitude and phase of these terms at $x^*=0.11\mathrm{m}$ between the smooth-solid-wall case and porous-wall case.

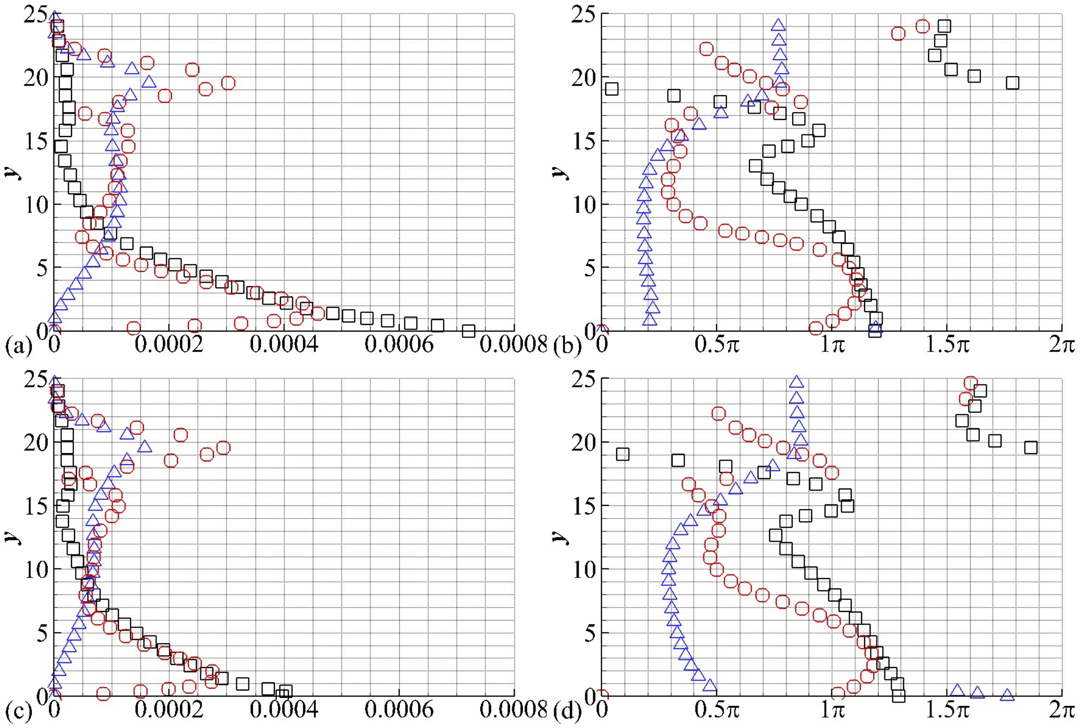

Figure 4.12 Comparison in magnitude (left-hand plots) the phase (right-hand plots) of $\frac{1}{T}\left(-i\omega\hat{T}+U\frac{\partial\hat{T}}{\partial x}\right)$(○), $-\frac{dT}{dy}\frac{\hat{v}}{T}$ (△) and $-(\gamma-1)\left(\frac{\partial\hat{u}}{\partial x}+\frac{\partial\hat{v}}{\partial y}\right)$ (□) between the smooth-solid-wall (top) and porous-wall (bottom) cases at $x^*=0.11\mathrm{m}$.

By comparing the magnitude plots, presented in Figure 4.12 (a) and (c), it can be seen that in contrast to the smooth-solid-wall case, the intensity of the fluctuations around the critical layer ($y\approx 17$) is little diminished, but the fluctuations near the wall are inhibited evidently. It indicates the near-wall fluctuations are more sensitive to the growth rate than those around the critical layer. Indeed, the internal energy fluctuations in the vicinity are mainly sustained by the mean-flow advection of perturbed thermal energy while the energy transport by the wall-normal velocity fluctuation is of small account. By contrast, near the wall, the energy transport by the wall-normal velocity fluctuation is significant for the dilatation fluctuation, though its magnitude is much less than that of the energy change due to dilatation fluctuations. Consequently, a trifling change in the energy transport by the wall-normal velocity fluctuation results in a distinct impact on the dilatation fluctuation.

The comparison between Figure 4.12 (b) and (d), shows the phase discrepancy of $\frac{1}{T}\left(-i\omega\hat{T}+U\frac{\partial\hat{T}}{\partial x}\right)$ and $-\frac{dT}{dy}\frac{\hat{v}}{T}$ around the critical layer in the porous-wall case is more evident than that in the smooth-solid-wall case, as shown in Figure 4.12(b) and (d). This phenomenon is consistent with the comparison in the growth rate between these two cases, as shown in Figure 4.10(b). It confirms again that the amplification of the second mode is associated with the phase overlap of $\frac{1}{T}\left(-i\omega\hat{T}+U\frac{\partial\hat{T}}{\partial x}\right)$ and $-\frac{dT}{dy}\frac{\hat{v}}{T}$ around the critical layer.

Figure 4.12 (d) demonstrates that below the critical layer, the phase of $-\frac{dT}{dy}\frac{\hat{v}}{T}$ is distinctly affected, which influences the phase discrepancy of $\frac{1}{T}\left(-i\omega\hat{T}+U\frac{\partial\hat{T}}{\partial x}\right)$ and $-\frac{dT}{dy}\frac{\hat{v}}{T}$ around the critical layer. Here we focus on the disturbance components to investigate the way that the porous wall reconstructs the phase relation of $\frac{1}{T}\left(-i\omega\hat{T}+U\frac{\partial\hat{T}}{\partial x}\right)$ and $-\frac{dT}{dy}\frac{\hat{v}}{T}$. The magnitude and phase of the disturbance components $\hat{p}$, $\hat{v}$ and $\hat{T}$ are depicted in Figure 4.13.

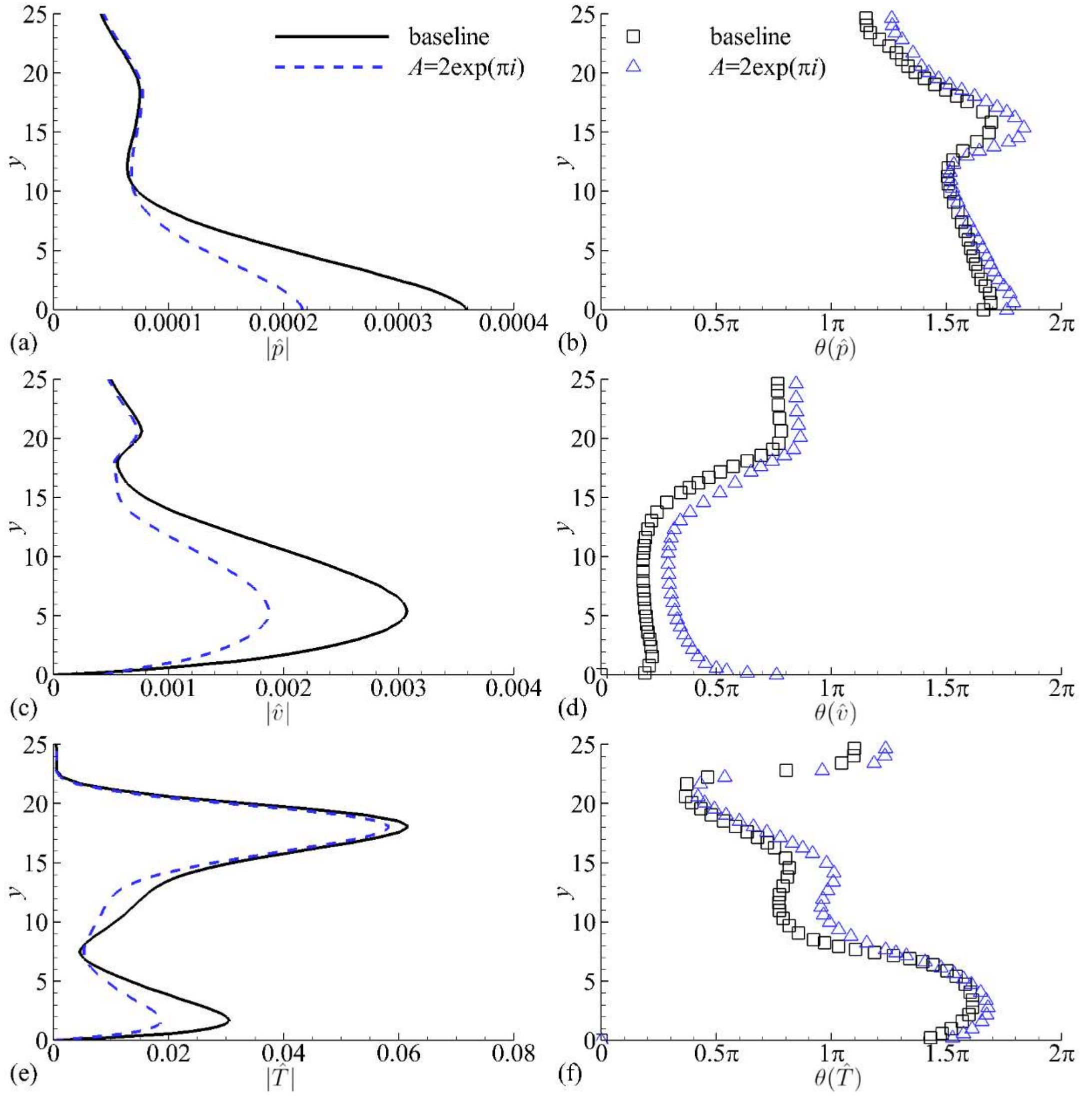

Figure 4.13 Comparison in the magnitude (left-hand plots) and phase (right-hand plots) profiles of perturbations of pressure, wall-normal velocity and temperature at $x^* = 0.11\mathrm{m}$ between the smooth-solid wall case (baseline) and porous-wall case.

Considering a normal incident wave with the velocity of $v'(x,y,t) = \hat{v}(x,y)e^{-i\omega t}$ (phase varies from 2π to 0 in a circle along with the time increasing), the porous wall with the admittance phase of π delays its reflection (i.e. a rightward phase shift), as shown in Figure 4.13 (d). Moreover, this delay affects the phase of the wall-normal velocity fluctuation in the far field. According to Figure 4.13 (f), the phase of $\hat{T}$ in the regions above the critical layer ($y \approx 17$) and near the wall ($y < 7$) is slightly adjusted. However, the phase of $\hat{T}$ at moderate y, namely $7 < y < 17$, is remarkably delayed. It is noted that phase delay represents the change in the interplay between the critical-layer fluctuation and near-wall fluctuation. Consequently, the phase delay in the wall-normal velocity fluctuation and the phase delay of the temperature fluctuation at moderate y account for the trimming in the phase overlap of $\frac{1}{T}\left(-i\omega\hat{T} + U\frac{\partial\hat{T}}{\partial x}\right)$ and $-\frac{dT}{dy}\frac{\hat{v}}{T}$ in the vicinity of the critical layer in the porous-wall case.

4.4 Destabilization on the Second Mode

The second mode associated with either the slow mode or the fast mode depends on the wall condition. Commonly, the slow mode is unstable when the ratio of the wall temperature and mean-flow temperature is relatively high [65]. In Chapter 3, it is found that porous walls can overturn the eigenmode branch if the real part of the admittance of porous walls is positive and exceeds a threshold. In practice, a positive real part of admittance is rare for the porous walls composed of random or regular microstructures. This section is aimed to investigate the scenario that the fast mode is destabilized. The parameters of disturbances and the porous wall are listed in Table 4.2.

Table 4.2 Parameters of disturbances and porous wall

Disturbances	Porous wall

Frequency (f^*)	Amplitude (ε)	Admittance magnitude ($\|A\|$)	Admittance phase (θ)	Location
138.74kHz	0.001	*2*	0	0.08m~0.16m

Figure 4.14 compares the growth rate and phase speed of disturbances between DNS and LST computations. The growth rate of the unstable wave obtained from DNS agrees well with the fast mode in the region of a high growth rate, as shown in Figure 4.14(a). Whereas the phase speed obtained from DNS is lower than the fast mode and closer to the slow mode, as shown in Figure 4.14 (b). Indeed, the wave propagation speed near the wall is slowed down by the fluid viscosity, which is analogous to the smooth-solid-wall case. Therefore, the growth of perturbations in the current porous-wall case is dominated by the fast mode.

Figure 4.15(a) shows the porous wall remarkably destabilizes the pressure fluctuation due to the large growth rate depicted in Figure 4.15(b). This destabilization effect is consistent with the LST predication conducted in Chapter 3.

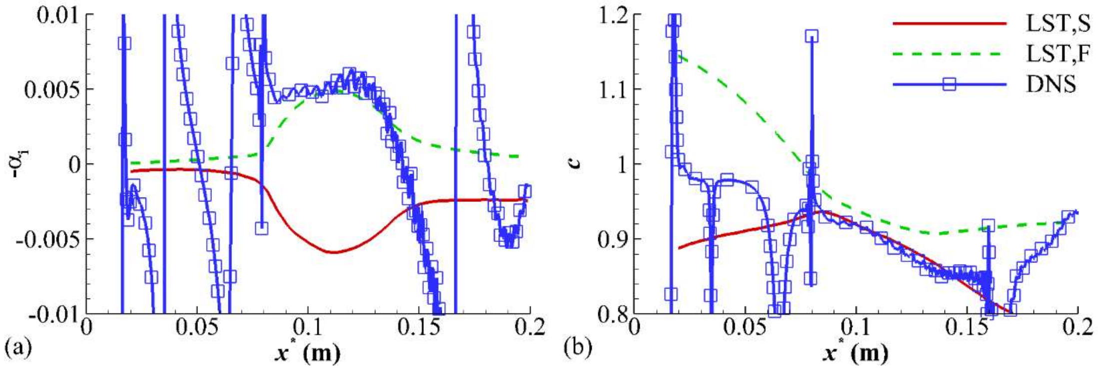

Figure 4.14 Comparison in (a) growth rate and (b) phase speed of perturbations between DNS and LST with the admittance of $A = 2$.

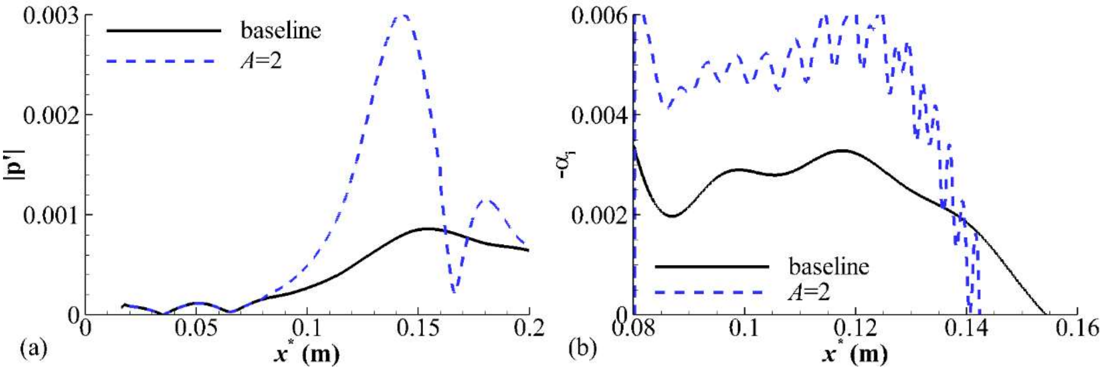

Figure 4.15 Comparison in the distribution of (a) wall-pressure-fluctuation magnitude and (b) growth rate between the porous-wall case ($A = 2$) and the smooth-solid-wall case (baseline).

Figure 4.16 compares the contours of the instantaneous disturbance components between the porous-wall case and the smooth-porous-wall case. The spatial structure of wave packets governed by the fast mode is evidently distinct from that governed by the slow mode in the smooth-solid-wall case. In the porous-wall case, the pressure fluctuations, wall-normal velocity disturbances, and density fluctuations even extend beyond the boundary layer, while the temperature fluctuations, streamwise velocity disturbances are consistently constrained within the boundary layer.

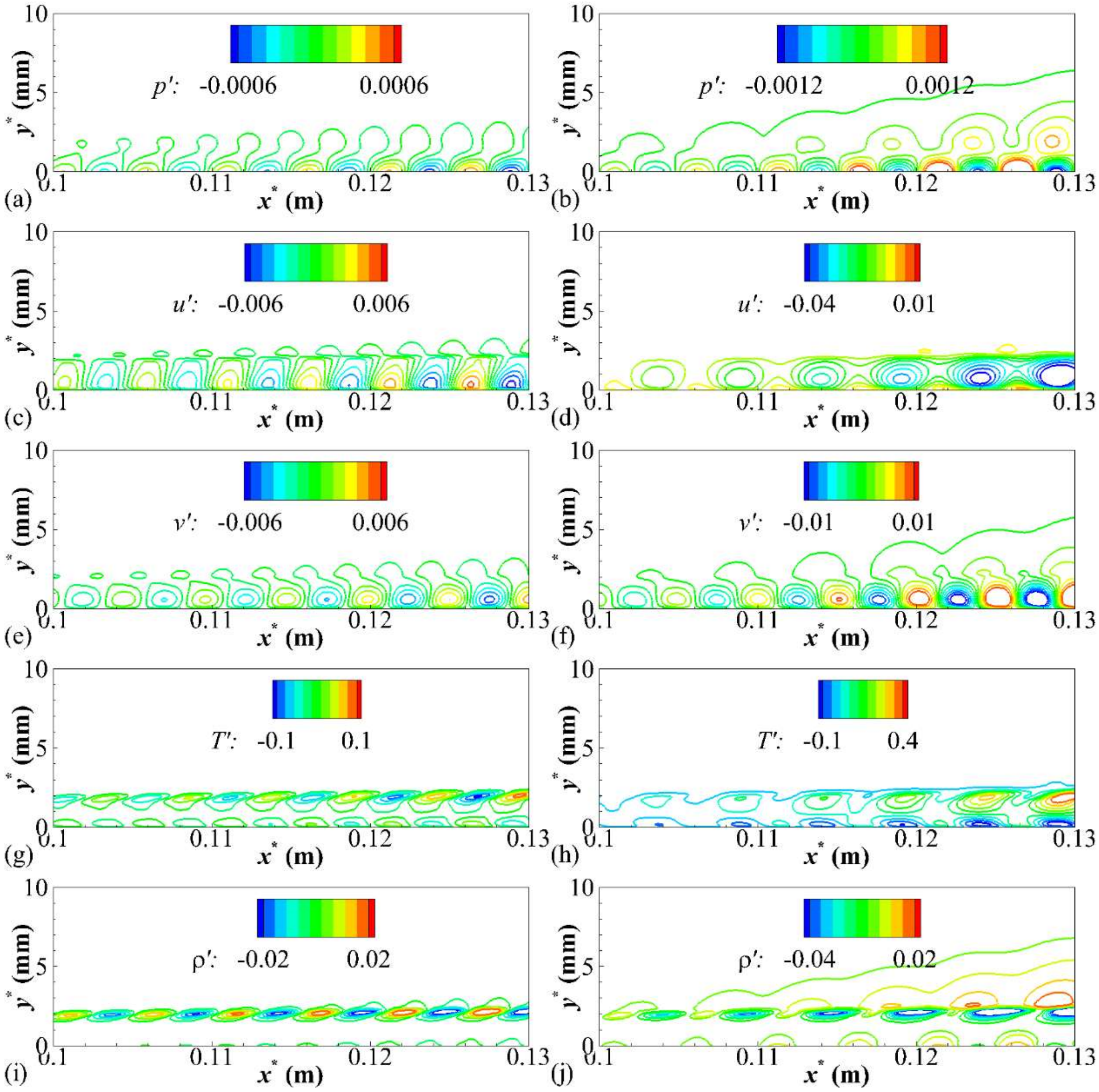

Figure 4.16 Comparison of instantaneous disturbance components between the smooth solid wall (left-hand plots) and the porous wall with the admittance of $A = 2$ (right-hand plots) at the same timestamp.

Figure 4.17 compares the terms $\frac{1}{T}\left(-i\omega\hat{T}+U\frac{\partial\hat{T}}{\partial x}\right)$, $-\frac{dT}{dy}\frac{\hat{v}}{T}$ and $-(\gamma-1)\left(\frac{\partial\hat{u}}{\partial x}+\frac{\partial\hat{v}}{\partial y}\right)$ in their magnitude and phase between the porous-wall case and the smooth-solid-wall case. It is remarkable that in the porous-wall case the phase of $\frac{1}{T}\left(-i\omega\hat{T}+U\frac{\partial\hat{T}}{\partial x}\right)$ is superposed on that of $-\frac{dT}{dy}\frac{\hat{v}}{T}$ not only in the vicinity of the critical layer but also at moderate y. Therefore, the energy transport by the wall-normal velocity fluctuation has a great contribution to the internal energy fluctuations in the porous-wall case. In return, the wall-normal energy transport is also promoted by the augmentation in the internal energy fluctuations, particularly in the region below the critical layer.

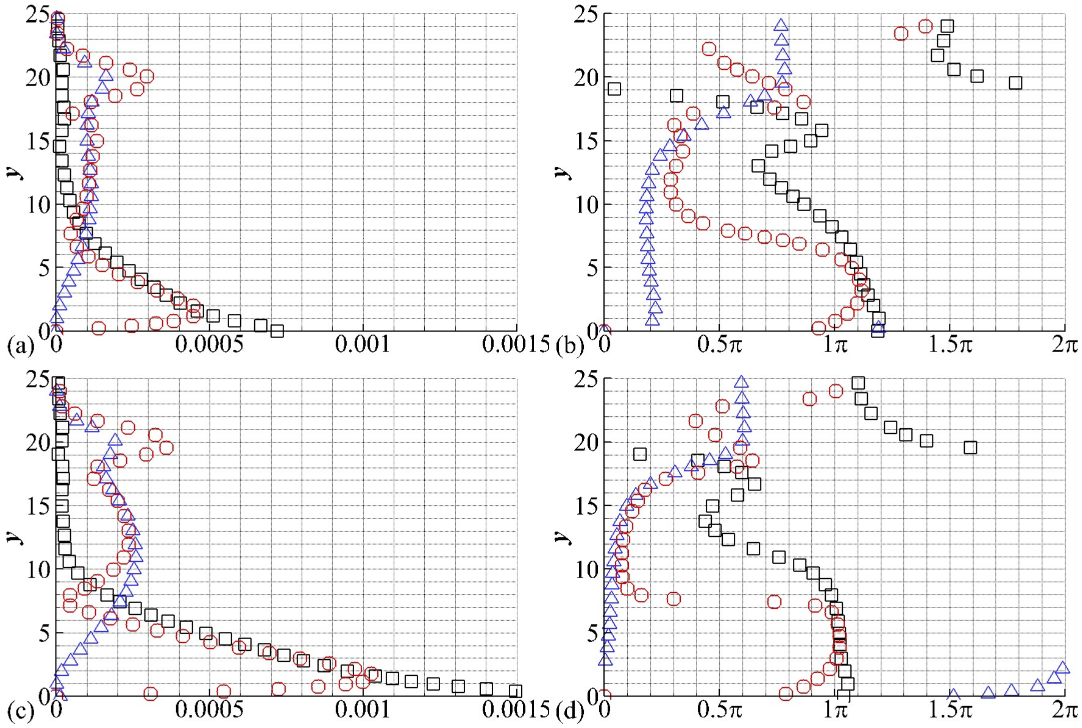

Figure 4.17 Comparison in magnitude (left-hand plots) the phase (right-hand plots) of $\frac{1}{T}\left(-i\omega\hat{T}+U\frac{\partial\hat{T}}{\partial x}\right)$(○), $-\frac{dT}{dy}\frac{\hat{v}}{T}$ (△) and $-(\gamma-1)\left(\frac{\partial\hat{u}}{\partial x}+\frac{\partial\hat{v}}{\partial y}\right)$ (□) between the smooth-solid-wall (top) and porous-wall (bottom) cases at $x^*=0.11\mathrm{m}$.

Figure 4.17(c) shows the near-wall dilatation fluctuations are also greatly elevated in the porous-wall case. Apparently, this elevation is closely associated with the increase in the energy transport by the wall-normal velocity fluctuation. As the porous wall firstly affects the near-wall perturbations, the change in the near-wall dilatation fluctuations results in the broad phase overlap between $\frac{1}{T}\left(-i\omega\hat{T}+U\frac{\partial\hat{T}}{\partial x}\right)$ and $-\frac{dT}{dy}\frac{\hat{v}}{T}$ in the region away from the wall. To crystallize the phase variation caused by the porous wall, we examine the disturbance components in their magnitude and phase, as shown in Figure 4.18.

Figure 4.18 compares the disturbance components $\hat{p}$, $\hat{v}$ and $\hat{T}$ between the porous-wall case and the smooth-solid-wall case at $x^* = 0.11\mathrm{m}$. It is evident that the phase of $\hat{v}$ shift leftwards entirely in the porous-wall case compared with the smooth-solid-wall case in Figure 4.18 (d). From Figure 4.18(f), we can see that a phase advance of $\hat{T}$ emerges at moderate y. As a result, the phase shifts in $\hat{v}$ and $\hat{T}$ lead to the high phase overlap of $\frac{1}{T}\left(-i\omega\hat{T} + U\frac{\partial\hat{T}}{\partial x}\right)$ and $-\frac{dT}{dy}\frac{\hat{v}}{T}$. In the following we analyze the reason of the phase shifts in $\hat{v}$ and $\hat{T}$.

Considering a normal incident wave in a form of $v'(x,y,t) = \hat{v}(x,y)e^{-i\omega t}$ propagating towards the wall, it is compelled to reflect forward by the porous wall when the near-wall fluid elements are in the contraction stage (i.e. $p' > 0$) as $v' = 2p'$ at the wall. While in the thermal expansion stage, the near-wall fluid elements are accelerated to move towards the wall. Therefore, the phase of $\hat{v}$ is brought forward. Moreover, this early reflection facilitates the thermal contraction and the acceleration of fluid elements to the wall strengthens the thermal expansion, which both aggravate the near-wall dilatation fluctuation. In return, the augmentation in the dilatation fluctuation accelerates the wall-normal fluctuating velocity at moderate y, which escalates the wall-normal energy transport. Figure 4.17(c) shows that the total time rate of change of fluctuating internal energy is accounted for by the wall-normal energy transport at moderate y. Therefore, the phase of $\hat{T}$ is concomitantly advanced.

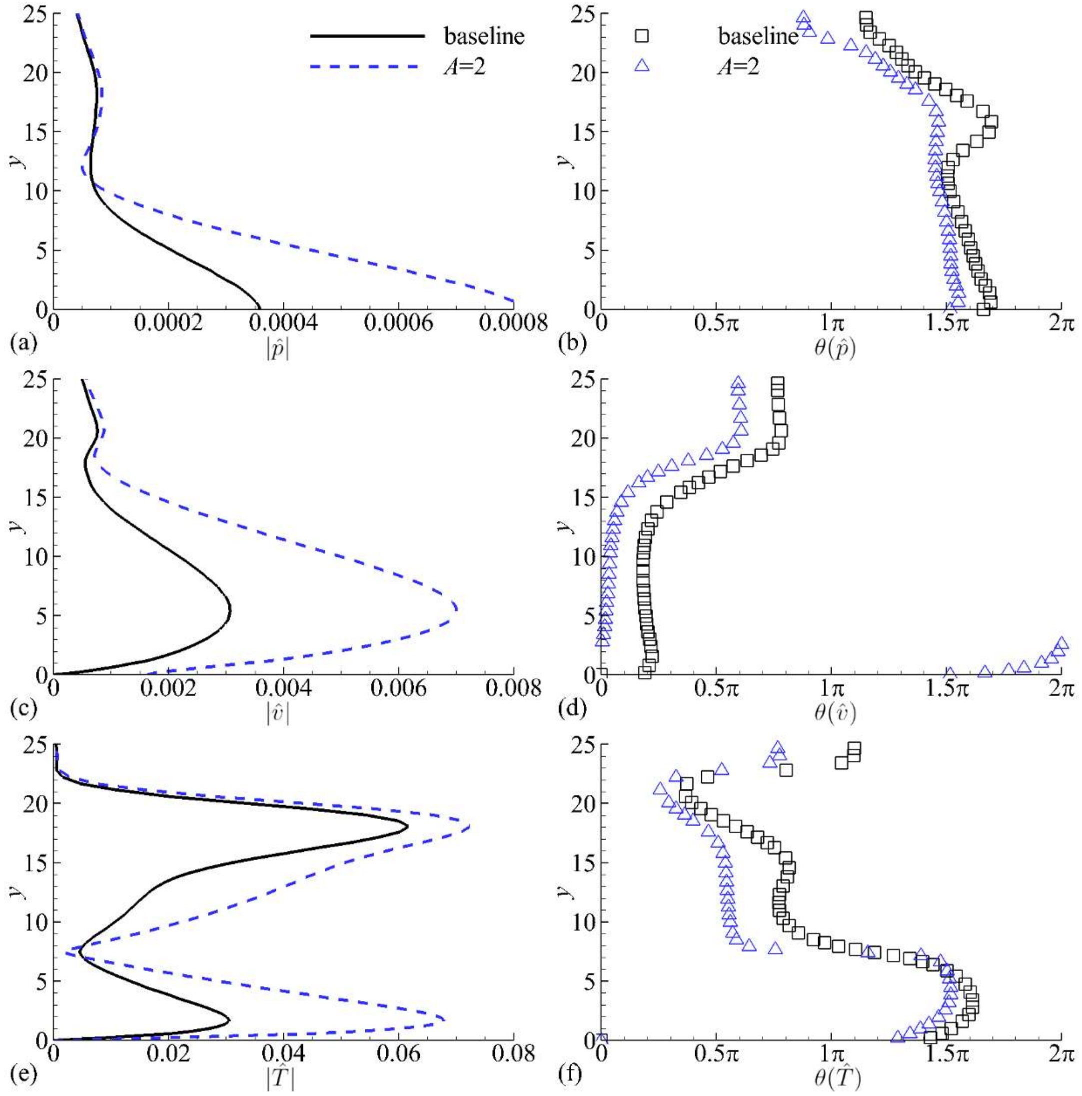

Figure 4.18 comparison in the magnitude (left-hand plots) and phase (right-hands plot) of perturbations of pressure, wall-normal velocity and temperature at $x^* = 0.11\mathrm{m}$ between the smooth-solid-wall case (baseline) and porous-wall case.

4.5 Frequency Shift

According to the theoretical analyses based on LST, the non-dimensional angular frequency ω has a shift when a porous wall with admittance phase tending to 0.5π or 1.5π is applied. If $\theta = 0.5\pi$, it shifts to the low-frequency band, while if $\theta =$

1.5π, a shift to the high-frequency band emerges. In the DNS computations, disturbances have a fixed frequency, therefore the frequency shift is converted to a spatial shifting of disturbances as $\omega = \frac{2\pi f^*}{U_\infty^*}\sqrt{\frac{\nu^* x^*}{U_\infty^*}}$. Here we analyze this spatial shifting based on DNS computations. The parameters of the disturbances and porous walls are shown in Table 4.3.

Table 4.3 Parameters of disturbances and porous wall

Disturbances		Porous wall		
Frequency (f^*)	Amplitude (ε)	Admittance magnitude ($\|A\|$)	Admittance phase (θ)	Location
138.74kHz	0.001	2	0.5π	0.08m~0.16m
		2	1.5π	0.08m~0.16m

The growth rate and phase speed based on the wall disturbance pressure for the porous-wall cases are depicted in Figure 4.19. The LST results are provided for comparison. It can be seen that the DNS solutions have an excellent agreement with the slow mode obtained from LST in the linear growth region, which indicates the evolutions of the instability waves in these two porous-wall cases are dominated by the slow mode.

Figure 4.20(a) compares the wall pressure fluctuation amplitude of the two porous-wall cases with the baseline. It clearly demonstrates the pressure perturbations are amplified in advance when $\theta = 0.5\pi$ and delayed to rise when $\theta = 1.5\pi$ in contrast to the baseline case. The growth rate illustrated in Figure 4.20(b) also exhibits that the peak growth rate moves upstream when $\theta = 0.5\pi$, and downstream when $\theta = 1.5\pi$. This is consistent with the non-dimensional frequency shift predicted by LST.

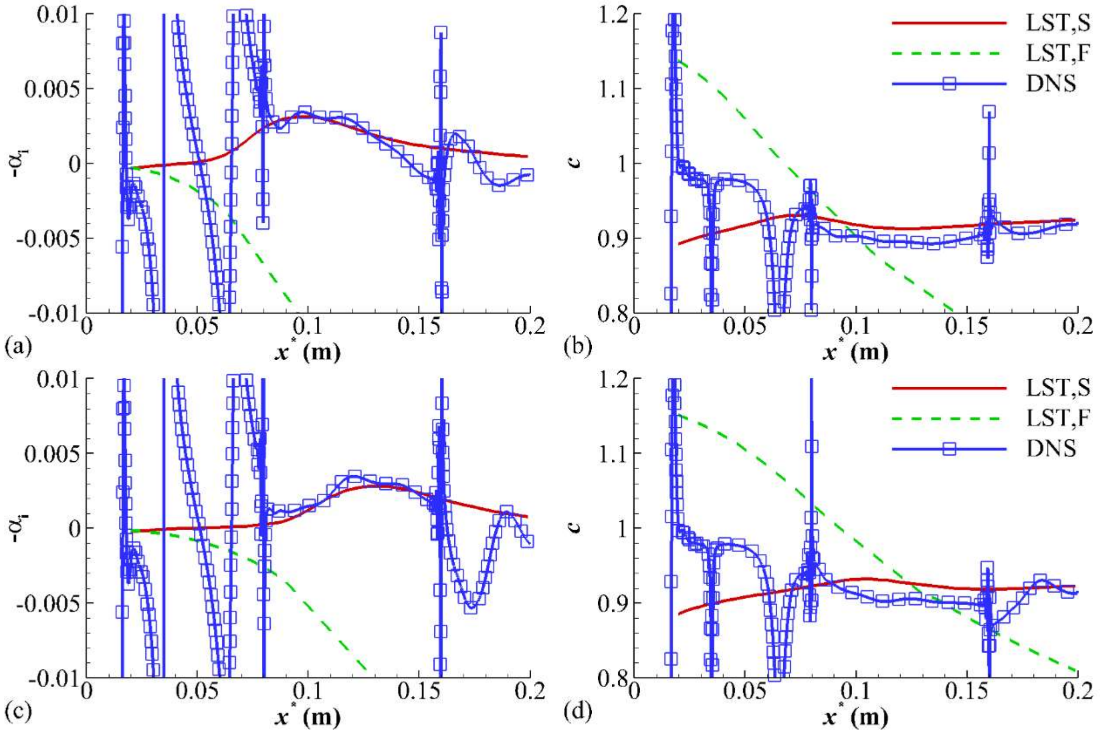

Figure 4.19 Comparison in growth rate (left-hand plots) and phase speed (right-hand plots) of perturbations obtained from DNS and LST at different admittances: (a) (b) $A = 2\exp(0.5\pi i)$, (c) (d) $A = 2\exp(1.5\pi i)$.

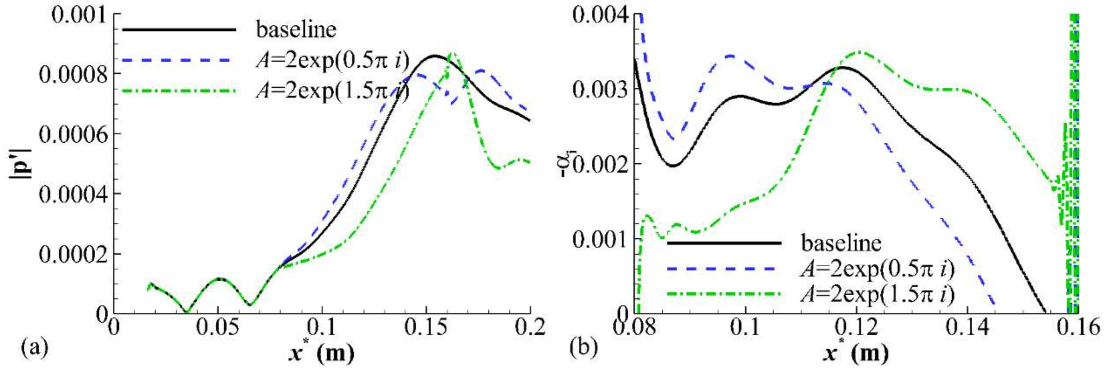

Figure 4.20 Comparisons in the distribution of (a) the wall pressure fluctuation amplitude and (b) growth rate among different walls.

Figure 4.21 compares the contours of the instantaneous pressure fluctuations of the porous-wall cases with the smooth-solid-wall case. We can observe that the spatial cell structures of pressure fluctuations on the porous walls move upstream or downstream depending on the admittance phases. Moreover, the movement of the cell structures is in an integrated manner and there is no crystal distortion appearing in such structures, which suggests that the porous walls do not change the mechanisms of the amplification of the second mode waves, but result in phase variations in the fluctuating energy terms.

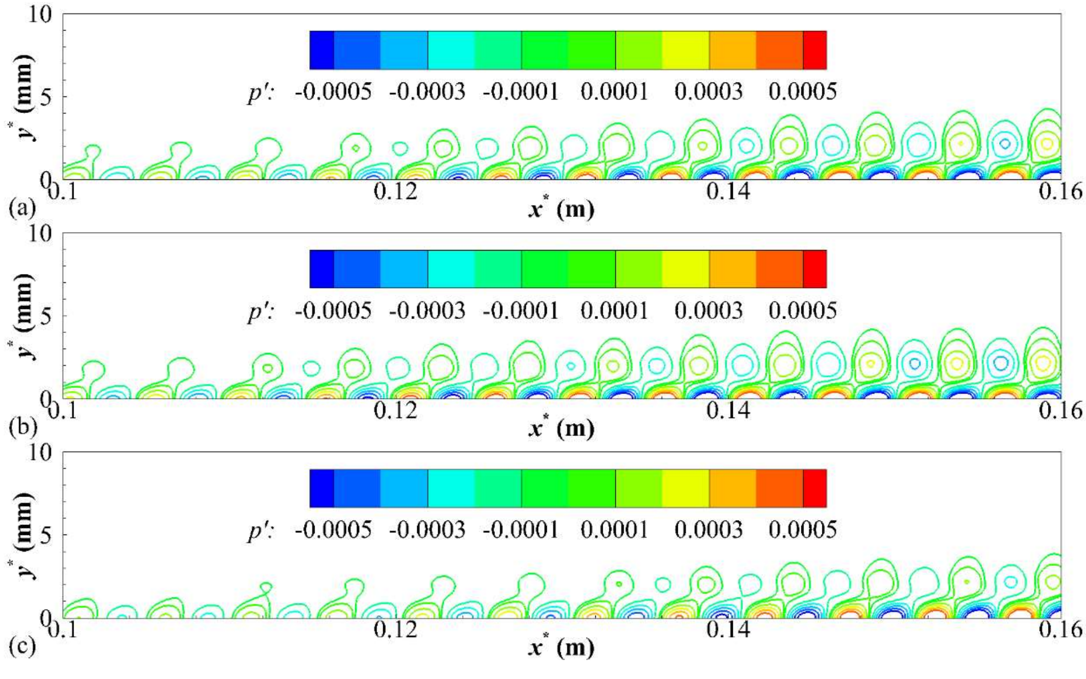

Figure 4.21 Contours of instantaneous pressure fluctuations in (a) the smooth-solid-wall case and the porous-wall cases with admittances of (b) $A = 2\exp(0.5\pi i)$ and (c) $A = 2\exp(1.5\pi i)$.

Figure 4.22 compares the magnitude and phase of the terms $\frac{1}{T}\left(-i\omega\hat{T} + U\frac{\partial\hat{T}}{\partial x}\right)$,

$-\frac{dT}{dy}\frac{\hat{v}}{T}$ and $-(\gamma-1)\left(\frac{\partial\hat{u}}{\partial x}+\frac{\partial\hat{v}}{\partial y}\right)$ among different wall conditions at $x^* = 0.1\mathrm{m}$. By comparing Figure 4.22 (b) (d) and (f), it is observed that the phase overlap between the terms $\frac{1}{T}\left(-i\omega\hat{T}+U\frac{\partial\hat{T}}{\partial x}\right)$ and $-\frac{dT}{dy}\frac{\hat{v}}{T}$ around the critical layer ($y \approx 17$) is changed in porous-wall cases in contrast to the baseline case. The variation in this phase overlap is consistent with the change in the growth rate. Therefore, the premature or delayed amplification is due to the transform of the phases of $\frac{1}{T}\left(-i\omega\hat{T}+U\frac{\partial\hat{T}}{\partial x}\right)$ and $-\frac{dT}{dy}\frac{\hat{v}}{T}$ around the critical layer.

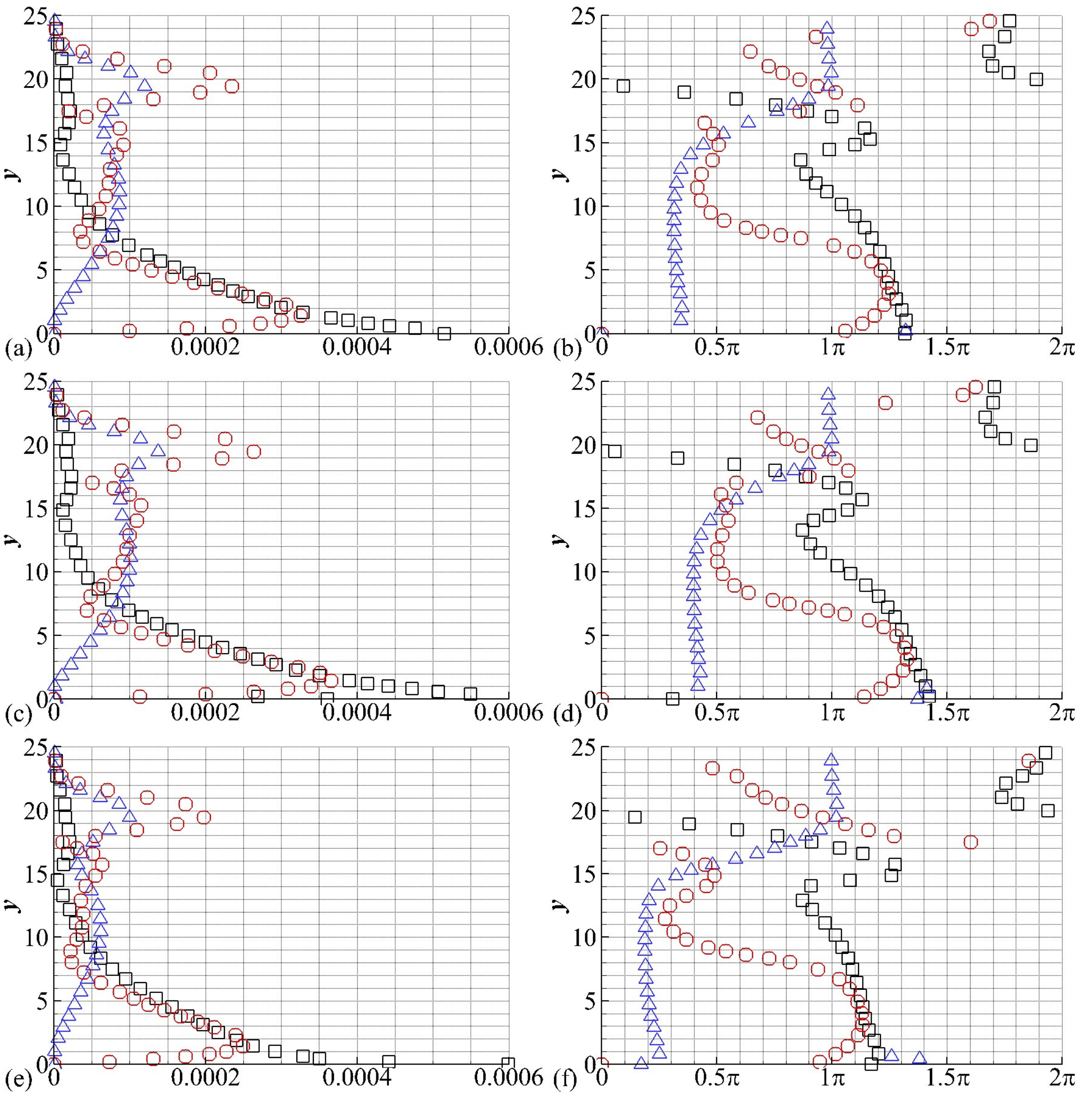

Figure 4.22 Comparison in magnitude (left-hand plots) the phase (right-hand plots) of

$\frac{1}{T}\left(-i\omega\hat{T}+U\frac{\partial\hat{T}}{\partial x}\right)$(○), $-\frac{dT}{dy}\frac{\hat{v}}{T}$ (△) and $-(\gamma-1)\left(\frac{\partial\hat{u}}{\partial x}+\frac{\partial\hat{v}}{\partial y}\right)$ (□) among the smooth-solid-wall (top) and porous-wall cases with $A=2\exp(0.5\pi i)$ (middle) and $A=2\exp(1.5\pi i)$ (bottom) at $x^*=0.1\mathrm{m}$.

Figure 4.23 compares the wall-normal velocity, pressure, and temperature perturbations among these three cases. Concerning disturbances with time dependence of $exp(-i\omega t)$, the wall-normal velocity $\hat{v}$ has a phase advance of 0.5π compared with $\hat{p}$ near the wall in the baseline case. For the case with the admittance of $A=2\exp(0.5\pi i)$, the wall-normal velocity is $\hat{v}=2\hat{p}\,exp(0.5\pi i)$ at the wall, which is identical to the phase relation of $\hat{v}$ and $\hat{p}$ of the baseline case. As $\hat{v}$ is nonzero at the wall in this porous-wall case, the perturbation near the wall is exacerbated. By contrast, for the case with the admittance of $A=2\,exp(1.5\pi i)$, the wall-normal fluctuating velocity is $\hat{v}=2\hat{p}\exp(1.5\pi i)=2\hat{p}\exp(-0.5\pi i)$. The phase of $\hat{v}$ at the wall is reversed forcibly, which results in a decrease in the magnitude of $\hat{v}$ against the wall. These analyses are in accord with the near-wall performance of the perturbation components shown in Figure 4.23(a) (c) and (e).

From Figure 4.23 (b), (d), and (f), it is notable that below the critical layer, the strong perturbations correspond to a rightward shift in phase, while the weak perturbations correspond to a leftward shift in phase. In other words, strong perturbations propagate slower than weak perturbations. Considering the intensity of perturbations, we conjecture the near-wall phase shift may be accounted for by the fluid viscosity. In addition, the phases of the disturbance components $\hat{p}$, $\hat{v}$ and $\hat{T}$

remain constant in the far field, which is because the mean-flow advection is in charge of the wave propagation in the far field. Therefore, the phase shift of the disturbance components below the critical layer results in the spatial shift of disturbances.

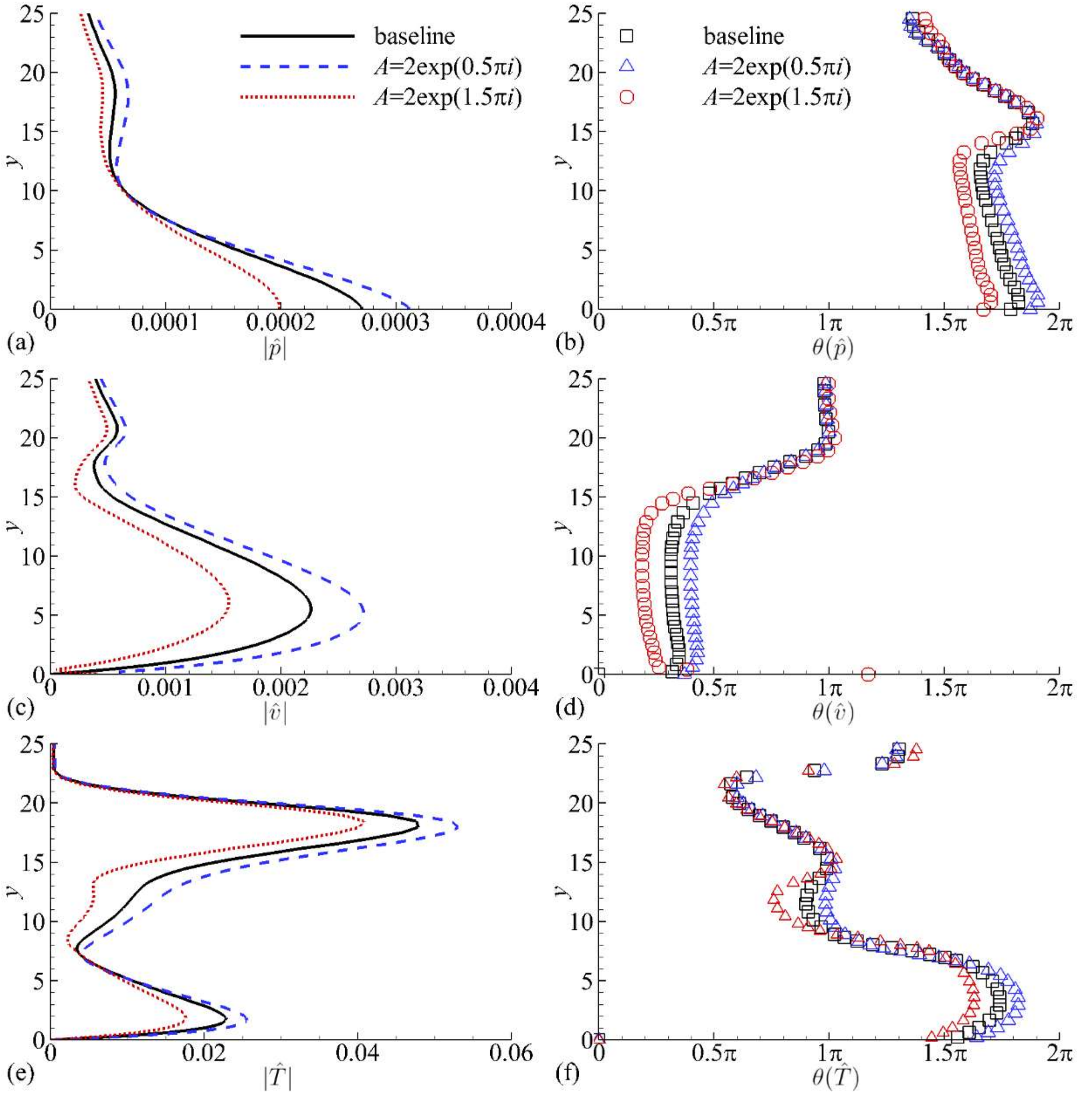

Figure 4.23 Comparison in magnitude (left-hand plots) and phase (right-hand plots) of the pressure, wall-normal velocity and temperature perturbations at $x^* = 0.1\mathrm{m}$ among the smooth-solid-wall case (baseline) and porous-wall cases.

In conclusion, the porous wall strengths or mitigates the near-wall perturbations according to the phase relation of v' and p', and the variation in the disturbance intensity alters the fluid viscosity, leading to the phase shifts of disturbance components. The phase shifts of the wall-normal fluctuating velocity and disturbance temperature result in the premature or delayed amplification of the second mode instability.

4.6 Summary

The numerical simulations have confirmed the effects of porous walls on the second-mode instabilities obtained by LST analysis. Meanwhile, the phase analyses on the disturbance energy equation with the DNS results employed provide further insight into the mechanisms of the stabilization, destabilization, and frequency shift of the second mode caused by porous walls.

In the propagation of the second-mode waves, the variation of the critical-layer phase overlap between $\frac{1}{T}\left(-i\omega\hat{T}+U\frac{\partial\hat{T}}{\partial x}\right)$ and $-\frac{dT}{dy}\frac{\hat{v}}{T}$, which is due to the inconsistency of the phase shifts of $\frac{1}{T}\left(-i\omega\hat{T}+U\frac{\partial\hat{T}}{\partial x}\right)$ and $-\frac{dT}{dy}\frac{\hat{v}}{T}$ across the critical layer, is consistent with the distribution of the growth rate. Porous walls alter the magnitude and phase of the wall-normal fluctuating velocity at the wall, which results in a change in the near-wall dilatation fluctuation. In the stabilized or destabilized case, the phase of the wall-normal fluctuating velocity is delayed or advanced entirely, respectively. Meanwhile, the phase of the temperature fluctuation at moderate y is adjusted to adapt the change in the near-wall dilatation fluctuation. The frequency shift of the second mode is associated with phase shifts of disturbance components below the critical layer, which are evoked by the intensity change of the near-wall dilation fluctuation.

Chapter 5 Design of Ultrasonic Absorptive Coatings for the Stabilization of a Supersonic Boundary Layer

This chapter describes a reverse design strategy for the ultrasonic absorptive coating (UAC) design to stabilize the first and second modes. Unlike the foregoing analyses which are based on boundary layers with free-stream Mach number of 6, this chapter focuses on a flat-plate boundary layer with free-stream Mach number of 4, in which the first and second mode coexist and both are significant for the boundary layer transition.

5.1 Effect of Porous Walls on the First and Second Modes

In this Chapter, the flow conditions listed in Table 5.1 are used and these conditions can be implemented in the Ludwieg tube built in The Hong Kong Polytechnic University. The gas is assumed to be calorically perfect. The Prandtl number is $Pr = 0.72$ and the specific heat rate is $\gamma = 1.4$. The viscosity is calculated using Sutherland's law. The boundary-layer-edge Mach number is assumed to be identical to the free-stream Mach number M_∞ as the shock waves at the leading edge of the flat plate are rather weak.

Table 5.1 Parameters of flow conditions

$P_0(\mathrm{kPa})$	$T_0(\mathrm{K})$	M_∞	$Re_1(\mathrm{m}^{-1})$	$T_w(\mathrm{K})$
300	295	4	13.9×10^6	295

For the calculations of boundary layer instabilities, LST is employed and the mean flow quantities are obtained from the self-similar solution. The contour of the growth rate of the first and second modes in the boundary layer on a smooth solid wall is depicted in Figure 5.1. It can be seen that the non-dimensional angular frequencies ω corresponding to the largest growth rate of the first and second modes basically maintain constant as the Reynolds number increases. And they are about 0.07 and 0.25 for the first and second modes, respectively. Due to the coexistence of the first and second modes, it should take the first- and second-mode instabilities into account simultaneously to stabilize the current boundary layer flow.

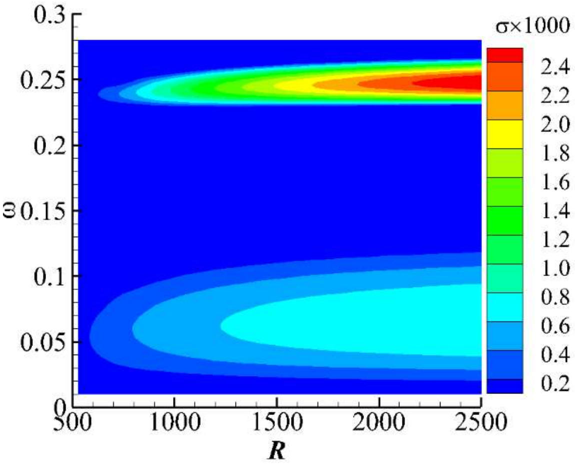

Figure 5.1 Contour of the growth rate of the first and second modes which correspond to the low-frequency and high-frequency bands, respectively, for the smooth solid wall. The Reynold number R is based on the boundary layer thickness scale.

To stabilize the first and second modes using porous walls, the influences of admittance magnitude $|A|$ and phase θ on the growth rate of the first and second modes are examined under different admittance magnitudes with the admittance phase in a range of $[0.5\pi,\ 1.5\pi]$, as shown in Figure 5.2.

Figure 5.2 shows in contrast to the smooth-solid-wall case (i.e. $A=0$), the second mode instabilities are efficiently damped as θ is a little larger than π but further amplified as θ tends to 0.5π. When θ approaches 1.5π, the second mode is still unstable if $|A|$ is not too large. Moreover, when the admittance phase inclines to 0.5π or 1.5π, a shift in the non-dimensional angular frequency ω of the second mode emerges. Regarding the first mode, the growth rate increases as θ in the vicinity of $\theta=\pi$ and slightly decreases as θ tends to 0.5π. Basically, the frequency band of the first mode is relatively broadened as $\theta\approx\pi$.

By comparing Figure 5.2 (b) (c) and (d), it can be seen that the aforementioned effects of porous walls on the first and second modes are facilitated by the increase in the admittance magnitude $|A|$. When $|A|=4$, the frequency bands of the first and second modes merge as θ is roughly in the vicinity of $\theta=0.75\pi$, which results in a wide frequency band of perturbations, which is adverse to delay the boundary layer transition.

In the current analyses, the wall temperature is close to the adiabatic wall temperature. Recalling the studies of the effects of porous walls on the hypersonic boundary instabilities carried out on the adiabatic wall in Chapter 3, we can conclude that under the adiabatic or quasi-adiabatic wall condition, the regularities of the effects of the porous walls with the admittance phase in the range of $[0.5\pi,\ 1.5\pi]$ on the first and second modes are similar between the supersonic and hypersonic boundary layers.

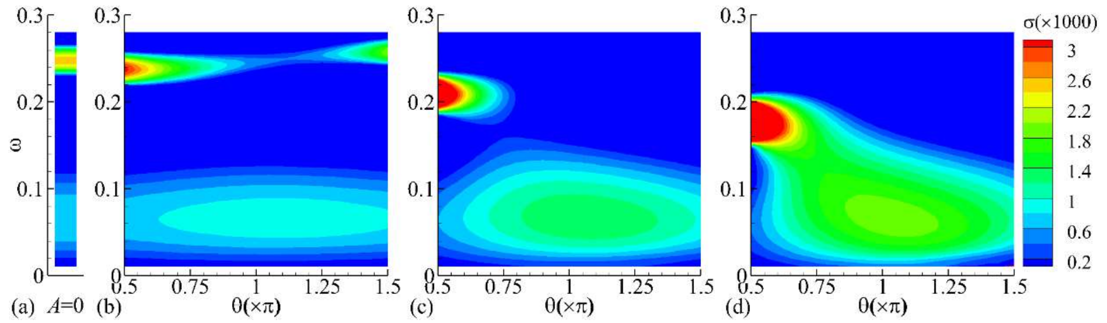

Figure 5.2 Growth rates of the first and second modes varied along with the non-dimensional angular frequency and admittance phase under different admittance magnitudes: (a) $A = 0$ denotes the smooth solid wall case (b) $|A| = 0.5$, (c) $|A| = 2$ and (d) $|A| = 4$. The calculations are conducted at $R = 2358$ ($x^* = 0.4\text{m}$).

5.2 Design Strategy

Previously proposed methodologies of UAC design focus on the reflective coefficient of a UAC for normal-incident waves as it represents the absorption capability of the UAC for high-frequency disturbances. In practice, a large reflective coefficient can also be performed by improving the porosity of a UAC, even the admittance phase differs from π greatly, which is unfavorable for the stabilization of the second mode. By contrast, if the admittance magnitude and phase of a UAC are provided, the growth rates of the first and second modes are easy to determine. Therefore, UAC can be designed based on the required admittance magnitude and phase.

As shown in Figure 5.1, the ranges of the non-dimensional angular frequency of the first and second modes are changed moderately as the Reynolds number increases.

Indeed, it indicates the first- or second-mode waves with different frequencies will be amplified at different locations. As we know, the disturbance frequencies are commonly indeterminate in flight environments. To stabilize the first- and second-mode instabilities in broadband, here we utilize a non-dimensional angular frequency to substitute for the dimensional frequency.

Unlike the common UAC design strategy, which straightforwardly optimizes the parameters of a structure based on the reflective coefficient, here we propose a reverse design strategy: firstly determine the admittance magnitude and phase to stabilize the first and second modes; then find a feasible UAC structure which meets the required admittance magnitude and phase. In the following, we detail this design strategy based on the current flat-plate boundary layer.

5.2.1 Determination of Admittance

Although the required admittances to stabilize the first and second modes are indeed conflicted with each other, it is compatible to stabilize the first and second modes simultaneously using an identical structure due to the difference in the frequencies of the first and second modes, and that a certain structure has different admittances for different frequencies. From Figure 5.2, we can see the admittance phase should be close to 0.5π and a little larger than π to stabilize the first and second mode, respectively. However, the strick constraints on the admittance phase make the determination of the UAC structure strenuous. Figure 5.2 also reveals the constraint on the admittance phase to stabilize the second mode can be relaxed to $\theta \geq 0.75\pi$. Here we choose $\theta = 0.55\pi$ and $\theta = 0.75\pi$ to damp the first and second mode instabilities, respectively.

Figure 5.3 (a) and (b) depict the maximum growth rate and the corresponding angular frequency of the first mode, respectively, under different admittance magnitudes $|A|$ and $\theta = 0.55\pi$ with the increase of Reynolds number taken into account. Figure 5.3 (a) shows the growth rate of the first mode decrease as the admittance magnitude increases. However, the performance of a UAC with a large admittance magnitude is not prominent. Therefore, the object of UAC to damp the first mode should be degraded to avoid aggravating the first-mode instability. Figure 5.3(b) shows the variation of the non-dimensional angular frequency of the maximum growth rate of the first mode is not manifest when the admittance magnitude increases and the non-dimensional angular frequency is about 0.064 at a relatively large Reynolds number. Therefore, to stabilize the first mode, the frequency $\omega = 0.064$ should be focused on and the admittance phase for this freuqncy should be close to 0.55π.

Concerning the second mode, the maximum growth rates and the corresponding angular frequencies of the second mode are shown in Figure 5.4 (a) and (b), respectively. Apparently, when the admittance magnitude is small, the increase in the admittance magnitude is favorable for the stabilization of the second mode. But when the admittance magnitude is large, a further increase in the admittance magnitude becomes inefficient. Therefore, the criterion for the largest admittance magnitude to stabilize the second mode can be set to 2. From Figure 5.4 (b), we can see the non-dimensional angular frequency of the maximum growth rate is basically in the range of $0.2 \leq \omega < 0.25$ as the admittance magnitude varies from zero to 2.

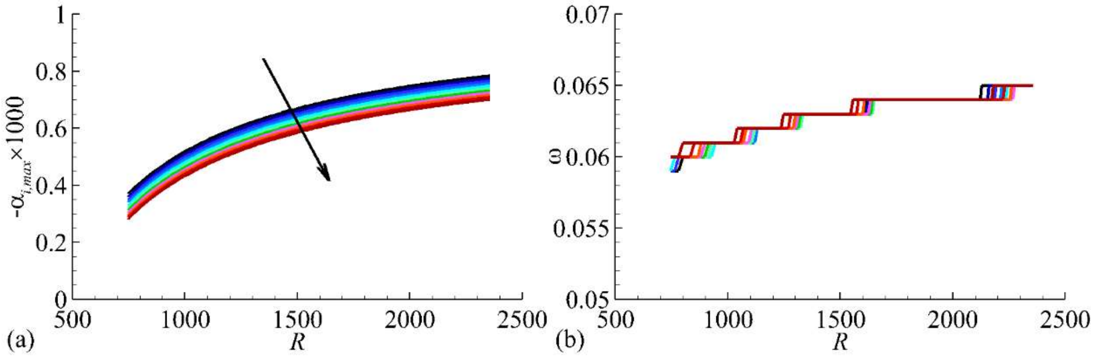

Figure 5.3 (a) maximum growth rate and (b) the corresponding angular frequency for the first mode vs. R under different $|A|$ with $\theta = 0.55\pi$. The arrow denotes the increasing direction of $|A|$ which increases from 0 to 2 with a step of 0.2.

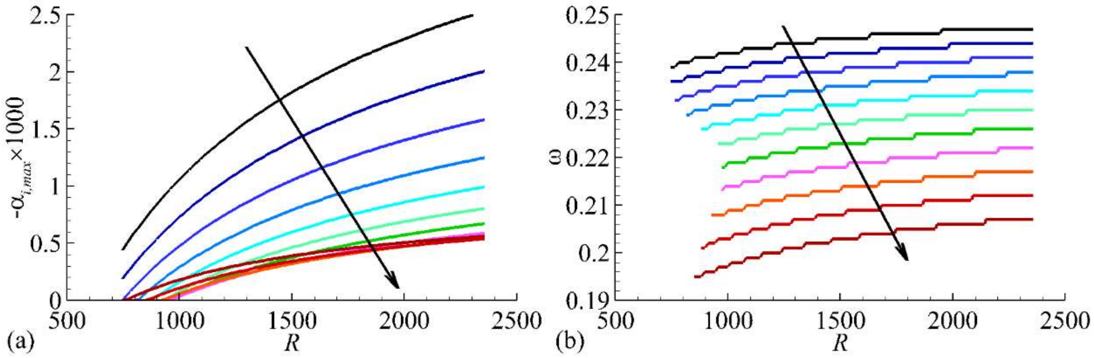

Figure 5.4 (a) maximum growth rate and (b) the corresponding angular frequency for the second mode vs. R under different $|A|$ with $\theta = 0.75\pi$. Arrows denote the increasing direction of $|A|$ which increases from 0 to 2 with a step of 0.2.

In summary, the admittance phase for $\omega = 0.064$ should be close to 0.55π to elude destabilizing the first mode, while to stabilize the second mode instabilities, a UAC should have an admittance phase larger than or equal to 0.75π and admittance magnitude of 2 for the non-dimensional angular frequency in the range of $0.2 \leq \omega < 0.25$.

5.2.2 UAC Design

For the 2D instability problem, we consider a 2D UAC structure consisting of slots with width $2b$, spacing s, and depth H, shown in Figure 5.5, to damp the instability waves. This 2D UAC structure is an equivalent structure of 3D UAC composed of regular microstructures. Its admittance for normal-incident waves is given by [74, 75]

$$\begin{aligned} A = n M_e \sqrt{T_w \left(1 - \frac{\tan(k_v b)}{k_v b}\right)\left(1 + \frac{(\gamma - 1)\tan(k_t b)}{k_t b}\right)} \\ \times \tanh\left(i\omega H M_e \sqrt{\frac{1 + \frac{(\gamma-1)\, tan(k_t b)}{k_t b}}{T_w \left(1 - \frac{tan(k_v b)}{k_v b}\right)}}\right) \end{aligned} \tag{5.1}$$

where n is the porosity of a UAC and $n = \frac{2b}{s}$, the subscript w represents the value at the wall, and k_v and k_t are the viscous wave number and thermal wave number, defined by $k_v = \sqrt{\frac{i\omega R}{T_w \mu_w}}$ and $k_t = \sqrt{Pr} k_v$ [66], respectively. All quantities are non-dimensionalized in the same way with LST calculations, so that the calculated admittance can be applied to the LST calculations straightforwardly.

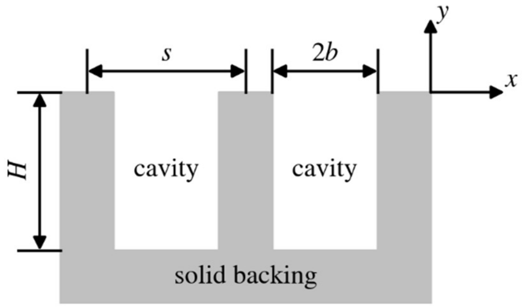

Figure 5.5 Schematic diagram of 2D UAC structure.

Equation (5.1) can also be rewritten as a function of $A = nF(\omega H, \omega b^2 R)$, where F is a function with two variables ωH and $\omega b^2 R$. The contours of the admittance phase and magnitude varied along with ωH and $\omega b^2 R$ are depicted in Figure 5.6 and Figure 5.7, respectively. Notably, the admittance magnitude is proportional to the porosity n, and the porosity $n = 0.1$ is chosen in Figure 5.7. Based on Figure 5.6 and Figure 5.7, the UAC parameters H, b, and s could be found to match the admittance requirements.

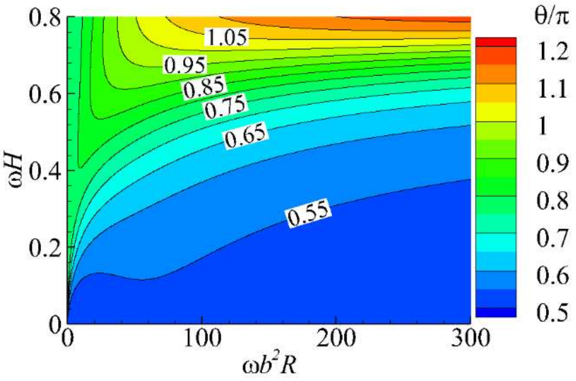

Figure 5.6 Contour of admittance phase θ as a function of ωH and $\omega b^2 R$.

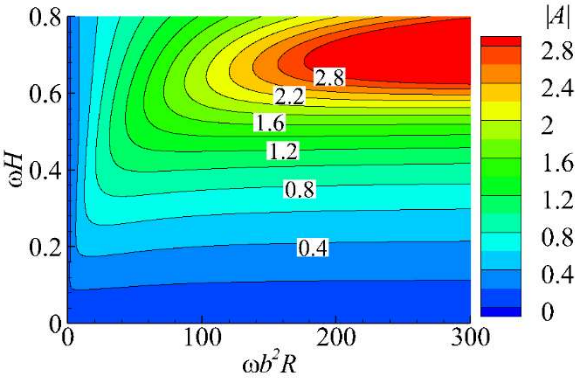

Figure 5.7 Contour of admittance magnitude $|A|$ as a function of ωH and $\omega b^2 R$ with the porosity of $n = 0.1$.

Here we illustrate an example of determining the parameters H, b, and s. For convenience, b^2R is set as a constant. Assuming $b^2R = 400$, the dimensional slot half width $b^* = 20(x^*)^{\frac{1}{4}}(Re_1)^{-\frac{3}{4}}$. At $x^* = 0.1\mathrm{m}$, $b^* = 0.049\mathrm{mm}$, which is on the same order of the hole size of UAC employed in the experiments conducted by Fedorov et al. [31], indicating this size is applicable. For the second mode at $\omega = 0.2$, $\omega b^2R = 80$, it is obtained that ωH should satisfy $\omega H \geq 0.52$ to ensure $\theta \geq 0.75\pi$ according to Figure 5.6. Then we yield $H = \frac{0.52}{0.2} = 2.6$. Moreover, the requirements $\theta \geq 0.75\pi$ is satisfied at $b^2R = 400$ and $H = 2.6$ for the second-mode waves with $0.2 \leq \omega < 0.25$. Pertaining to the first mode of $\omega = 0.064$, $\omega H \approx 0.166$ as $H = 2.6$. From Figure 5.6, we identify $\theta = 0.56\pi$ as $\omega b^2R = 25.6$ and $\omega H = 0.166$. This admittance phase approaches the requirement for the first-mode stabilization. Then the parameter b and H are determined.

With respect to the parameter s, it can be resolved according to the requirement on the admittance magnitude for the second mode. At $\omega b^2R = 80$ and $\omega H = 0.52$, $|A| = 1.5$, therefore, the porosity n should be $n = \frac{2}{1.5} \times 0.1 = 0.133$ to attain $|A| = 2$, which leads to $s = \frac{2b}{n} = 15b$. Thus all the parameters b, H, and s are determined. Furthermore, their dimensional quantities are $b^* = 20(x^*)^{\frac{1}{4}}(Re_1)^{-\frac{3}{4}}$, $H^* = 2.6(x^*)^{\frac{1}{2}}(Re_1)^{-\frac{1}{2}}$ and $s^* = 300(x^*)^{\frac{1}{4}}(Re_1)^{-\frac{3}{4}}$. We exert these dimensions in the region from $x^* = 0.08\mathrm{m}$ to $x^* = 0.4\mathrm{m}$. The slot size distribution of the designed UAC can be seen in Figure 5.8. There are at least three slots in a wavelength of the second mode waves which is about $2\delta^*$.

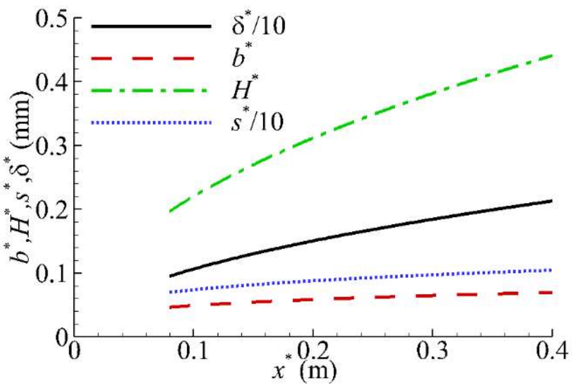

Figure 5.8 Slot size distribution of the designed UAC

Figure 5.9 illustrates the contour of the admittance magnitude and phase of the designed UAC. It can be seen from Figure 5.9 (a) that when the non-dimensional angular frequency is in the range $0.2 \leq \omega < 0.25$, the admittance phase is not less than 0.75π, and pertaining to $\omega = 0.064$, the admittance phase approaches 0.55π. Therefore, the requirements on the admittance phase are satisfied.

In terms of the admittance magnitude, Figure 5.9 (b) shows for the non-dimensional angular frequency in the range $0.2 \leq \omega < 0.25$, the admittance magnitude is equal or larger than 2 depending on ω. When $\omega = 0.2$, $|A| = 2$, and for a larger ω, the admittance magnitude increases. Indeed, the second-mode waves with a large non-dimensional angular frequency are stabilized by a large admittance magnitude according to Figure 5.2. Consequently, the admittance of the UAC matches the requirements on the stabilization of the first and second modes.

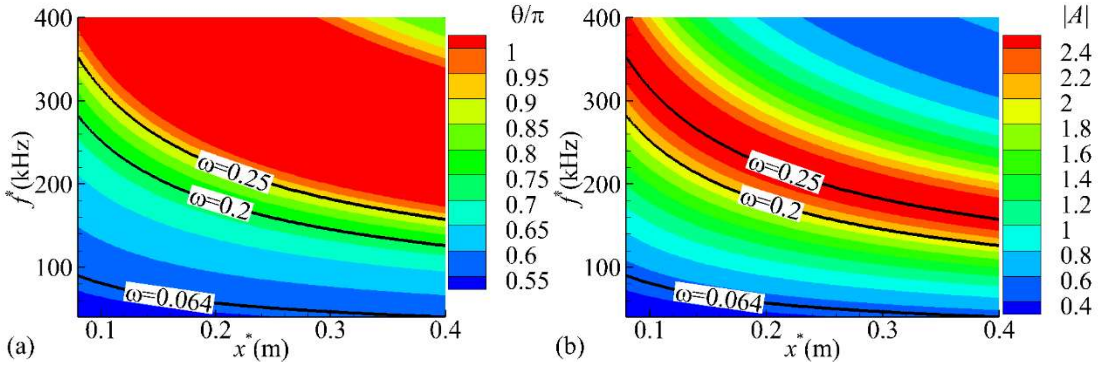

Figure 5.9 Contours of (a) admittance phase and (b) magnitude of the designed UAC for normal incident waves.

5.3 UAC Performance

To validate the performance of this UAC, we utilize LST to examine the growth rate of unstable waves in a wide frequency band with regarding the first and second modes simultaneously, as shown in Figure 5.10. In terms of the first mode, the maximum growth rate of each disturbance frequency is slightly attenuated by the UAC, as depicted in Figure 5.10 (a). Of the stabilization effect of the designed UAC on the second mode, Figure 5.10 (b) demonstrates the maximum growth rate is remarkably damped in a wide frequency band. Therefore, the designed UAC can efficiently stabilize the second mode instabilities and meanwhile do not aggravate the first mode instabilities.

In addition, this UAC structure is resolved based on the current flow conditions, for a different combination of the free-stream Mach number M_∞, wall temperature ratio T_w/T_∞ and Reynolds number R, the non-dimensional angular frequency ω of the first and second modes should be redetermined, as well as the requirements on the admittance.

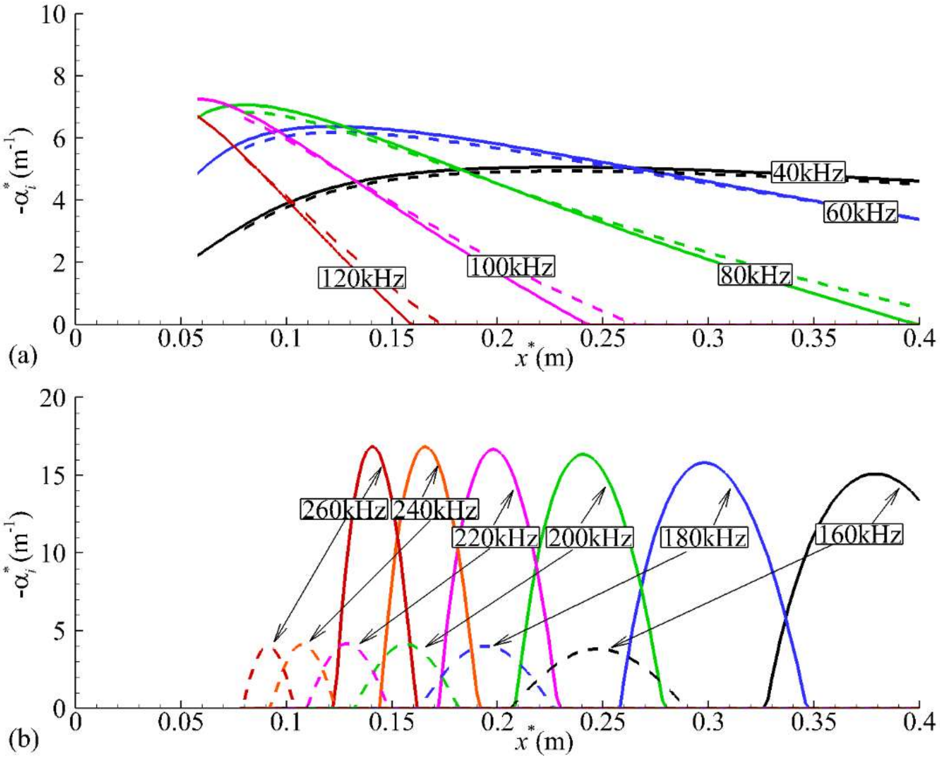

Figure 5.10 Comparison in the growth rate of (a) the first and (b) second modes between the smooth solid wall (solid lines) and the designed UAC (dashed line).

Chapter 6 Conclusions

In the present research, the effects of porous walls on the first and second modes in supersonic/hypersonic boundary layers are investigated using LST or DNS method, and the mechanisms of the first and second mode instabilities in hypersonic boundary layers with and without porous walls are also studied using phase analysis on the simplified disturbance energy equation. Moreover, a design strategy for UAC to stabilize the first and second mode simultaneously is proposed based on a supersonic boundary layer.

For an adiabatic or quasi-adiabatic wall, the regularities of the effects of porous walls on the first and second mode instabilities are identical between the hypersonic and supersonic boundary layers. When the admittance phase is close to π, the second mode is effectively stabilized while the first mode is destabilized. On the contrary, when the admittance phase is close to 0.5π, the second mode is destabilized with a shift to the low-frequency band accompanied, whereas the first mode is comparatively stabilized. If the admittance phase approaches to 1.5π, the frequency of the second mode shifts to a high-frequency band. These effects are facilitated by the increase in the admittance magnitude. Moreover, the regularities of the effects of porous walls on the 2D waves are also applicable to oblique waves.

The phase analyses on the simplified disturbance energy equation show both for the first and second modes, the time rate of change of the fluctuating internal energy is dominated by the mean-flow advection of perturbed thermal energy in the vicinity of the critical layer and by the dilatation fluctuation near the wall. The growth rate of the second mode waves depends on the contribution of the energy transport by the wall-normal velocity fluctuation. When the energy transport by the wall-normal velocity fluctuation is in phase with the total time rate of change of fluctuating internal energy in the vicinity of the critical layer, the contribution of the energy transport by the wall-normal velocity fluctuation is great, which leads to a large growth rate. Pertaining to the amplification of the first mode waves, involving the oblique wave, it is found that the phase overlap between the time rate of change of fluctuating internal energy and the energy change due to dilatation fluctuations below the critical layer is proportional to the growth rate. Particularly, for the oblique first-mode wave, the growth rate is also involved with the contribution of energy transport by the wall-normal velocity fluctuation around the critical layer.

If a porous wall is applied, the amplitude and phase of the wall-normal fluctuating velocity are altered at the wall, which exerts impacts on the near-wall dilatation fluctuation. For the second mode, the phase of the wall-normal fluctuating velocity is delayed when the admittance phase tends to π and advanced when the admittance phase tends to 0, and the intensity change in the near-wall dilatation fluctuation alter the phase of the temperature perturbation at moderate y, then such phase shifts result in the alteration in the critical-layer phase overlap between the energy transport by the wall-normal velocity fluctuation and the total time rate of change of fluctuating internal energy. The frequency shift of the second mode is associated with the augmentation or reduction of the amplitude of the wall-normal fluctuating velocity near the wall. Whereas for the first mode, the stabilization is related to the shrinking in the phase superposition between the time rate of change of fluctuating internal energy and the energy change due to dilatation fluctuations, while the destabilization is due to the diminishing in the critical-layer phase discrepancy of the energy transport by the wall-normal velocity fluctuation and the total time rate of change of fluctuating internal energy.

Appendix A

The explicit form of Equation (2.10) is shown below:

$$
\begin{aligned}
\frac{i}{T}(\alpha U+\beta W-\omega)\,\hat{u}+\frac{1}{T}\frac{dU}{dy}\hat{v} &= -i\alpha\hat{p}\\
&+\frac{\mu}{R}\left[-\frac{4}{3}\alpha^2\hat{u}+\frac{1}{3}\left(i\alpha\frac{d\hat{v}}{dy}-\alpha\beta\hat{w}\right)+\frac{d^2\hat{u}}{dy^2}-\beta^2\hat{u}\right]\\
&+\frac{1}{R}\left[\frac{d\mu}{dy}\left(\frac{d\hat{u}}{dy}+i\alpha\hat{v}\right)+\frac{d\mu}{dT}\left(\frac{d^2U}{dy^2}\hat{T}+\frac{dU}{dy}\frac{d\hat{T}}{dy}\right)\right]\\
&+\frac{1}{R}\frac{d^2\mu}{dT^2}\frac{dT}{dy}\frac{dU}{dy}\hat{T}
\end{aligned}
\tag{A.1}
$$

$$
\begin{aligned}
\frac{i}{T}(\alpha U+\beta W-\omega)\hat{v} &= -\frac{d\hat{p}}{dy}\\
&+\frac{\mu}{R}\left[-\alpha^2\hat{v}+\frac{1}{3}\left(i\alpha\frac{d\hat{u}}{dy}+i\beta\frac{d\hat{w}}{dy}\right)+\frac{4}{3}\frac{d^2v}{dy^2}-\beta^2\hat{v}\right]\\
&+\frac{1}{R}\left[\frac{d\mu}{dT}\left(i\alpha\frac{dU}{dy}+i\beta\frac{dW}{dy}\right)\hat{T}-\frac{2}{3}\frac{d\mu}{dy}\left(i\alpha\hat{u}+i\beta\hat{w}-2\frac{d\hat{v}}{dy}\right)\right]
\end{aligned}
\tag{A.2}
$$

$$
\begin{aligned}
\frac{i}{T}(\alpha U+\beta W-\omega)\hat{w}+\frac{1}{T}\frac{dW}{dy}\hat{v} &= -i\beta\hat{p}\\
&+\frac{\mu}{R}\left[-\alpha^2\hat{w}+\frac{1}{3}\left(-\alpha\beta\hat{u}+i\beta\frac{d\hat{v}}{dy}\right)+\frac{d^2\hat{w}}{dy^2}-\frac{4}{3}\beta^2\hat{w}\right]\\
&+\frac{1}{R}\left[\frac{d\mu}{dy}\left(i\beta\hat{v}+\frac{d\hat{w}}{dy}\right)+\frac{d\mu}{dT}\left(\frac{d^2W}{dy^2}\hat{T}+\frac{dW}{dy}\frac{d\hat{T}}{dy}\right)\right]\\
&+\frac{1}{R}\frac{d^2\mu}{dT^2}\frac{dT}{dy}\frac{dW}{dy}\hat{T}
\end{aligned}
\tag{A.3}
$$

$$
\begin{aligned}
\frac{1}{T}(\alpha U+\beta W-\omega)\hat{T} &= i(\gamma-1)M^2(\alpha U+\beta W-\omega)\hat{p}\\
&+\frac{\mu}{R\sigma}\left[-\alpha^2\hat{T}+\frac{d^2\hat{T}}{dy^2}-\beta^2\hat{T}+\frac{2}{k}\frac{dk}{dT}\frac{dT}{dy}\frac{d\hat{T}}{dy}\right]\\
&+\frac{\mu}{R\sigma k}\left[\frac{dk}{dT}\frac{d^2T}{dy^2}+\frac{d^2k}{dT^2}\left(\frac{dT}{dy}\right)^2\right]\hat{T}\\
&+2(\gamma-1)M^2\frac{\mu}{R}\left[\frac{dU}{dy}\left(\frac{d\hat{u}}{dy}+i\alpha\hat{v}\right)+\frac{dW}{dy}\left(i\beta\hat{v}+\frac{d\hat{w}}{dy}\right)\right]\\
&+(\gamma-1)M^2\frac{1}{R}\frac{d\mu}{dT}\left[\left(\frac{dU}{dy}\right)^2+\left(\frac{dW}{dy}\right)^2\right]\hat{T}
\end{aligned}
\tag{A.4}
$$

$$
\gamma Ma_e^2(i\alpha U-i\omega)\hat{p}-(i\alpha U-i\omega)\frac{\hat{T}}{T}+i\alpha\hat{u}+\frac{\partial\hat{v}}{\partial y}-\frac{dT}{dy}\frac{\hat{v}}{T}+i\beta\hat{w}=0 \tag{A.5}
$$

References

1. Rushton, G.H. and K.F. Stetson, *Shock tunnel investigation of boundary-layer transition at M equals 5.5.* AIAA Journal, 1967. **5**(5): p. 899-906.
2. Reed, H.L., et al., *DRAG PREDICTION AND TRANSITION IN HYPERSONIC FLOW.* AIAA Journal, 1997.
3. Mack, L., *Boundary-Layer Stability Theory," Document 900-277, Rev. A.* Jet Propulsion Lab., Pasadena, CA, 1969.
4. Morkovin, M., E. Reshotko, and T. Herbert, *Transition in open flow systems-a reassessment.* Bull. Am. Phys. Soc, 1994. **39**(9): p. 1882.
5. Reshotko, E., *Transient growth: A factor in bypass transition.* Physics of Fluids, 2001. **13**(5): p. 1067-1075.
6. Fedorov, A. and A. Tumin, *Receptivity of High-Speed Boundary Layers to Kinetic Fluctuations.* AIAA Journal, 2017. **55**(7): p. 2335-2348.
7. Mack, L.M., *Boundary-layer linear stability theory*. 1984, CALIFORNIA INST OF TECH PASADENA JET PROPULSION LAB.
8. Mack, L.M., *Linear stability theory and the problem of supersonic boundary-layer transition.* AIAA Journal, 1975. **13**(3): p. 278-289.
9. Fedorov, A., *Transition and Stability of High-Speed Boundary Layers.* Annual Review of Fluid Mechanics, 2011. **43**(1): p. 79-95.
10. Lysenko, V. and A. Maslov, *The effect of cooling on supersonic boundary-layer stability.* Journal of Fluid Mechanics, 1984. **147**: p. 39-52.
11. Malmuth, N., et al., *Problems in high speed flow prediction relevant to control.*

1998.

12. Morkovin, M.V., *Transition at hypersonic speeds.* NASA CR 178315, 1987.

13. Stetson, K., et al. *Laminar boundary layer stability experiments on a cone at Mach 8. I-Sharp cone*. in *16th Fluid and Plasmadynamics Conference*. 1983.

14. F, S.K. and K.R. L. *On hypersonic boundary-layer stability*. in *30th Aerospace Sciences Meeting and Exhibit*. 1992.

15. F, S.K. and K.R. L, *Example of second-mode instability dominance at a Mach number of 5. 2.* AIAA Journal, 1992. **30**(12): p. 2974-2976.

16. Fedorov, A.V., *Prediction and Control of Laminar-turbulent Transition in High-speed Boundary-Layer Flows.* Procedia IUTAM, 2015. **14**: p. 3-14.

17. Kendall, J.M., *Wind Tunnel Experiments Relating to Supersonic and Hypersonic Boundary-Layer Transition.* AIAA Journal, 1975. **13**(3): p. 290-299.

18. Heitmann, D., R. Radespiel, and H. Knauss, *Experimental Study of Boundary-Layer Response to Laser-Generated Disturbances at Mach 6.* Journal of Spacecraft and Rockets, 2013. **50**(2): p. 294-304.

19. Malik, M., T. Zang, and D. Bushnell. *Boundary layer transition in hypersonic flows*. in *2nd International Aerospace Planes Conference*. 1990.

20. Malik, M.R., *Prediction and control of transition in supersonic and hypersonic boundary layers.* AIAA Journal, 1989. **27**(11): p. 1487-1493.

21. Zhao, R., et al., *Numerical simulation of local wall heating and cooling effect on the stability of a hypersonic boundary layer.* International Journal of Heat

and Mass Transfer, 2018. **121**: p. 986-998.

22. Fedorov, A., et al., *High-Speed Boundary-Layer Stability on a Cone with Localized Wall Heating or Cooling.* AIAA Journal, 2015. **53**(9): p. 2512-2524.

23. Bountin, D., et al., *Stabilization of a Hypersonic Boundary Layer Using a Wavy Surface.* AIAA Journal, 2013. **51**(5): p. 1203-1210.

24. Lysenko, V.I., *Experimental studies of stability and transition in high-speed wakes.* Journal of Fluid Mechanics, 1999. **392**: p. 1-26.

25. Lees, L. and H. Gold. *Stability of laminar boundary layers and wakes at hypersonic speeds. Part I. Stability of laminar wakes*. in *Proc. Int. Symp. on Fundamental Phenomena in Hypersonic Flow (ed. JG Hall)*. 1964.

26. Fedorov, A.V., et al., *Stabilization of Hypersonic Boundary Layers by Porous Coatings.* AIAA Journal, 2001. **39**(4): p. 605-610.

27. Daniels, F.B., *On the Propagation of Sound Waves in a Cylindrical Conduit.* The Journal of the Acoustical Society of America, 1950. **22**(5): p. 563-564.

28. Allard, J.F. and Y. Champoux, *New empirical equations for sound propagation in rigid frame fibrous materials.* The Journal of the Acoustical Society of America, 1992. **91**(6): p. 3346-3353.

29. Stinson, M.R., *The propagation of plane sound waves in narrow and wide circular tubes, and generalization to uniform tubes of arbitrary cross-sectional shape.* The Journal of the Acoustical Society of America, 1991. **89**(2): p. 550-558.

30. Rasheed, A., et al., *Experiments on Passive Hypervelocity Boundary-Layer*

Control Using an Ultrasonically Absorptive Surface. AIAA Journal, 2002. **40**(3): p. 481-489.

31. Fedorov, A.V., et al., *Stability of Hypersonic Boundary Layer on Porous Wall with Regular Microstructure.* AIAA Journal, 2006. **44**(8): p. 1866-1871.

32. Fedorov, A., et al., *Stabilization of a hypersonic boundary layer using an ultrasonically absorptive coating.* Journal of Fluid Mechanics, 2003. **479**: p. 99-124.

33. Wagner, A., et al., *Experiments on passive hypersonic boundary layer control using ultrasonically absorptive carbon-carbon material with random microstructure.* Experiments in Fluids, 2013. **54**(10).

34. Brès, G.A., et al., *Second-mode attenuation and cancellation by porous coatings in a high-speed boundary layer.* Journal of Fluid Mechanics, 2013. **726**: p. 312-337.

35. Sandham, N.D. and H. Lüdeke, *Numerical Study of Mach 6 Boundary-Layer Stabilization by Means of a Porous Surface.* AIAA Journal, 2009. **47**(9): p. 2243-2252.

36. Egorov, I., et al., *Direct Numerical Simulation of Supersonic Boundary-Layer Stabilization by Porous Coatings.* 2007.

37. Bres, G.A., et al., *Alternate Designs of Ultrasonic Absorptive Coatings for Hypersonic Boundary Layer Control.* AIAA Paper, 2009. **4217**: p. 2009.

38. Zhao, R., et al., *Spatial Direct Numerical Simulation of the Hypersonic Boundary-Layer Stabilization Using Porous Coatings.* AIAA Journal, 2019.

57(11): p. 5061-5065.

39. Brès, G.A., T. Colonius, and A.V. Fedorov, *Acoustic Properties of Porous Coatings for Hypersonic Boundary-Layer Control.* AIAA Journal, 2010. **48**(2): p. 267-274.

40. Stephen, S.O. and V. Michael, *Effects of Porous Walls on Hypersonic Boundary Layers over a Sharp Cone.* AIAA Journal, 2013. **51**(5): p. 1234-1244.

41. Lukashevich, S.V., et al., *Stabilization of High-Speed Boundary Layer Using Porous Coatings of Various Thicknesses.* AIAA Journal, 2012. **50**(9): p. 1897-1904.

42. Wang, X. and X. Zhong, *Phase angle of porous coating admittance and its effect on boundary-layer stabilization.* 41st AIAA Fluid Dynamics Conference and Exhibit, 2011.

43. Carpenter, P.W. and L.J. Porter, *Effects of Passive Porous Walls on Boundary-Layer Instability.* AIAA Journal, 2001. **39**(4): p. 597-604.

44. Unnikrishnan, S. and D.V. Gaitonde, *Interactions between vortical, acoustic and thermal components during hypersonic transition.* Journal of Fluid Mechanics, 2019. **868**: p. 611-647.

45. Unnikrishnan, S. and D.V. Gaitonde, *Kovasznay-type analysis of transition modes in a hypersonic boundary layer*, in *2018 AIAA Aerospace Sciences Meeting*. 2018.

46. Malik, M.R., *Numerical Methods for Hypersonic Boundary Layer Stability.*

Journal of computational physics, 1990. **86**: p. 37.

47. El-Hady, N.M., *On the effect of boundary layer growth on the stability of compressible flows.* 1981.

48. El-Hady, N.M., *Nonparallel stability of three-dimensional compressible boundary layers. Part 1: Stability analysis*. Vol. 3245. 1980: National Aeronautics and Space Administration.

49. Malik, M.R., *Boundary-layer transition prediction toolkit*, in *Computational Fluid Dynamics Review 1998: (In 2 Volumes)*. 1998, World Scientific. p. 869-890.

50. Paredes, P., et al., *Transient Growth Analysis of Compressible Boundary Layers with Parabolized Stability Equations.* 2016.

51. Zhang, Y. and C. Su, *Self-consistent parabolized stability equation (PSE) method for compressible boundary layer.* Applied Mathematics and Mechanics, 2015. **36**(7): p. 835-846.

52. Pralits, J.O., et al., *Sensitivity analysis using adjoint parabolized stability equations.* Flow, turbulence and combustion, 2000. **65**: p. 25.

53. Li, F. and M.R. Malik, *On the Nature of PSE Approximation.* Theoretical and Computational Fluid Dynamics, 1996.

54. Chang, C.-L. and M.R. Malik, *Oblique-mode breakdown and secondary instability in supersonic boundary layers.* Journal of Fluid Mechanics, 1994. **273**: p. 37.

55. Chang, C.-L., et al., *Linear and Nonlinear PSE for Compressible Boundary*

Layers. 1993.

56. Chang, C.-L., et al., *Compressible stability of growing boundary layers using parabolized stability equations.* 1991.

57. Bertolotti, F.P. and T. Herbert, *Analysis of the linear stability of compressible boundary layers using the PSE.* Theoretical and Computational Fluid Dynamics, 1991.

58. Tumin, A., *Three-dimensional spatial normal modes in compressible boundary layers.* Journal of Fluid Mechanics, 2007. **586**: p. 295.

59. Tumin, A., *Three-Dimensional Spatial Normal Modes in Compressible Boundary Layers.* 2006.

60. El-Hady, N.M., *Nonparallel instability of supersonic and hypersonic boundary layers.* 1991.

61. El-Hady, N.M., *Spatial three-dimensional secondary instability of compressible boundary-layer flows.* AIAA Journal, 1991. **29**(5): p. 688-696.

62. Cebeci, T., *Analysis of turbulent boundary layers*. 2012: Elsevier.

63. Liang, X., et al., *Effects of wall temperature on boundary layer stability over a blunt cone at Mach 7.99.* Computers & Fluids, 2010. **39**(2): p. 359-371.

64. Zhang, Y., et al., *Receptivity to free-stream disturbance waves for hypersonic flow over a blunt cone.* Science in China Series G: Physics, Mechanics and Astronomy, 2008. **51**(11): p. 1682-1690.

65. Fedorov, A. and A. Tumin, *High-Speed Boundary-Layer Instability: Old Terminology and a New Framework.* AIAA Journal, 2011. **49**(8): p. 1647-1657.

66. Zhao, R., et al., *Theoretical Modeling and Optimization of Porous Coating for Hypersonic Laminar Flow Control.* AIAA Journal, 2018: p. 1-5.

67. Rijke, P.L., *Notice of a new method of causing a vibration of the air contained in a tube open at both ends.* The London, Edinburgh, and Dublin Philosophical Magazine and Journal of Science, 1859. **17**(116): p. 419-422.

68. Strutt, J.W. and B. Rayleigh, *The theory of sound*. Vol. 2. 1945: Dover.

69. Zhu, Y., et al., *Aerodynamic heating in transitional hypersonic boundary layers: Role of second-mode instability.* Physics of Fluids, 2018. **30**(1).

70. Hao, J. and C. Wen, *Stabilization of a Mach 6 Boundary Layer Using a Two-Dimensional Cavity*, in *AIAA Scitech 2019 Forum*. 2019.

71. Laurence, S.J., A. Wagner, and K. Hannemann, *Experimental study of second-mode instability growth and breakdown in a hypersonic boundary layer using high-speed schlieren visualization.* Journal of Fluid Mechanics, 2016. **797**: p. 471-503.

72. Laurence, S.J., A. Wagner, and K. Hannemann, *Schlieren-based techniques for investigating instability development and transition in a hypersonic boundary layer.* Experiments of Fluids, 2014.

73. Laurence, S.J., et al., *Time-Resolved Visualization of Instability Waves in a Hypersonic Boundary Layer.* AIAA Journal, 2012. **50**(1): p. 243-246.

74. Tian, X., et al., *Reverse Design of Ultrasonic Absorptive Coating for the Stabilization of Mack Modes.* AIAA Journal, 2019. **57**(6): p. 2264-2269.

75. Kozlov, V.F., A.V. Fedorov, and N.D. Malmuth, *Acoustic properties of*

rarefied gases inside pores of simple geometries. The Journal of the Acoustical Society of America, 2005. **117**(6): p. 3402-3411.